

ELECTROCHEMICAL SYNTHESIS AND APPLICATIONS OF LAYERED DOUBLE
HYDROXIDES AND DERIVATIVES

Michael S. Kahl, B.S.

Dissertation Prepared for the Degree of
DOCTOR OF PHILOSOPHY

UNIVERSITY OF NORTH TEXAS

August 2015

APPROVED:

Teresa D. Golden, Major Professor
Francis D'Souza, Committee Member
W. Justin Youngblood, Committee Member
Martin Schwartz, Committee Member
Faith Yarberry, External Committee Member
William E. Acree, Chair of the Department of
Chemistry
Costas Tsatsoulis, Interim Dean of Toulouse
Graduate School

Kahl, Michael S. *Electrochemical Synthesis and Applications of Layered Double Hydroxides and Derivatives*. Doctor of Philosophy (Chemistry-Analytical Chemistry), August 2015, 142 pp., 16 tables, 51 illustrations, references, 297 titles .

Layered double hydroxides (LDH) are a class of anionic clay with alternating layers of positive and negative charge. A metal hydroxide layer with divalent and trivalent metals with a positive charge is complemented by an interlayer region containing anions and water with a negative charge. The anions can be exchanged under favorable conditions. Hydrotalcite ($\text{Mg}_6\text{Al}_2(\text{OH})_{16}[\text{CO}_3]\cdot 4\text{H}_2\text{O}$) and other variations are naturally occurring minerals. Synthetic LDH can be prepared as a powder or film by numerous methods. Synthetic LDH is used in electrode materials, adsorbents, nuclear waste treatment, drug delivery systems, water treatment, corrosion protection coatings, and catalysis. In this dissertation Zn-Al- NO_3 derivatives of zaccagnaite ($\text{Zn}_4\text{Al}_2(\text{OH})_{12}[\text{CO}_3]\cdot 3\text{H}_2\text{O}$) are electrochemically synthesized as films and applied to sensing and corrosion resistance applications. First, Zn-Al- NO_3 LDH was potentiostatically electrosynthesized on glassy carbon substrates and applied to the electrochemical detection of gallic acid and caffeic acid in aqueous solutions. The modified electrode was then applied to the detection of gallic acid in green tea samples. The focus of the work shifts to corrosion protection of stainless steel. Modified zaccagnaite films were electrodeposited onto stainless steel in multiples layers to reduce defects caused by drying of the films. The films were deposited using a step potential method. The corrosion resistance of the films in a marine environment was investigated while immersed in 3.5 wt.% NaCl environments. Next modified zaccagnaite films were potentiostatically electrodeposited onto stainless steel followed by a hydrophobization reaction with palmitic acid in order to prepare superhydrophobic ($>150^\circ$

contact angle) surfaces. Each parameter of the film synthesis was optimized to produce a surface with the highest possible contact angle. The fifth chapter examines the corrosion resistance of the optimized superhydrophobic film and a hydrophobic film. The hydrophobic film is prepared using the same procedure as the superhydrophobic film except for a difference in electrodeposition potential. The corrosion resistance of these films is investigated in a simulated marine environment (3.5 wt.% NaCl) for short and extended durations. The last chapter summarizes the previous chapters and suggests future directions for this work.

Copyright 2015

by

Michael S. Kahl

ACKNOWLEDGEMENTS

First I would like to thank my research advisor, Dr. Teresa D. Golden for her continued support, guidance, and encouragement while working on this research project.

I would also like to thank Dr. W. Justin Youngblood, Dr. Francis D'Souza, Dr. Martin Schwartz, and Dr. Faith Yarberry for taking their time to participate as a member of my committee and for the effort and guidance dedicated to my research and dissertation.

I would like to give special thanks to Casey Thurber and Jeerapan Tientong for performing the SEM and EDX experiments.

I would like to thank all of the other group members for their support and advice in completing my research.

Above all I would like to thank my family and friends for their continued encouragement and support.

TABLE OF CONTENTS

ACKNOWLEDGEMENTS.....	iii
LIST OF TABLES.....	viii
LIST OF ILLUSTRATIONS.....	x
CHAPTER 1: INTRODUCTION TO LAYERED DOUBLE HYDROXIDES	1
1.1. Description and Characteristics	1
1.2. Structure and Bonding	2
1.3. Preparation of LDH	4
1.3.1. In Situ Methods	4
1.3.2. Physical Deposition Methods	6
1.4. Post-Synthesis Treatment	8
1.5. LDH Film Applications	9
1.5.1. Anti-Corrosion Coatings	9
1.5.2. Clay-Modified Electrodes (CLMEs) and Other Electrochemical Applications	10
1.5.3. Optical, Electrical, and Magnetic Applications.....	11
1.5.4. Film Catalysis	12
1.5.5. Other Applications	12
1.6. Characterization Techniques	13
1.6.1. Fourier-Transform Infrared Spectroscopy	13

1.6.2. Powder X-Ray Diffraction	16
1.6.3. Scanning Electron Microscopy	19
1.6.4. Elemental Analysis	21
1.6.5. Other Characterization Techniques	22
1.7. Chapter Summaries	22
1.8. References	23
CHAPTER 2: PHENOLIC ACID SENSOR BASED ON LDH MODIFIED GLASSY CARBON	30
2.1. Introduction	30
2.2. Experimental	33
2.2.1. Preparation of Electrolyte Solution and Substrate	33
2.2.2. Electrochemical Techniques.....	33
2.2.2.1. Electrochemical Deposition	33
2.2.2.2. Cyclic Voltammetry	35
2.2.2.3. Differential Pulse Voltammetry	37
2.2.2.4. Electrochemical Impedance Spectroscopy	38
2.2.3. Structural Characterization of Deposited Films	40
2.3. Results and Discussion	41
2.3.1. Structural Characterization	41
2.3.2. Film Morphology	43

2.3.3. Voltammetric Response of LDHf/GCE to GA and CA	44
2.3.4. Effect of Scan Rate	48
2.3.5. Effect of pH	48
2.3.6. Linear Range and Limit of Detection	52
2.3.7. Interference, Stability and Reproducibility	54
2.3.8. Analytical Application	54
2.4. Chapter Conclusions	56
2.5. References	56
CHAPTER 3: CORROSION RESISTANCE OF ELECTROCHEMICALLY SYNTHESIZED MODIFIED	
ZACCAGNAITE FILMS ON STAINLESS STEEL	61
3.1. Introduction	61
3.2. Experimental	64
3.2.1. Film Synthesis	64
3.2.2. Characterization	65
3.2.3. Immersion Tests and Corrosion Measurements	65
3.3. Results and Discussion	69
3.3.1. Structural Characterization	69
3.3.2. Corrosion Resistance	75
3.4. Chapter Conclusions	81

3.5. References	81
CHAPTER 4: INVESTIGATION OF THE OPTIMAL PARAMETERS FOR THE PREPARATION OF	
SUPERHYDROPHOBIC MODIFIED ZACCAGNAITE FILMS ON STAINLESS STEEL	85
4.1. Introduction	85
4.2. Experimental	87
4.2.1. Electrodeposition of Modified Zaccagnaite Film	87
4.2.2. Hydrophobization Reaction	89
4.2.3. Characterization	90
4.2.3.1. Surface Wettability and Contact Angle	90
4.2.3.2. Surface Roughness	94
4.2.3.3. Surface Morphology and Microstructure	95
4.3. Results and Discussion	96
4.3.1. Stainless Steel Substrate	96
4.3.2. Influence of Film Electrodeposition Potential	96
4.3.3. Influence of Film Deposition Time	98
4.3.4. Influence of Palmitic Acid Concentration in Hydrophobization Reaction	100
4.3.5. Influence of Hydrophobization Time	101
4.3.6. Influence of Hydrophobization Temperature	102
4.3.7. Film Structure	104

4.4. Chapter Conclusions	106
4.5. References	107
CHAPTER 5: CORROSION RESISTANCE OF SUPERHYDROPHOBIC AND HYDROPHOBIC MODIFIED ZACCAGNAITE FILMS ON STAINLESS STEEL	
5.1. Introduction	111
5.2. Experimental	114
5.2.1. Substrate Preparation and Film Synthesis	114
5.2.2. Film Hydrophobization	115
5.2.3. Characterization	115
5.2.4. Contact Angle Measurement	115
5.2.5. Immersion Tests and Corrosion Measurements	116
5.3. Results and Discussion	117
5.3.1. Structural Characterization and Morphology	117
5.3.2. Contact Angle	121
5.3.3. Corrosion Resistance	122
5.4. Chapter Conclusions	133
5.5. References	134
CHAPTER 6: CONCLUSIONS AND SUGGESTIONS FOR FUTURE WORK.....	
6.1. Conclusions	138
6.2. Suggestions for Future Work	140

LIST OF TABLES

Table 1.1. Possible cations in LDH [compiled from 1,12,13]	4
Table 1.2. Common FTIR peaks	15
Table 3.1. Elemental composition and thickness of the electrodeposited films (n=3)	72
Table 3.2. Corrosion potentials and corrosion current densities derived from polarization experiments performed in 3.5 wt.% NaCl (n=3)	76
Table 3.3. Corrosion potentials and corrosion current densities derived from immersion of a 5L film in 3.5 wt.% NaCl for various immersion times (n=3)	78
Table 4.1. Properties of hydrophilic and hydrophobic surfaces	90
Table 4.2. Surface roughness parameters and SWCA of SS (n=3)	96
Table 4.3. Film thickness and roughness values (n=3)	98
Table 4.4. Elemental analysis, roughness parameters, and SWCA of 1, 2, and 3 min modified zaccagnaite/palmitate film depositions at -1.3 V (n=3)	98
Table 4.5. SWCA of modified zaccagnaite/palmitate films where the palmitic acid concentration varied while the other parameters are kept static (3 min film electrodeposition time, 7 h hydrophobization reaction time at 70° C) (n=3)	101
Table 4.6. SWCA of modified zaccagnaite/palmitate films where the hydrophobization reaction time varied while the other parameters kept static (3 min film electrodeposition time, 0.1M palmitic acid concentration, hydrophobization reaction performed at 70° C) (n=3)	102
Table 4.7. SWCA of modified zaccagnaite/palmitate films where the hydrophobization reaction temperature varied while the other parameters were kept static (3 min film deposition, 0.1M palmitic acid concentration, 7 h hydrophobization reaction time) (n=3)	102

Table 5.1. FTIR assignments of the palmitic acid, MZ, and MZ/P	119
Table 5.2. SWCA of the -1.0 V MZ/P and -1.3 V MZ/P films	122
Table 5.3. Corrosion potential (E_{corr}) and corrosion current density (i_{corr}) of the samples	124
Table 5.4. Fitting parameters of impedance spectra after 1 h and 192 h immersion in 3.5% NaCl calculated using ZView	131

LIST OF ILLUSTRATIONS

Figure 1.1. Structural schematic of LDH	3
Figure 1.2. Schematic of FTIR	15
Figure 1.3. X-ray diffractometer schematic.....	16
Figure 1.4. Diagram of X-ray beams and diffraction from crystal planes.....	18
Figure 1.5. SEM instrument diagram.....	20
Figure 2.1. Electrochemical cell for LDH deposition.....	34
Figure 2.2. A) Applied waveform for a CV and B) cyclic voltammogram of a classical reversible system	35
Figure 2.3. DPV waveform	37
Figure 2.4. A) Nyquist plot and B) Randles circuit	39
Figure 2.5. A) FT-IR spectrum of Zn-Al-NO ₃ LDHf/GCE and B) XRD pattern of Zn-Al-NO ₃ LDHf/GCE	41
Figure 2.6. Nyquist plots obtained for a) bare GC electrode and b)-e) LDHf/GCEs at deposition times of 30, 60, 90 and 120s, respectively	43
Figure 2.7. SEM image of LDHf/GCE	44
Figure 2.8. Consecutive CV cycles of 0.1 mM (A) GA and (B) CA at a bare GCE.....	45
Figure 2.9. Cyclic voltammograms of 0.1 mM (A) GA and (B) CA at (a) bare GCE and (b) LDHf/GCE.....	46
Figure 2.10. Cyclic voltammograms of 0.1 mM (A) GA and (B) CA in 0.1 M pH 3 PBS at a LDHf/GCE at different scan rates (50, 100, 150, 200, 250, 300, 350, 400) and at 50 mv/s in the absence of analyte	49

Figure 2.11. Log I vs. log v was plotted for the oxidation peaks of (A) GA and (B) CA.....	50
Figure 2.12. CVs of GA and CA at various pHs	51
Figure 2.13. The differential pulse voltammograms of (A) GA at a) 0, b) 4, c) 40, d) 60, e) 80, f) 140, g) 180, h) 400, i) 600 and (B) CA at a) 0, b) 7, c) 20, d) 40, e) 60, f) 80, g) 120, h) 140, i) 160, j) 180. The inset shows the plot of the DPV peak current vs. the concentration. Amplitude: 0.05 V; pulse width: 0.06s; pulse period: 0.2s CA.....	53
Figure 2.14. Calibration curve of the standard addition method for GA determination in green tea by DPV at LDHf/GCE CA	55
Figure 3.1. Diagram of the pitting corrosion of stainless steel in seawater.....	66
Figure 3.2. Example of Tafel plot and extrapolation	68
Figure 3.3. X-ray diffraction pattern of a modified zaccagnaite coating on a stainless steel substrate	69
Figure 3.4. FT-IR spectrum of a modified zaccagnaite film	70
Figure 3.5. SEM images of modified zaccagnaite films for (a) 1L, (b) 2L, (c) 5L and (d) 5L film with a portion of top phase removed	71
Figure 3.6. Film formation process of the mixed hydroxide phase and top aluminum hydroxide layer for the electrodeposited zaccagnaite coating	74
Figure 3.7. Film composition from substrate to outer layer for the electrodeposited zaccagnaite coating.....	74
Figure 3.8. Polarization curves of the substrate and modified zaccagnaite films measured in 3.5 wt.% NaCl solution	75
Figure 3.9. Polarization curves of 5L films immersed in 3.5 wt.% NaCl solution up to 168h.....	78

Figure 3.10. SEM images of 5L film (a) before and (b) after immersion in 3.5 wt. % NaCl solution for 168h as well as (c) an enlarged image of a defect in the immersed film	79
Figure 3.11. Postulated corrosion mechanism for immersed electrodeposited zaccagnaite film	80
Figure 4.1. Illustration of the in situ electrosynthesis of modified zaccagnaite and hydrophobization reaction to produce a superhydrophobic surface	89
Figure 4.2. Contact angle classification	91
Figure 4.3. Representations of a droplet on an ideal surface	92
Figure 4.4. Depiction of the a) Wenzel state and the b) Cassie state	93
Figure 4.5. Digital images of the a) -1 V film and b) -1.3 V film. Low magnification of SEM images of film deposited at c) -1.0 V film and d) -1.3 V film and higher magnification SEM images of e) -1.0 V film and d) -1.3 V film	97
Figure 4.6. Schematic of film composition a) before and b) after hydrophobization reaction .	100
Figure 4.7. SEM of modified zaccagnaite/palmitate film at a) high and b) low magnification..	103
Figure 4.8. Comparison of SWCA on a) SS, b) modified zaccagnaite, and c) optimized zaccagnaite/palmitate film	103
Figure 4.9. XRD patterns of modified zaccagnaite films deposited for 3 min and 15 min.....	105
Figure 4.10. FT-IR spectra of a) palmitic acid, b) modified zaccagnaite film, and c) the modified zaccagnaite/palmitate film	106
Figure 5.1. Illustration of SHP surface water repellency	113
Figure 5.2. XRD patterns of the a) -1.0 V MZ and b) -1.3 V MZ films	118

Figure 5.3. FTIR spectra of the -1.0 V MZ and -1.3 V MZ films before and after the hydrophobization reaction	119
Figure 5.4. SEM images of a,c) -1 V MZ film at different magnifications and b,d) -1.3 V MZ film at different magnifications. SEM images of e) -1 V MZ/P film and f) -1.3 V MZ/P film.....	120
Figure 5.5. Optical images of the SWCA for a) -1.0 V MZ/P and b) -1.3 V MZ/P films	121
Figure 5.6. a) Polarization curves of SS, -1.0 V MZ, -1.0 V MZ/P and -1.3 V MZ measured in 3.5 wt.% NaCl. b) Polarization curve of the -1.3 V MZ/P film in 3.5 wt.% NaCl	122
Figure 5.7. Equivalent circuit model used to fit EIS data of bare SS substrate, MZ films, and MZ/P films.....	125
Figure 5.8. a) Nyquist plot, b) Bode plot of $\log Z $ vs. $\log(\text{frequency})$, and c) Bode plot of phase angle vs. $\log(\text{frequency})$ of samples at 1 h immersion in 3.5% NaCl. The straight lines represent the simulated curves from ZView	126
Figure 5.9. a) Nyquist plot, b) Bode plot of $\log Z $ vs. $\log(\text{frequency})$, and c) Bode plot of phase angle vs. $\log(\text{frequency})$ of samples at 192 h immersion in 3.5% NaCl. The straight lines represent the simulated curves from ZView	129
Figure 5.10. OCP monitoring in 3.5% NaCl	132
Figure 5.11. SEM images of a) -1 V MZ, b) -1.3 V MZ, c) -1 V MZ/P, and d) -1.3 V MZ/P films after 192 h immersion in 3.5% NaCl	133

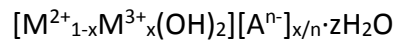
CHAPTER 1

INTRODUCTION TO LAYERED DOUBLE HYDROXIDES

1.1. Description and Characteristics

Layered double hydroxides (LDH) are clay-like materials containing alternating positively charged and negatively charged layers. They are a class of anionic clays containing natural and synthetic variants [1,2]. The positively charged layers are comprised of metal hydroxides and the negative layers contain anions and water. LDH is structurally similar to brucite, $\text{Mg}(\text{OH})_2$, except that the positively charged layer contains both divalent and trivalent cations. The positive charge results from the substitution of divalent ions with trivalent ions in brucite-like metal hydroxide. This positive charge is balanced by interlayer anions which can be exchanged.

The general formula for LDH:



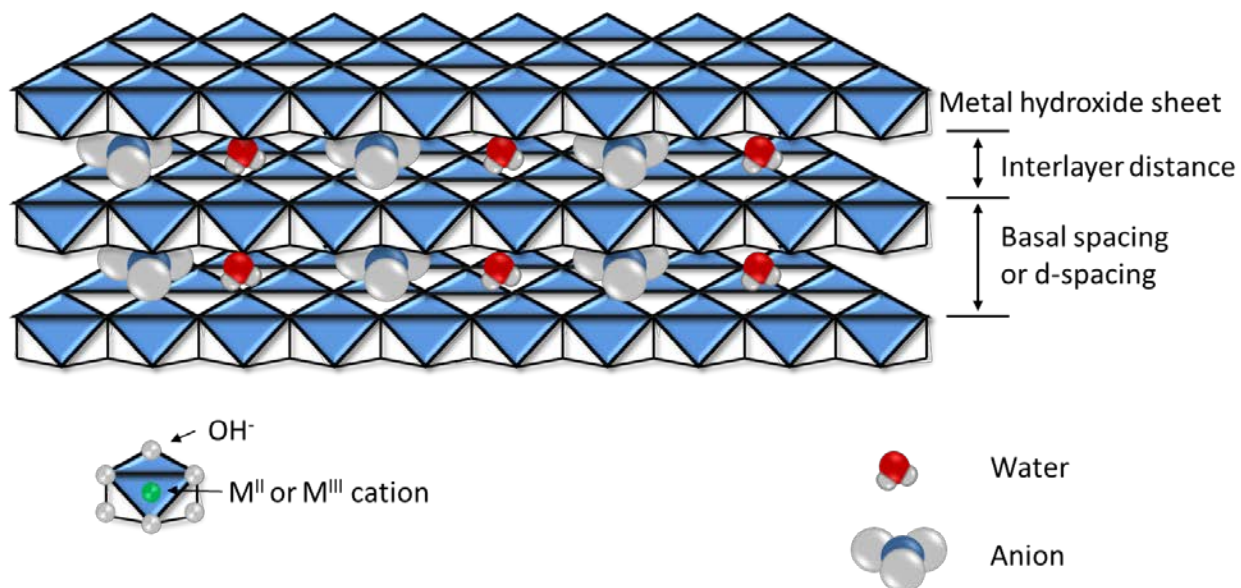
M^{2+} and M^{3+} are divalent and trivalent metal cations, A^{n-} is an anion such as CO_3^{2-} or NO_3^- , x is the $\text{M}^{3+}/(\text{M}^{2+} + \text{M}^{3+})$ mole ratio and z is the number of associated water molecules.

The values of x can vary but the reliable limits are between 0.2 and 0.4 corresponding to $\text{M}^{2+}:\text{M}^{3+}$ ratios of 4:1 and 1.6:1 [1]. Although the x value may be within the reliable limits, it cannot be known for sure that a pure LDH phase has been achieved. There may be secondary phases such as hydroxides or salts of the metal cations. Furthermore, there are exceptions that have x values outside the accepted limits [2-4]. The y value is dependent on the anion and the synthesis conditions. The value of the anion depends on its charge and the amount of trivalent cation in order to achieve charge neutrality.

1.2. Structure and Bonding

LDH is often compared to the brucite because they both exhibit sheet-like morphologies. Both have octahedral symmetry where the metal cations are bonded to six hydroxide groups and each hydroxide group is bonded to three metals. As a result each metal has a coordination number of six and each oxygen has a coordination number of four except for terminal oxygens at the edge of the sheets. LDH differs from brucite because it contains two metals, a divalent and trivalent cation, in the sheets while brucite only has a single divalent cation. Because two metals are used in LDH they have different metal-oxygen bond lengths. The different bond distances result in a grooved or wrinkled sheet [5]. The layers contain divalent and substituted trivalent cations which results in a positive charge. The charge density is proportional to $M^{3+}/(M^{2+} + M^{3+})$. The trivalent cations are not located adjacent to each other to spread the positive charge throughout the layer. These positively charged layers are stacked alternating with negatively charged anions and water molecules to balance the charge as shown in Figure 1.1. The higher the charge density the more anions that can be potentially intercalated. Anions and water are not only intercalated but also adsorbed on the edges and surfaces of the LDH layers. The intercalated anions do not participate in direct electrostatic attraction with the trivalent cations but are hydrogen-bonded to the hydroxide protruding towards the interlayer. Intercalated water is hydrogen bonded to anions and other water molecules [6].

Figure 1.1. Structural schematic of LDH.



The octahedra of the metal ions are flattened in the stacking direction [1]. This results in a change in symmetry from O_h to D_{3d} . The higher the average metal ionic radius, the more compressed the octahedral structure becomes. The increased stacking lowers the thickness of the hydroxide layer and increases the distance between metals.

LDH exhibits two common stacking sequences; a two-layer hexagonal stacking sequence (2H) or a three-layer rhombohedral stacking sequence (3R) [7]. Both sequences can also exist in the same material at differing proportions [5]. Further classification based on the ordering of the sequences is possible and the most common examples are $3R_1$ and $2H_1$ [8,9]. These designations signify that the interlayer sites are prismatic.

There are many divalent and trivalent cations that can be found in LDH. Table 1.1 shows those that can be present in synthetic LDH. Monovalent-trivalent and divalent-tetravalent LDH layers can be synthesized [1,4]. Also, more than two metals can be placed into the lattice [1,10,11]. Many anions can intercalate into the interlayer including: halides, oxo-anions, organic

anions, oxo-metallates, and polyoxo-metallates. Anion intercalation research shows that carbonate is the easiest ion to intercalate and the hardest ion to exchange. Halides and nitrates are equally able to intercalate but are also easily exchanged. LDHs are never intercalated with carbonate if anion exchange reactions will be performed later. The first LDH discovered was the natural occurring mineral hydrotalcite. Its formula is represented by $\text{Mg}_6\text{Al}_2(\text{OH})_{16}\text{CO}_3 \cdot 2\text{H}_2\text{O}$ [2]. In this project a nitrate intercalated synthetic zaccagnaite, $\text{Zn}_4\text{Al}_2(\text{OH})_{12}\text{NO}_3 \cdot 3\text{H}_2\text{O}$, derivative is used.

Table 1.1. Possible cations in LDH [compiled from 1,12,13].

I-III	II-III	II-IV
Li-Al	Mg, Fe, Co, Ni, Cu, Zn, Ca-Al	Zn, Co-Ti
	Co, Ni, Cu, Zn, Ca-Cr	Zn-Sn
	Mg, Fe, Co, Cu, Zn, Ca-Fe	
	Fe, Co, Ni-Co	
	Ni-Ni	
	Mg, Fe, Co, Ni, Cu, Zn, Ca-Ga	
	Ni, Ca-Ln	

1.3. Preparation of LDH

1.3.1. In Situ Methods

There are numerous ways to synthesize LDH films but each technique can be divided into two categories; in situ growth and physical deposition methods. The in situ growth method

has the greatest adhesion due to the presence of chemical bonds between substrate and film. Also, the substrate shape is not limited to simple geometries. One method to prepare LDH films involves the homogenous precipitation of divalent and trivalent metal salts by the slow hydrolysis of urea. Urea is a weak Bronsted base and is highly soluble in water. Controlled urea hydrolysis in aqueous solutions yield ammonium cyanate or NH_4^+ and NCO^- . Sustained urea hydrolysis produces CO_2 (acidic conditions) or CO_3^{2-} (basic conditions). When the reaction is conducted at temperatures greater than 60°C , urea decomposes into ammonium hydroxide which leads to homogenous precipitation of metal hydroxides [14,15]. Urea hydrolysis uses the substrate, usually aluminum, as the trivalent metal source and the divalent metal is dissolved as a salt in solution. Mg-Al LDH can only be synthesized with this technique. The urea hydrolysis method was used in the creation of Mg-Al LDH films on sulfonated polystyrene substrate [16]. Since the substrate contained no metal ions both LDH cations were dissolved in the reaction solution. In order for Zn-Al and Ni-Al LDH films to be fabricated, ammonia must be substituted for urea and the reaction proceeds in the same manner [17,18]. The Ni-Al LDH film synthesized via the ammonia method is oriented with its ab-faces perpendicular to the substrate and has a very rough surface. The microstructure can be adjusted by altering crystallization time and temperature. The Zn-Al LDH film is surprisingly different with a random orientation. Metal substrates have also been used as the source of divalent cations. Zn-Al and Cu-Al LDH films have been synthesized on zinc and copper substrates using the ammonia method [19]. The aluminum source is a dissolved salt. The thickness and lateral size of the crystallites can be controlled.

Electrodeposition of LDH films has been performed on metal substrates. LDHs containing Co^{II} , Ni^{II} or Zn^{II} and Al^{III} have been synthesized by the cathodic reduction of nitrate ions to create a localized pH increase at the electrode [20,21]. Aluminum hydroxide usually forms initially because of its low solubility and lower pH of formation when compared to the other metal hydroxides [22]. Once the pH increases enough both metal hydroxides precipitate simultaneously. LDH films have been electrochemically synthesized on glassy carbon, gold, platinum, FeCrAlloy, stainless steel, and magnesium alloy [4,20-26]. Choosing an optimum deposition potential is important in obtaining a pure LDH phase [21-23]. The electrodeposited films have low crystallinity and crystallites are randomly oriented because of the rapid kinetics of the deposition mechanism.

1.3.2. Physical Deposition Methods

Physical deposition allows for a wider variety of substrates to be coated and greater variety in the composition of LDH. If the LDH can be synthesized as a powder, it can be fabricated into a film using an appropriate technique. Physical deposition is limited by the weaker adhesion between the film and substrate because of the lack of chemical bonds. Also, the substrate geometry must be simple in order to obtain successful deposition.

Layer-by-layer (LBL) assembly has been utilized in the synthesis of LDH films because of its simplicity and low cost. Film deposition is independent of the type of substrate, size, and film morphology. Delamination of LDH can produce positively charged nanosheets which can be used in LBL deposition [27-29]. The positively charged sheets can be alternated with negatively charged polymers or negatively charged nanosheets to produce inorganic-organic composite or

inorganic films [30-32]. Ultrathin multifunctional heterogeneous films containing different LDH layers can also be assembled by LBL electrostatic assembly [33]. Any negatively-charged species can be combined with positively-charged LDH nanosheets.

LDH particles produced by using separate nucleation and aging steps (SNAS) had smaller diameters and higher uniformity in size distribution than particles produced by regular co-precipitation methods [34]. LDH colloids prepared by the SNAS method produced self-supporting films and films that can be peeled from substrates with dimensions up to several centimeters [35]. The film's ab-faces, platelets, were parallel to the substrate. Solvent evaporation can effectively produce LDH films as long as a colloidal suspension can be prepared. The careful selection of solvent and ultrasonication are sometimes required.

Sol-gel methods combined with spin-coating are another technique utilized to fabricate LDH films. The LDH precursor suspension is applied in excess onto the substrate. The substrate is then rotated at very high speeds to spread the solution equally by centrifugal force. The film is then formed by thermal treatment. LDH films with ab-faces parallel to the substrate have been synthesized [36,37]. The sol-gel method is easily scaled up but is wasteful because of the large amounts of nonaqueous solvents used.

LDH can be synthesized by rehydrating mixed oxide phases that were produced through the calcination of LDH. Amorphous $\text{ZnO}/\text{Al}_2\text{O}_3$ films deposited on glass substrates by sol-gel deposition and calcined at 400°C can be converted into an LDH film by rehydration in hot water [38].

1.4. Post-Synthesis Treatment

Post-synthesis treatment is common when the LDH is synthesized as a powder. This treatment usually involves reflux of the LDH in its mother liquor (aged) or simple stirring in mother liquor (fresh or raw). The precipitate from both methods is centrifuged and washed repeatedly with high purity water. Aging results in more crystalline material and sharper more intense diffraction peaks [1]. Anion exchange is possible on LDH powders because of its alternating layered structure. Nitrate- and chloride-LDH are the best precursors for anion exchange reactions because of their low selectivity [39]. The procedure for anion exchange involves an aqueous suspension of the precursor stirred in the presence of a large excess (10-20 times) of the desired anion. The pH of the reaction is important because the hydroxide layer and the desired anion must both be stable. Delamination is another common post-synthesis treatment for LDH powders. Delamination can be carried out with a variety of techniques. The delamination of LDH powders can produce thin positively charged platelets which can be utilized in composites with polymer, metal or organic materials [40]. The composites have a wide array of applications.

LDH films typically do not undergo post-treatment except for rinsing with high purity water and drying in air or under a stream of nitrogen. Sometimes the films are heated up to 100°C in order to remove surface waters. LDH films can undergo various post-synthesis modifications. One such modification is calcination which is performed on the powder as well as the films [41,42]. Temperatures of various decomposition processes vary depending on the intercalated anion. Calcination involves heating the LDH up to temperatures of 1000°C in order to produce a mixed oxide phase. As the film is heated to 250°C the film becomes dehydrated

because the surface and interlayer waters have been driven off. The removal of water forces the interlayers to collapse. At 300-500°C dehydroxylation of the metal hydroxide layers occurs to form mixed oxides and the decomposition of the anion occurs. The decomposition of LDH eventually leads to the formation of a spinel product.

Surface modifications can be performed on synthesized LDH films. Surface anion exchange reactions are performed by immersing the film in a solution containing the dissolved modifier. These reactions usually impart some properties on the film such as hydrophobicity or corrosion resistance [10,17,43].

1.5. LDH Film Applications

1.5.1. Anti-Corrosion Coatings

The estimated cost of metal corrosion amounts to just over \$276 billion which is more than 3% of the US GDP in 2002 [44]. Due to inflation and the aging infrastructure the current cost is much higher. There are many ways to reduce corrosion but the most effective method is to utilize protective coatings [45,46]. There have been several studies that have observed the corrosion resistance of LDH films on various metal substrates. These films were synthesized by a variety of methods [10,25,36]. In situ prepared films provided the best protection and adhesion; however, most coatings deteriorated during prolonged immersion in corrosive solution. Intercalation of corrosion inhibitors into the LDH films has been investigated [47].

Recent research has focused on the surface chemistry of anti-corrosion films. Specifically, superhydrophobic films with high water contact angles (CA) of >150 and very small CA hysteresis have been investigated [48,49]. Superhydrophobic films can be constructed from

the combination of appropriate hierarchical micro/nanoscale surface structure (surface roughness) and low surface energy materials. Most LDH films are hydrophilic although there are a few exceptions with a hydrophobic CA [4,50]. Most of the hydrophobic and superhydrophobic films are prepared on top of a porous aluminum substrate or another metal which has been acid etched [10,17]. The films are usually prepared by an in situ hydrothermal method and result in vertically aligned nanosheets with high surface roughness. The LDH films are then immersed in an aqueous solution at an elevated temperature containing the low surface energy modifier which is usually sodium laurate. The barrier properties of the LDH film combine with the hydrophobic properties of the laurate modified surface to enhance corrosion protection.

1.5.2. Clay-modified Electrodes (CLMEs) and Other Electrochemical Applications

Electron transfer at clay-modified electrodes (CLMEs) has been thoroughly researched. LDH is a nonconducting material which results in poor charge transport. This means that only a small amount of adsorbed anions are electroactive [51]. Although LDHs are nonconducting, they have a high surface area, and adsorptive properties because of their permanent positive charge. CLMEs are attractive electrode materials because of their ability to concentrate the analyte in a small area near the electrode surface during the preconcentration step allowing for the detection of very dilute concentrations [52].

CLMEs have electrocatalytic properties and the ability to immobilize electrocatalytic reagents that increase sensitivity and selectivity. Electrocatalysis is the mediation of an electron transfer between the analyte and electrode surface by an immobilized catalyst or the film itself. A reduction in overpotential and an increase in peak current usually results [53]. CLMEs may

also be applied to the development of biosensors because of the adsorption of proteins on clay surfaces. LDH films have been synthesized with immobilized redox mediators [54].

Charge transport in CLMEs can be improved by using redox active sites in the LDH film such as Ni^{2+} , Co^{2+} or Mn^{2+} [56]. CLMEs with improved charge transport have been as ion-selective electrodes, oxidation of primary alcohols and sugars, and utilized in amperometric sensing [56-58]. Ni based LDHs have also been investigated as cathodes for nickel batteries and biosensors with immobilized proteins [59,60]. Co-based LDH films been synthesized for use as capacitors [61].

1.5.3. Optical, Electrical and Magnetic Applications

LDH films have been used as precursors for $\text{M}^{\text{II}}\text{M}^{\text{III}}_2\text{O}_4$ spinel films. Superparamagnetic MgFe_2O_4 films were obtained by calcining $\text{MgFe}^{\text{II}}\text{Fe}^{\text{III}}$ LDH films [62]. A porous $\text{ZnO}/\text{Zn}/\text{Al}_2\text{O}_3$ nanosheet was prepared from Zn-Al LDH film on a Zn-covered stainless steel substrate. When used as an anode for Li-ion batteries, the material exhibited better properties than pure ZnO because the inactive ZnAl_2O_4 relieved stress due to volume change during charge-discharge cycling [19].

LDH films used in optical or electrical devices are intercalated with an organic anion. Co-Al LDH nanosheets and poly(sodium styrene 4-sulfonate) composite films behaved as ferromagnetic layers at room temperature [63]. Multilayer assemblies had a significant magneto-optical response in the UV-Vis region. Anionic sulfonated poly(p-phenylene) derivative/LDH ultrathin films showed blue luminescence and LDH monolayers with tris(1,10-phenanthroline-4,7-diphenylsulfonate)ruthenium(II) anions showed red luminescence [64,65].

Optically transparent films with reversible thermochromic behavior between 35-65°C were synthesized by intercalating Zn-Al LDH films with different molar ratios of 4-(4-anilinophenylazo)benzenesulfonate and sodium dodecylbenzene sulfonate [66]. A LDH monolayer grafted with poly(methylmethacrylate) on quartz exhibited excellent UV blocking capabilities [67].

1.5.4. Film Catalysis

Calcined LDHs and activated rehydrated LDHs which contain intercalated hydroxide ions have excellent base catalytic properties. They have been studied as catalysts for aldol condensation, Michael addition, Claisen-Schmidt, Knoevenagel condensation, Wittig, and Henry reactions [68-73]. Fabrication of LDH films as catalysts allows for easy removal when the reaction has completed. Films with ab-faces perpendicular to the substrate can potentially have greater catalytic efficiency due to the high availability of active sites at the edges of the crystallites.

1.5.5. Other Applications

Intercalated LDH immobilized into a specific orientation on a substrate have intercalated molecules that also show a preferred orientation. A Zn-Al LDH film with ab-faces parallel to the substrate was synthesized with intercalated α -naphthalene acetate and β -naphthalene acetate [74]. Both intercalated molecules exhibited tilt angles of 60° (α) and 65° (β). An organic chromophore film located in an inorganic matrix has many potential applications.

Hydroxide sheets of an LDH film can be used to immobilize functional molecules such as monolayers of zeolites, polymer nanobeads, and caged proteins [75]. The electrostatic attraction between the highly order LDH monolayer and the negatively charged particles allows for an ordered structure. LDH monolayers can be used as assembly templates for different kinds of composites. LDH can also be used to synthesize inorganic particles in the interlayer regions. Cadmium sulfate nanoparticles with controllable sizes have been synthesized from LDH-Cd(EDTA) films [76]. ZnS and CdS 3D structured films were made using the LDH films as the precursor and the template [77].

LDH films have been used in selectively permeable gas membranes. Silicone modified Mg-Al LDH films on macroporous alumina disks formed by solvent evaporation have exhibited a CO₂/N₂ separation factor of 34 [78]. LDH films prepared by electrophoretic deposition on macroporous alumina have exhibited permselectivity for CO₂ [79].

1.6. Characterization Techniques

1.6.1. Fourier-Transform Infrared Spectroscopy

Fourier-transform infrared spectroscopy (FTIR) is a vibrational spectroscopy technique that measures the infrared (IR) energy absorption of a gas, liquid or solid sample. The complex vibrations of molecules can be divided into separate vibrational modes. The vibrational modes of chemical bonds have measurable and characteristic frequencies in the IR region. These absorption bands can be used to identify functional groups and provide information pertaining to the chemical bonds in the sample. The IR region is subdivided into three regions; far (400-10 cm⁻¹), mid (4000-400 cm⁻¹) and near (14,000-4,000 cm⁻¹).

The main components of a FTIR include a radiation source, Michelson interferometer, sample compartment, and detector. A schematic of an instrument is shown in Figure 1.2. The source generates radiation containing multiple frequencies which heads to the Michelson interferometer. The interferometer contains two mirrors (one stationary and one moveable) and a beam splitter. The interferometer splits the beam from the source into two so that the paths of the beams are different. The two beams are recombined and directed to the detector where the difference in intensities is measured as a function of the difference in the split radiation paths. The signal is amplified and converted to a digital signal. The digital signal then reaches the computer where the Fourier transform is performed and the spectrum is generated. The spectrum can be viewed as percent transmittance or absorption vs. wavenumber. The equations for transmittance and absorbance are

$$\%T = I/I_0 \quad \text{(Equation 1. 1)}$$

$$A = -\log_{10}(T) \quad \text{(Equation 1.2)}$$

where %T is percent transmittance, I is the transmitted light intensity, I_0 is the incident light intensity, and A is absorbance [80].

FTIR is a very important technique for LDH characterization. The mid-IR region (4000-400 cm^{-1}) is the main focus when characterizing LDH. The presence of metal hydroxide, water (intercalated and surface) and anions can be determined. Table 1.2 shows the major LDH FTIR peaks. Breaking down the mid-IR region further hydroxide stretching is observed at 3700-3000 cm^{-1} . The hydroxide stretching modes are a result of the metal-hydroxide bonds and from water. In the 3000-1000 cm^{-1} region water bending and anion stretching modes are observed. Below 1000 cm^{-1} anion vibrational modes can be seen. LDH intercalated with halides do not

have internal vibrational modes since they do not have an oscillating dipole. In the same region metal hydroxide stretching and bending occurs. The metal hydroxide vibrations are dependent on the cation content of the LDH.

Figure 1.2. Schematic of FTIR.

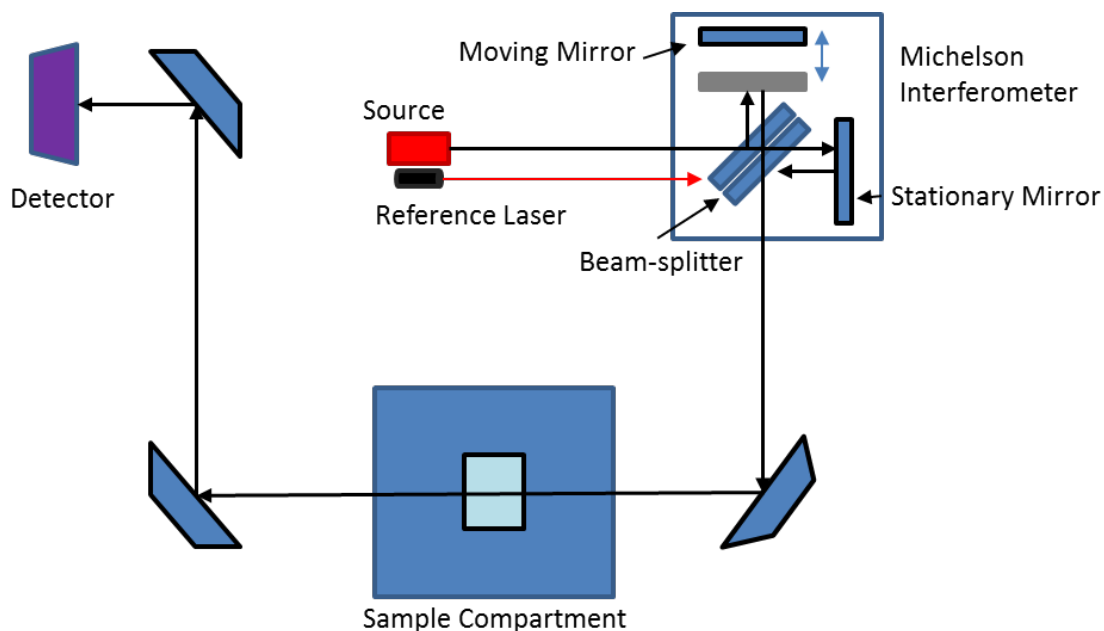


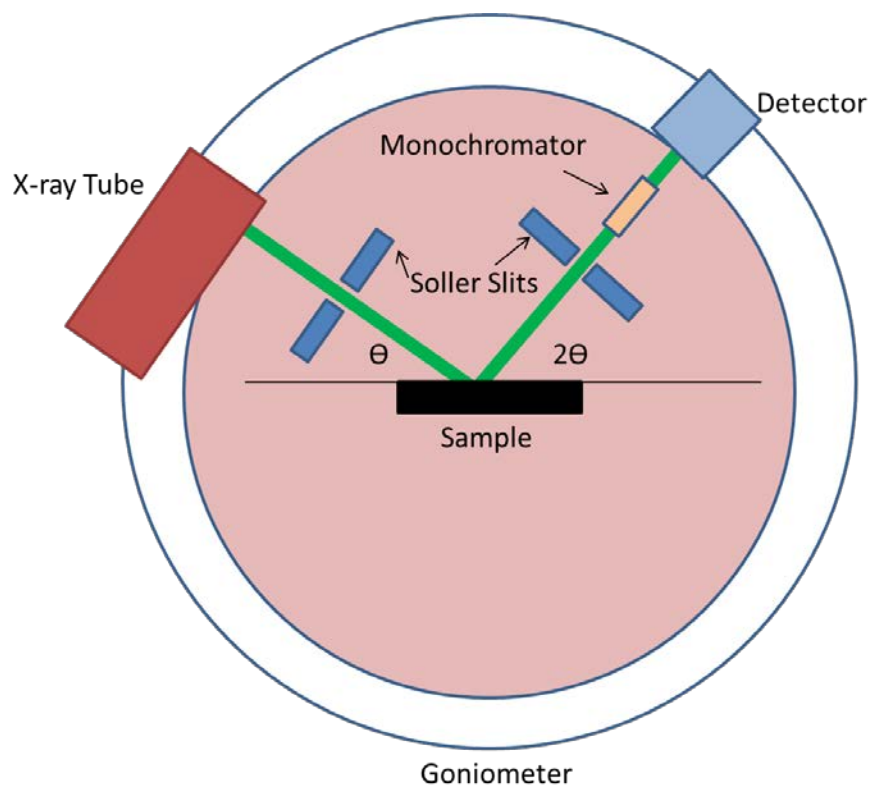
Table 1.2. Common FTIR peaks.

IR Assignment	Associated Wavenumber Range (cm ⁻¹)
M-OH translation	400-800
Doublet M-OH deformation	940-1000
Asymmetric anion stretch (NO ₃ ⁻ or CO ₃ ²⁻)	1340-1400
H ₂ O bending	1600-1660
OH stretching	3000-3700

1.6.2. Powder X-Ray Diffraction

Powder X-ray diffraction (XRD) is a very important structural characterization technique. It is used mostly for the identification of unknown crystalline material. The analysis of unknown solids is important in the fields of engineering, environmental science, geology, materials science, and biology. Crystalline material can be examined in order to determine phase composition, unit cell dimensions, and sample purity. The main components of an X-ray diffractometer shown in Figure 1.3 are a source, monochromator/filters, goniometer, sample holder, and detector.

Figure 1.3. X-ray diffractometer schematic.

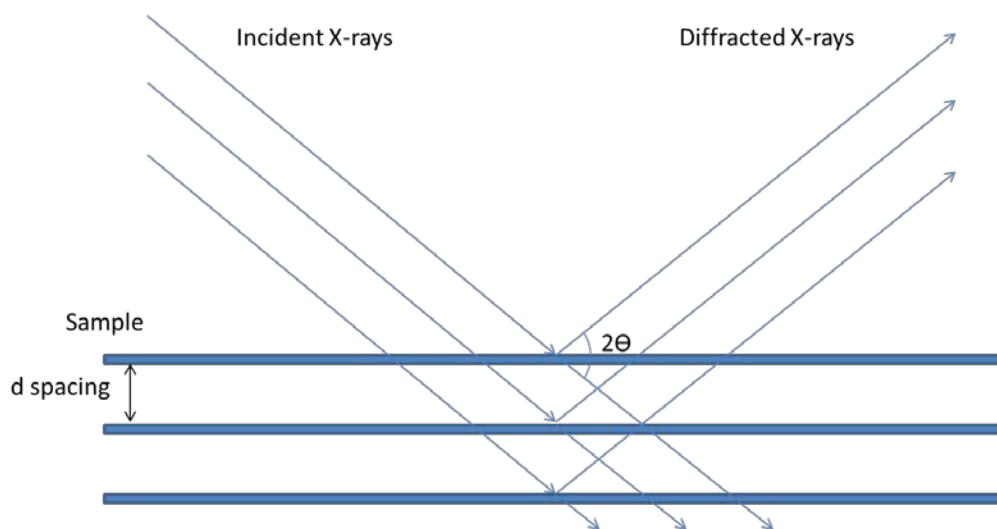


X-ray generation occurs when a cathode ray tube heats a filament through the application of high voltage. As the filament heats up electrons are produced and accelerated towards a metal anode. Electrons that have enough energy to displace inner shell electrons of the anode result in the emission of X-rays. The resulting X-ray spectra contains several components which include K_α and K_β . K_α is comprised of $K_{\alpha 1}$ and $K_{\alpha 2}$, which has a longer wavelength and half the intensity of $K_{\alpha 1}$. The actual wavelengths depend on the metal comprising the anode. Copper is the most common anode used in X-ray diffraction and the K_α wavelengths are close enough to each other that a weighted average ($\text{Cu}K_\alpha = 0.15418 \text{ \AA}$) is used in calculations. Soller slits are used to collimate the X-ray beam. The X-rays are focused and directed to the sample located in the middle of the goniometer. The goniometer ensures that the sample and detector are rotated such that the focused X-ray beam strikes the sample at an angle θ while the detector collects X-rays at an angle of 2θ . A monochromator is used to select the wavelength of interest diffracted from the sample. The detector records the intensity of the reflected X-rays and converts the collected X-rays into a counts value which is output to the computer. A peak is observed when the geometry of the incident X-rays follows Bragg's Law, constructive interference occurs and a peak is visible in the resulting XRD pattern which is observed as intensity (usually counts per second) vs. degrees (2θ). A diagram of X-ray diffraction is shown in Figure 1.4. Bragg's Law relates the wavelength (λ) of the X-ray radiation to the diffraction angle (θ) and lattice spacing (d).

$$n\lambda = 2d\sin(\theta) \qquad \text{(Equation 1.3)}$$

The variable n represents the order of diffraction and is usually represented by a positive integer. Usually only the first order is examined. Typical scans are run from 5° to 70° although some may start at 2° and end at a higher 2θ .

Figure 1.4. Diagram of X-ray beams and diffraction from crystal planes.



XRD can be used to determine interlayer distance, crystallinity, particle size, repeat layer distances and distances between adjacent cations in powder LDH. Powder LDH commonly displays reflections with Miller indices of 003, 006, 009, 012, 015, and 018 from 2° to 60° based on the interlayer spacings. Two other peaks, reflections 110 and 113, depend on the actual LDH lattice sheets and are commonly observed in powder LDH. In electrochemically synthesized LDH the material is less crystalline because of the fast deposition time and all of the LDH peaks may not be visible [23]. Although electrochemically synthesized material provides less XRD information, we can still calculate the basal spacing and identify some impurity phases. The 003 and 006 reflections will be seen even if the LDH is poorly crystalline. The 003 reflection is the

peak with the smallest angle. The exact diffraction angle will depend on the size of the anion. The larger the anion the smaller the 003 peak angle and vice versa. The interlayer or d-spacing can be calculated from the 003 reflection using Bragg's Law. The interlayer spacing is the distance from one LDH sheet to the next and is affected by the size of the anion in the interlayer. The interlayer spacing is a certain range for the anion that is intercalated into the LDH. Nitrate LDHs can have two different interlayer distances depending on the metal hydroxide layer charge. A higher layer charge results in the ions intercalating with an orientation parallel to the stacking direction (8.8 Å) and a lower layer charge results in an orientation perpendicular to the stacking direction (8.0 Å) [81,82]. Nitrate LDH are poorly ordered and their structure has not been thoroughly investigated [83]. Impurity phases such as metal or metal oxides can be observed from 30°-50° [23].

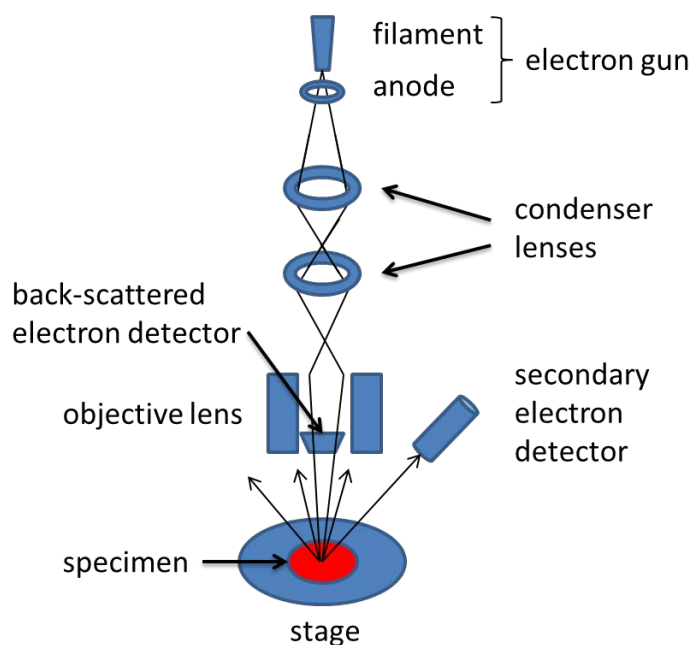
The d_{110} and d_{113} reflections are observed in more crystalline LDH samples and can give information about the LDH sheets. The two peaks are usually located after 60° and sometimes overlap. The d_{110} reflection can provide the distance between two adjacent hydroxide groups or the average distance between two metal ions. This distance is calculated by multiplying the d-spacing of the (110) reflection by 2.

1.6.3. Scanning Electron Microscopy

Scanning electron microscopy (SEM) is a technique used to examine the morphology of a conducting sample whether it is a powder or film. High energy electrons are focused into a beam to probe the surface of the sample. The magnification ranges from 10-500,000 and results in images have a resolution of nanometers to micrometers. The electron beam has an

energy range of 0.5 to 50 keV and can be focused into a spot size ranging from 0.4 to 5 nm. A SEM schematic is shown in Figure 1.5.

Figure 1.5. SEM instrument diagram.



The electron beam produces several signals but the most important include secondary electrons and back-scattered electrons. Back-scattered electrons are the result of elastic scattering and provide a visualization of the composition. They can also provide information about the distribution of elements in the sample. Secondary electrons can show surface topography. Usually the surface of the sample must be conducting and grounded. Nonconducting surfaces cause scanning faults and image artifacts. Nonconducting surfaces can be coated with a thin layer of electrically conducting material such as gold. Nonconducting samples can be examined using environmental SEM (ESEM). ESEM instruments have relatively high pressure chambers, short working distances, and low vacuum at the electron gun. The high

pressure around the sample neutralizes charge and amplifies the second electron signals. In this project films were examined by ESEM to observe morphology and homogeneity.

1.6.4. Elemental Analysis

There are several techniques that can provide elemental composition of layered double hydroxides. Atomic absorption spectroscopy (AAS) and inductively couple plasma mass spectrometry (ICP-MS) are often used for powders. When the elemental composition of a thin film is required, energy dispersive X-ray spectroscopy (EDS) is usually performed. AAS and ICP-MS require greater samples masses for analysis while EDS only requires a 2 nm thick film. EDS also requires very little sample preparation and is a nondestructive technique.

EDS is often combined with SEM so an electron beam is used to probe the sample. The electrons excite electrons in the inner shells which results in their ejections from the shell and the creation of an electron hole. An electron from the outer shell fills the hole resulting in the emission of an X-ray containing the energy difference between the shells. The energy of the X-ray is characteristic of whichever atom it came from and a detector can measure the energy and the number of X-rays emitted. The most common detector is a Si(Li) detector which is a PIN diode with a lithium center. Electron-hole pairs form and a voltage pulse occurs when an X-ray passes through the detector. Low conductivity and high resolution must be achieved through liquid-nitrogen cooling.

1.6.5. Other Characterization Techniques

Some notable techniques used in previous research but not conducted in this project include Raman spectroscopy, X-ray photoelectron spectroscopy (XPS), and thermogravimetric analysis (TGA). Raman spectroscopy is vibrational spectroscopy similar to infrared spectroscopy that is based on the inelastic scattering of a monochromatic source. Raman provides complimentary bonding information to infrared spectroscopy. XPS is a surface technique in which a sample is irradiated with a beam of X-rays and the kinetic energy and number of escaping electrons is measured. It can provide information concerning the elemental composition of the surface, elemental contamination, electronic state of each element, and depth profiling with ion etching. TGA is a technique that monitors the weight of a sample as it is subjected to a programmed temperature ramp. It can provide information about the chemical formula and decomposition products.

1.7. Chapter Summaries

Chapter 2 covers in-situ electrochemical synthesis of Zn-Al-NO₃ LDH or zaccagnaite films on glassy carbon electrodes. These films were characterized structurally via XRD and FTIR. The electrochemical behavior of the clay modified electrodes was studied when they were used to detect two phenolic acids, caffeic acid and gallic acid, by differential pulse voltammetry. Then the clay modified electrodes were used as sensors to detect gallic acid in green tea samples.

Chapter 3 investigates the multilayer electrochemical deposition of modified zaccagnaite films onto stainless steel substrates. The elemental content and structure of the film were investigated. The films were tested for their corrosion protection in simulated sea

water (3.5% NaCl). The coatings showed greater protection than the bare stainless steel substrate. The films were immersed in 3.5% NaCl for 1 week and maintained their corrosion protection.

Chapter 4 involves the hydrophobization of electrodeposited modified zaccagnaite films on stainless steel. The surface hydroxide groups reacted with palmitic acid to produce a surface with low wettability and a high contact angle. The surface exchange reaction was optimized according to the parameters of electrodeposition time, palmitic acid concentration, reaction time, and reaction temperature. Contact angle was measured to evaluate each parameter. The films were characterized by FTIR, XRD, SEM/EDS and profilometer.

Chapter 5 examines the corrosion protection of optimized superhydrophobic film synthesized in Chapter 4 and another similar hydrophobic film. The films were tested for their corrosion protection in simulated sea water (3.5% NaCl) with potentiodynamic polarization and electrochemical impedance spectroscopy. Both the hydrophobic and superhydrophobic films exhibited greater corrosion protection than the bare stainless steel substrate with the superhydrophobic film providing the greatest protection.

Chapter 6 summarizes the previous chapters and proposes further experiments to expand upon this work.

1.8. References

[1] A. de Roy, C. Forano, J.P. Besse, Layered double hydroxides: synthesis and post-synthesis modification, in: V. Rives (Ed.), *Layered Double Hydroxides: Present and Future*, Nova Science Publishers, Inc., New York, 2001, 1-39.

- [2] S. J. Mills, A. G. Christy, J. -M. R. Génin, T. Kameda, F. Colombo, *Mineralogical Mag.*, 76, 2012, 1289-1336.
- [3] A. N. Salak, A. D. Lisenkov, M. L. Zheludkevich, and M. G. S. Ferreira, *ECS Electrochemistry Lett.*, 2014, 3, C9-C11.
- [4] J. Syu, J. Uan, M. Lin, Z. Lin, *Corros. Sci.*, 2013, 68, 238–248.
- [5] M. Bellotto, B. Rebours, O. Clause, J. Lynch, D. Bazin, E. Elkaïem, *J Phys. Chem.*, 1996, 100, 8527-8534.
- [6] T.E. Johnson, W. Martens, R.L. Frost, Z. Ding, J.T. Klopogge, *J. Raman. Spectrosc.*, 2002, 33, 604-609.
- [7] A. S. Bookin, V. I. Cherkashin, V. A. Drits, *Clays Clay Miner.*, 1993, 41 , 558-564.
- [8] G. S. Thomas, M. Rajamathi, P. V. Kamath, *Clays Clay Miner.*, 2004, 52 , 693
- [9] A. V. Radha, C. Shivakumara, P. V. Kamath, *Clays Clay Miner.*, 2005, 53 , 520-527.
- [10] X. Lei, L. Wang , X. Zhao , Z. Chang , M. Jiang, D. Yan, X. Sun, *Industrial & Engineering Chemistry Research*, 2013, 52, 17934–17940.
- [11] J. T. Klopogge, R. L. Frost, L. Hickey, *J. Raman. Spectrosc.*, 2004, 35, 967–974.
- [12] O. Saber, H. Tagaya, *J. Incl. Phenom. Macrocycl. Chem.*, 2003, 45, 107-115.
- [13] O. Saber, H. Tagaya, *J. Porous Mater.*, 2003, 10, 83-91.
- [14] U. Costantino, F. Marmottini, M. Nocchetti, and R. Vivani, *Eur. J. Inorg. Chem.*, 1998, 10, 1439-1446.
- [15] M. Adachi-Pagano, C. Forano, J. P. Besse, *J. Mater. Chem.*, 2003, 13, 1988-1993.
- [16] X. Lei, L. Yang, F. Zhang, D. G. Evans, X. Duan, *Chem. Lett.*, 2005, 34, 1610-1611.

- [17] F. Z. Zhang, L. L. Zhao, H. Y. Chen, S. L. Xu, D. G. Evans and X. Duan, *Angew. Chem. Int. Ed.*, 2008, 47, 2466-2469.
- [18] H. Y. Chen, F. Z. Zhang, S. S. Fu and X. Duan, *Adv. Mater.*, 2006, 18, 3089-3093.
- [19] J. P. Liu, Y. Y. Li, X. T. Huang, G. Y. Li and Z. K. Li, *Adv. Funct. Mater.*, 2008, 18, 1448-1458.
- [20] G. H. A. Therese, P. V. Kamath, *Chem. Mater.*, 2000, 12, 1195-1204.
- [21] I. Gualandi, M. Monti, E. Scavetta, D. Tonelli, V. Prevot, C. Mousty, *Electrochim. Acta*, 2015, 152, 75-83.
- [22] M. Montia, P. Benitoa, F. Basilea, G. Fornasaria, M. Gazzanob, E. Scavettaa, D. Tonellia, A. Vaccaria, *Electrochim. Acta*, 2013, 108, 596-604.
- [23] M.S. Yarger, E.M.P. Steinmiller, K.S. Choi, *Inorg. Chem.*, 2008, 47, 5859–5865.
- [24] M. Kahl, T.D. Golden, *Electroanalysis*, 2014, 26, 1664-1670.
- [25] F. Wu, J. Liang, Z. Peng, B. Liu, *Appl. Surf. Sci.*, 2014, 313, 834–840.
- [26] V. Gupta, S. Gupta, N. Miura, *J. Power Sources*, 2008, 175, 680-685.
- [27] M. A. Pagano, C. Forano, J. P. Besse, *Chem. Commun.*, 2000, 1, 91-92.
- [28] S. O’Leary, D. O’Hare, G. Seeley, *Chem. Commun.*, 2002, 14, 1506-1507.
- [29] T. Hibino and M. Kobayashi, *J. Mater. Chem.*, 2005, 15, 653-656.
- [30] J. Gong, X. Han, X. Zhu, , Z. Guan, *Biosens. Bioelectron.*, 2014, 61, 379–385.
- [31] Z. Zhao, Y. Qi, M. Wei, F. Zhang, S. Xu, *Mater. Lett.*, 2012, 78, 62–65.
- [32] L. Li, R. Ma, Y. Ebina, K. Fukuda, K. Takada, T. Sasaki, *J. Am. Chem. Soc.*, 2007, 129, 8000-8007.
- [33] J. B. Han, J. Lu, M. Wei, Z. L. Wang, X. Duan, *Chem. Commun.*, 2008, 41, 5188-5190.
- [34] Y. Zhao, F. Li, R. Zhang, D. G. Evans, X. Duan, *Chem. Mater.*, 2002, 14, 4286-4291.

- [35] L. Y. Wang, C. Li, M. Liu, D. G. Evans, X. Duan, *Chem. Commun.*, 2007, 2, 123.
- [36] F. Z. Zhang, M. Sun, S. L. Xu, L. L. Zhao, B. W. Zhang, *Chem. Eng. J.*, 2008, 141, 362-367.
- [37] M. Taibi, S. Ammar, F. Schoenstein, N. Jouini, F. Fievet, T. Chauveau, J. M. Greneche, *J. Phys. Chem. Solids*, 2008, 69, 1052-1055.
- [38] N. Yamaguchi, T. Nakamura, K. Tadanaga, A. Matsuda, T. Minami, M. Tatsmisago, *Cryst. Growth Des.*, 2006, 6, 1726-1729.
- [39] S. Miyata, *Clays Clay Miner.*, 1983, 31, 305-311.
- [40] Q. Wang, D. O'Hare, *Chem. Rev.*, 2012, 112, 4124-4155.
- [41] N. Uekawa, T. Saito, T. Kojima, K. Kakegawa, *Mater. Lett.*, 2012, 86, 125–128.
- [42] A. A. A. Ahmed, Z. A. Talib, M. Z. bin Hussein, A. Zakaria, *J. Alloys Compd.*, 2012, 539, 154–160.
- [43] J. Chen, Y. Song, D. Shan, E. Han, *Corros. Sci.*, 2013, 74, 130–138.
- [44] Corrosion Cost and Preventive Strategies In the United States. McLean, Va. (6300 Georgetown Pike, McLean 22101-2296): U.S. Dept. of Transportation, Federal Highway Administration, Research Development and Technology, Turner-Fairbank Highway Research Center, 2002.
- [45] Y. Wang, X. Shua, S. Weia, C. Liu, W. Gao, R. A. Shakoob, R. Kahraman, *J. Alloys Compd.*, 2015, 630, 189–194.
- [46] L. F. Dumée, L. He, Z. Wang, P. Sheath, J. Xiong, C. Feng, M. Y. Tan, F. She, M. Duke, S. Gray, A. Pacheco, P. Hodgson, M. Majumder, L. Kong, *Carbon*, 2015, 87, 395–408.
- [47] M.L. Zheludkevich, S.K. Poznyak, L.M. Rodrigues, D. Raps, T. Hack, L.F. Dick, T. Nunes, M.G.S. Ferreira, *Corros. Sci.*, 2010, 52, 602–611.

- [48] Y. Li, S. Li, Y. Zhang, M. Yu, J. Liu, *Mater. Lett.*, 2015, 142, 137–140.
- [49] X. Wen, C. Ye, Z. Cai, S. Xu, P. Pi, J. Cheng, L. Zhang, Y. Qian, *Appl. Surf. Sci.*, 2015, 339, 109-115.
- [50] F. Yang, B. Y. Xie, J. Z. Sun, J. K. Jin, M. Wang, *Mater. Lett.*, 2008, 62, 1302–1304.
- [51] G. Villemure, A. J. Bard. *J. Electroanal. Chem.*, 1990, 282, 107-121.
- [52] Ni F, Wang Y, Zhang D, Gao F, Li M, *Electroanalysis*, 2010, 22, 1130–1135.
- [53] H. S. Yin, L. Cui, S. Y. Ai, H. Fan, L. S. Zhu, *Electrochim. Acta*, 2010, 55, 603-610.
- [54] M. G. Li, S. H. Chen, F. Ni, Y. L. Wang and L. Wang, *Electrochim. Acta*, 2008, 53, 7255-7260.
- [55] R. Roto, G. Villemure, *J. Electroanal. Chem.*, 2002, 527, 123-130.
- [56] E. Scavetta, M. Berrettoni, M. Giorgetti, D. Tonelli, *Electrochim. Acta*, 2002, 47, 2451-2461.
- [57] B. Ballarin, M. Morigi, E. Scavetta, R. Seeber, D. Tonelli, *J. Electroanal. Chem.*, 2000, 492, 7-14.
- [58] E. Scavetta, M. Berrettoni, R. Seeber, D. Tonelli, *Electrochim. Acta*, 2001, 46, 2681-2692.
- [59] W. Hu, D. Noreus, *Chem. Mater.*, 2003, 15, 974-978.
- [60] X. Chen, C. L. Fu, Y. Wang, W. S. Yang, D. G. Evans, *Biosens. Bioelectron.*, 2008, 24, 356-361.
- [61] Y. Wang, W. S. Yang, C. Chen, D. G. Evans, *J. Power Sources*, 2008, 184, 682-690.
- [62] L. Yang, L. Yin, Y. Zhang, Y. Lu, F. Li, *Chem. Lett.*, 2007, 36, 1462-1463.
- [63] Z. P. Liu, R. Z. Ma, M. Osada, N. Iyi, Y. Ebina, K. Takada, T. Sasaki, *J. Am. Chem. Soc.*, 2006, 128, 4872-4880.
- [64] D. P. Yan, J. Lu, M. Wei, J. B. Han, J. Ma, F. Li, D. G. Evans, X. Duan, *Angew. Chem. Int. Ed.*, 2009, 48, 3073-3076.

- [65] D. P. Yan, J. Lu, M. Wei, J. Ma, D. G. Evans, X. Duan, *Chem. Commun.*, 2009, 42, 6358-6360.
- [66] X. R. Wang, J. Lu, W. Y. Shi, F. Li, M. Wei, D. G. Evans, X. Duan, *Langmuir*, 2010, 26, 1247-1253.
- [67] J. H. Lee, S. W. Rhee, H. J. Nam, D. Y. Jung, *Adv. Mater.*, 2009, 21, 546-549.
- [68] M. J. Climent, A. Corma, S. Iborra, A. Velty, *J. Catal.*, 2004, 221, 474-482.
- [69] M. L. Kantam, B. M. Choudary, C. V. Reddy, K. K. Rao, F. Figueras, *Chem. Commun.*, 1998, 9, 1033-1034.
- [70] M. Sychev, R. Prihod'ko, K. Erdmann, A. Mangel, R. A. V. Santen, *Appl. Clay Sci.*, 2001, 18, 103-110.
- [71] B. M. Choudary, M. L. Kantam, C. V. Reddy, K. K. Rao, F. Figueras, *Green Chem.*, 1999, 1, 187-189.
- [72] K. Ebitani, K. Motokura, K. Mori, T. Mizugaki, K. Kaneda, *J. Org. Chem.*, 2006, 71, 5440-5447.
- [73] F. Winter, A. J. Van Dillen, K. P. De Jong, *Chem. Commun.*, 2005, 31, 3977-3979.
- [74] W. Y. Shi, M. Wei, J. Lu, F. Li, J. He, D. G. Evans, X. Duan, *J. Phys. Chem. C*, 2008, 112, 19886-19895.
- [75] J. H. Lee, H. J. Nam, S. W. Rhee and D. Y. Jung, *Eur. J. Inorg. Chem.*, 2008, 36, 5573-5578.
- [76] X. Xu, F. Z. Zhang, S. L. Xu, J. He, L. Y. Wang, D. G. Evans, X. Duan, *Chem. Commun.*, 2009, 48, 7533-7535.
- [77] B. Schwenzer, L. Z. Pop, J. R. Neilson, T. B. Sbardellati, D. E. Morse, *Inorg. Chem.*, 2009, 48, 1542-1550.
- [78] T. W. Kim, M. Sahimi, T. T. Tsotsis, *Ind. Eng. Chem. Res.*, 2009, 48, 5794-5801.

- [79] T. W. Kim, M. Sahimi, T. T. Tsotsis, *Ind. Eng. Chem. Res.*, 2008, 47, 9127-9132.
- [80] D.A. Skoog, F.J. Holler, S.R. Crouch, *Principles of Instrumental Analysis*, 6th ed., Thomson Brooks, 2007.
- [81] S. V. Prasanna, P. V. Kamath, *Solid State Sci.*, 2008, 10, 260-266.
- [82] S. L. Wang, P. C. Wang, *Coll. Surf. A*, 2007, 292, 131-138.
- [83] S. Radha, P. V. Kamath,, *Z. anorg. allg. Chem.*, 2012, 638, 2317–2323.

CHAPTER 2

PHENOLIC ACID SENSOR BASED ON LDH MODIFIED GLASSY CARBON*

2.1. Introduction

Polyphenols are found in plants and plant products such as wine, tea, and coffee. They are also known to behave as strong antioxidants [1]. Phenolic acids are classified as either benzoic acid or cinnamic acid derivatives. Gallic acid (GA) is a naturally occurring benzoic acid derivative with several health benefits and is found in significant concentrations in teas, berries, hot cocoa, and walnuts [2-5]. GA is a strong antioxidant that possesses anti-inflammatory [6], antimicrobial [7], antimutagenic [8] and anticarcinogenic activities [9]. GA also assists in the regulation of cellular communication [10]. In the pharmaceutical industry, it is used in the determination of phenol content by the Folin-Ciocalteu assay.

Caffeic acid (CA) is a cinnamic acid derivative which is found in wine, coffee, tea, olive oil, fruits, and vegetables [11]. CA is an integral part of a plant's defense against infection [12, 13] and also enhances immunity in humans [14]. The CA content of wines affects many properties such as color, bitterness and oxidation level. CA is also a strong antioxidant with antimutagenic and anticarcinogenic properties [15]. Caffeic acid derivatives show promise in exhibiting anti-HIV activity in cell cultures [16], and have been shown to control the levels of triglycerides and cholesterol in humans [14].

There are several published methods on GA determination which include spectrometric, chromatographic and electrochemical methods [2, 17-20]. Electrochemical sensing allows for

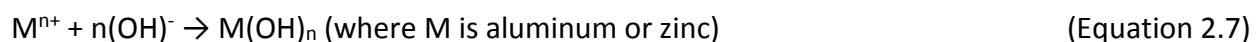
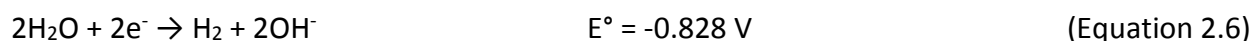
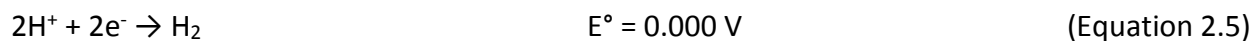
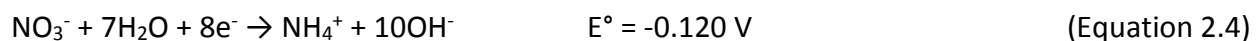
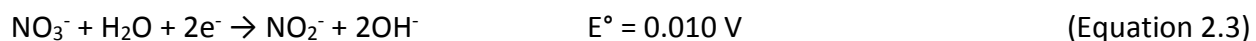
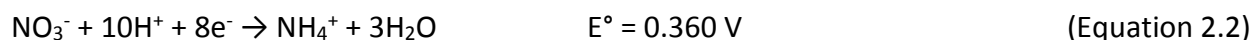
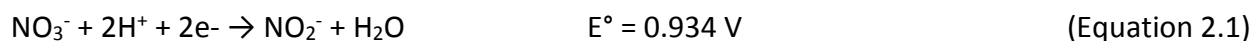
* Parts of this chapter have been previously published, either in part or in full, from M. Kahl, T. D. Golden, *Electroanalysis*, 2014, 26, 8. Reproduced with permission from John Wiley & Sons, Inc.

inexpensive, sensitive and reproducible determination. The oxidation of GA at the glassy carbon electrode (GCE) has been the subject of a previous study [21]. Electrode modifying materials include carbon nanotubes, polyethyleneimine-functionalized graphene and polyepinephrine [18, 22, 23]. These studies achieved great limits of detection but narrow linear ranges. There are also several methods for CA determination that incorporate chromatographic [14, 24-28] and electrochemical methods [29-32]. Oxidation of CA on glassy carbon has been studied as well [13, 33]. CA has been determined by lead film, electrochemically reduced graphene oxide–Nafion composite film, and molecularly imprinted siloxanes [30,34,35]. The detection limits were great but the linear ranges were narrow and some films require extensive preparation.

Since GA and CA are phenolic acids, they are prone to form polymeric products on the surface of electrodes during the oxidation process. These polymeric products can foul the surface of the electrode and distort electrochemical responses. Modified electrodes can protect against surface fouling and possibly catalyze the oxidation reaction. Wang et al. fabricated carbon nanotube modified electrodes to enhance the stability and sensitivity for measuring various phenolic compounds [36].

Layered double hydroxides (LDH) are attractive materials because of their biocompatibility, catalytic activity, great adsorbability, low cost, chemical stability, high ion exchange capacity, and intercalation properties [37, 38]. These properties make them suitable for electrochemical sensor applications. Yarger et al. demonstrated that LDH modified electrodes can be easily synthesized [39]. The electrochemical synthesis of hydroxides occurs by electrogeneration of base via nitrate reduction at the electrode (Eqs. 1-4) [40]. KNO_3 is used as

the supporting electrolyte and source of nitrates. The pH at the electrode increases because of the generation of OH⁻ and the consumption of H⁺ (Eqs. 5 and 6). The higher the applied cathodic potential, the higher and quicker the pH increases, because the nitrate reduction reactions proceed at a faster rate. Precipitation of metal hydroxides at the electrode consumes OH⁻ and lowers the pH (Eq. 7) [41]. The proposed electrode reactions are:



Electrochemical synthesis of LDH films is cheap, simple and allows for greater control during deposition. Previous studies have used glassy carbon modified with a LDH film (LDHf/GCE) to determine bisphenol A, simultaneously determine hydroquinone and catechol, as well as uric acid and epinephrine [42-44].

In this study, an LDHf/GCE electrode was fabricated to electrochemically determine GA and CA content in phosphate buffer solution. Also, the oxidation of GA and CA was studied for both the GCE and the LDHf/GCE electrochemical sensors. The electrodeposition procedure to produce the LDHf/GCE sensor was a facile one step synthesis. The electrochemical determination method was applied to the determination of GA in commercial green tea samples.

2.2. Experimental

2.2.1. Preparation of Electrolyte Solution and Substrate

Gallic acid monohydrate and caffeic acid were purchased from Fischer Scientific Inc. Phosphate buffer solution (PBS) was prepared by mixing stock solution of 0.2 M NaH_2PO_4 and 0.2M Na_2HPO_4 . Aluminum nitrate nonahydrate ($\text{Al}(\text{NO}_3)_3 \cdot 9\text{H}_2\text{O}$, Alfa Aesar), zinc nitrate hexahydrate ($\text{Zn}(\text{NO}_3)_2 \cdot 6\text{H}_2\text{O}$, Alfa Aesar), and potassium nitrate (KNO_3 , Fisher Scientific) were used as received for the synthesis of Zn/Al LDH. All the solutions were prepared with Millipore water.

The bare GCE was polished with 1 μm diamond and then with 0.3 and 0.05 μm alumina slurry on micro-cloth pads. The electrode was rinsed with ethanol after the diamond polish step and with distilled water after each alumina polish. The electrolytic solution was prepared by dissolving a 2:1 molar ratio of Zn^{2+} to Al^{3+} ions, with NO_3^- as the interlayer anion, in Millipore water. Potassium nitrate at a concentration of 0.1 M was added as an electrolyte to help facilitate the formation of the Zn-Al- NO_3 LDH film at the electrode surface.

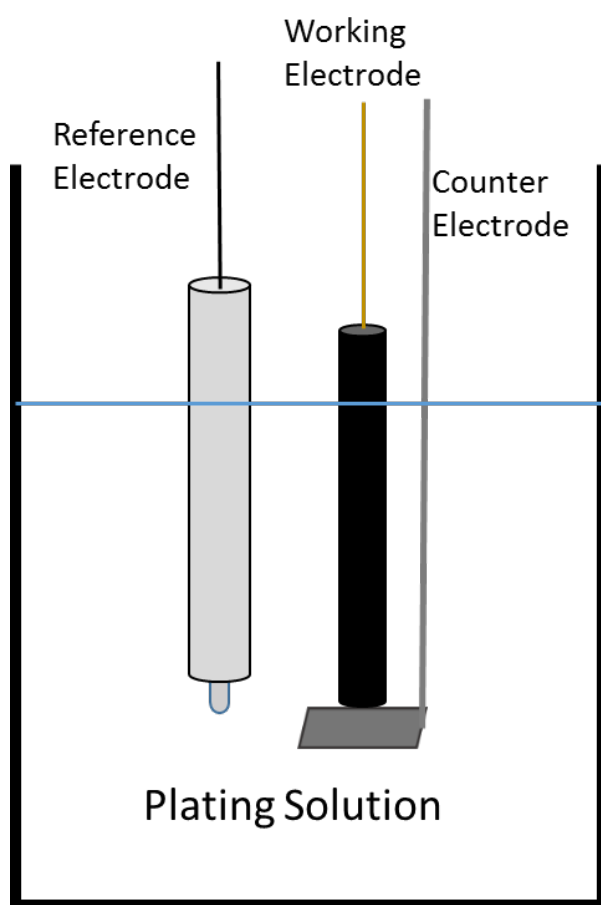
2.2.2. Electrochemical Techniques

2.2.2.1. Electrochemical Deposition

Electrochemical deposition of LDH films were performed by cathodic potentiostatic deposition using a Princeton Applied Research (PAR) 273A potentiostat/galvanostat. The working electrode (WE) was a bare GCE (CH Instruments, Inc., diameter = 3 mm), a saturated calomel electrode (SCE) was used as the reference electrode (RE), and a platinum mesh was the counter electrode (CE). The electrochemical cell configuration is depicted in Figure 2.1. A

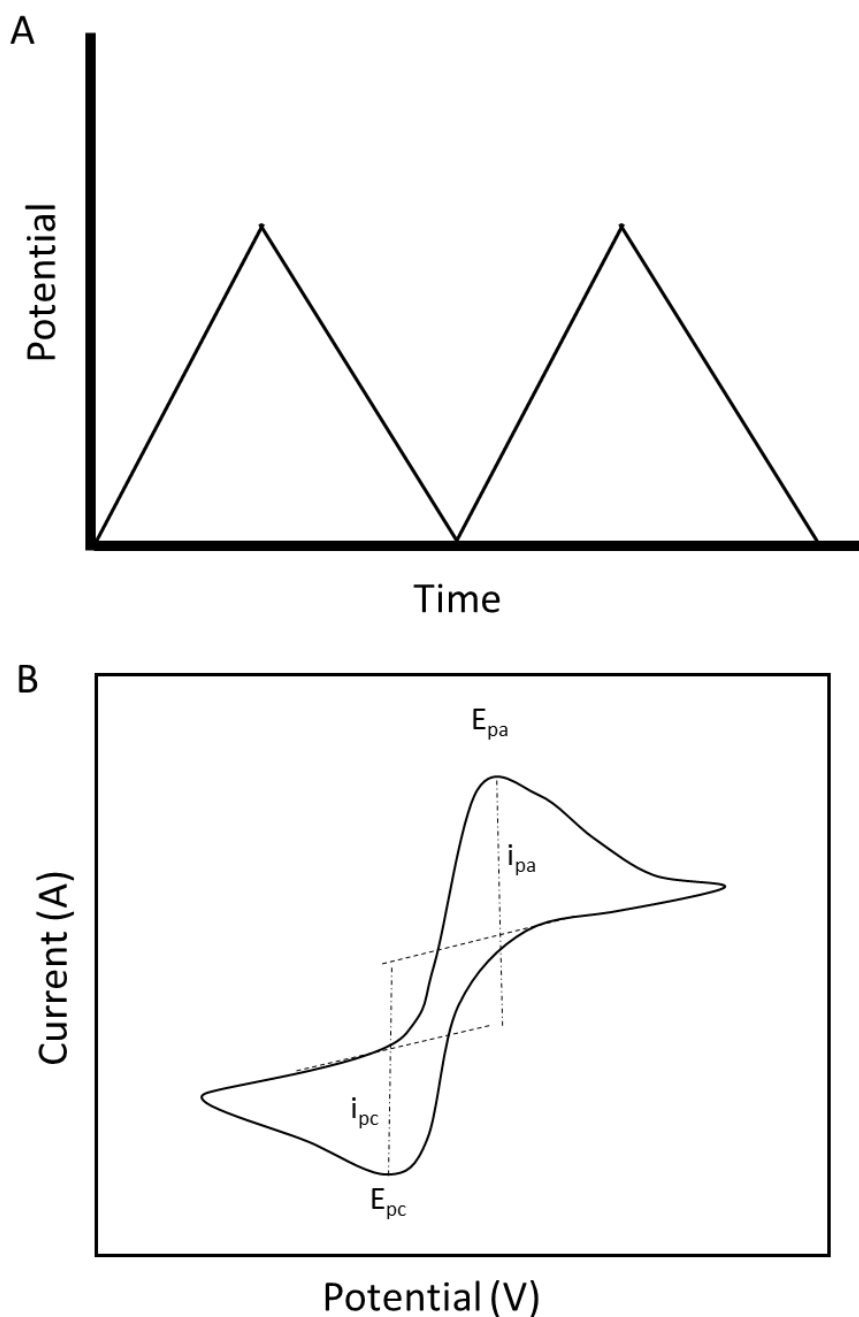
voltage of -0.9 V was applied at the GCE for 60s to deposit a thin film of LDH. The solution was purged with nitrogen gas for 20 min prior to deposition to remove carbon dioxide. The resulting films were rinsed with Millipore water and dried with a stream of nitrogen.

Figure 2.1. Electrochemical Cell for LDH deposition.



2.2.2.2. Cyclic Voltammetry

Figure 2.2. A) Applied waveform for a CV and B) cyclic voltammogram of a classical reversible system.



Cyclic voltammetry (CV) is a technique where the potential is scanned from an initial potential to a maximum potential and then returns back to the initial potential. The applied

potential represents a triangular waveform as shown in Figure 2.2A and current is measured throughout the duration of the experiment. CV is an important technique to investigate the redox behavior of the analyte and its reaction mechanism can be elucidated from the peaks observed. Figure 2.2B shows the voltammogram of a classical reversible system. The formal potential ($E^{0'}$) for a reversible reaction can be calculated from the anodic (E_{pa}) and cathodic peak potentials (E_{pc}) with the following equation:

$$E^{0'} = \frac{E_{pa} + E_{pc}}{2} \quad (\text{Equation 2.8})$$

In this study CVs are used to show the enhanced redox properties of the modified film versus the GCE and determine the optimum pH for analytical determination of GA or CA. CVs are also used to show the effect of scan rate on voltammograms. Peak current (i_p) in a reversible system can be calculated from the number of electrons transferred (n), the electrode area (A), diffusion coefficient (D), scan rate (v) and concentration of species (C) with the Randles-Sevcik equation:

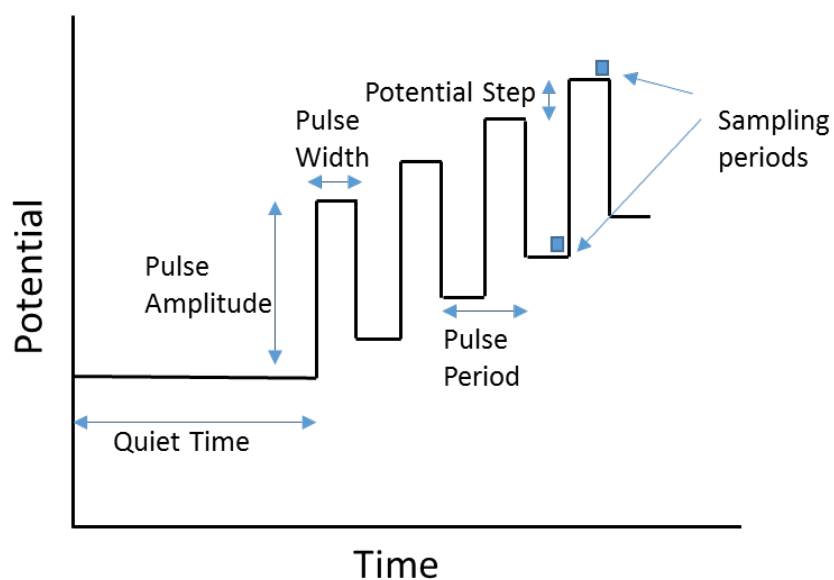
$$i_p = (2.687 \times 10^5) n^{3/2} v^{1/2} D^{1/2} AC \quad (\text{Equation 2.9})$$

CV experiments were performed with an EG&G Princeton Applied Research (PAR) model 273A potentiostat/galvanostat. The same electrochemical cell represented in Figure 2.1 was used for CV experiments. The WE was a bare GCE or LDHf/GCE, a SCE was used as the RE, and a platinum mesh was the CE.

2.2.2.3. Differential Pulse Voltammetry

Differential pulse voltammetry (DPV) is an electroanalytical technique used for the detection of low concentration of analyte. An induction period or quiet time at a constant potential precedes the pulse application. The potential waveform, displayed in Figure 2.3, consists of small pulses of a constant magnitude superimposed over a staircase waveform. The current is sampled twice during each pulse period, once before the pulse and again at the end of the pulse. The difference of the two current measurements is the displayed versus applied potential. It is an effective technique because charging current, caused by the migration of electrolyte ions in response to the charging the electrode, is minimized and therefore the Faradaic current, which is generated by redox reactions, is isolated increasing the signal to noise.

Figure 2.3. DPV waveform.



Differential pulse voltammetry was performed with a Pine WaveDriver 20 bipotentiostat/galvanostat. The same electrochemical cell represented in Figure 2.1. was used for DPV experiments. The WE was the LDHf/GCE, a SCE was used as the RE, and a platinum mesh was the CE.

2.2.2.4. Electrochemical Impedance Spectroscopy

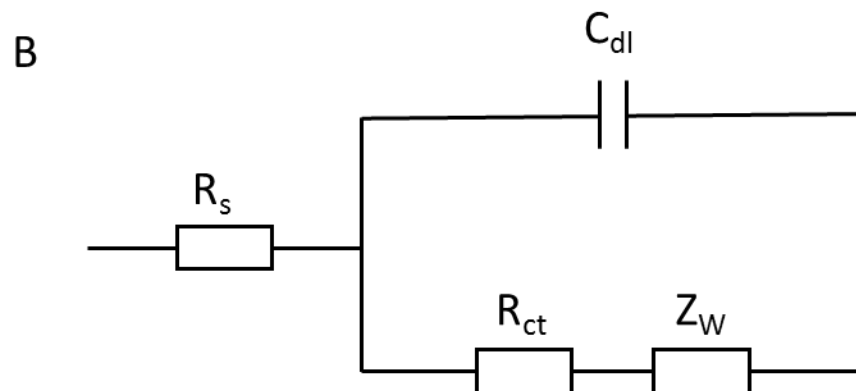
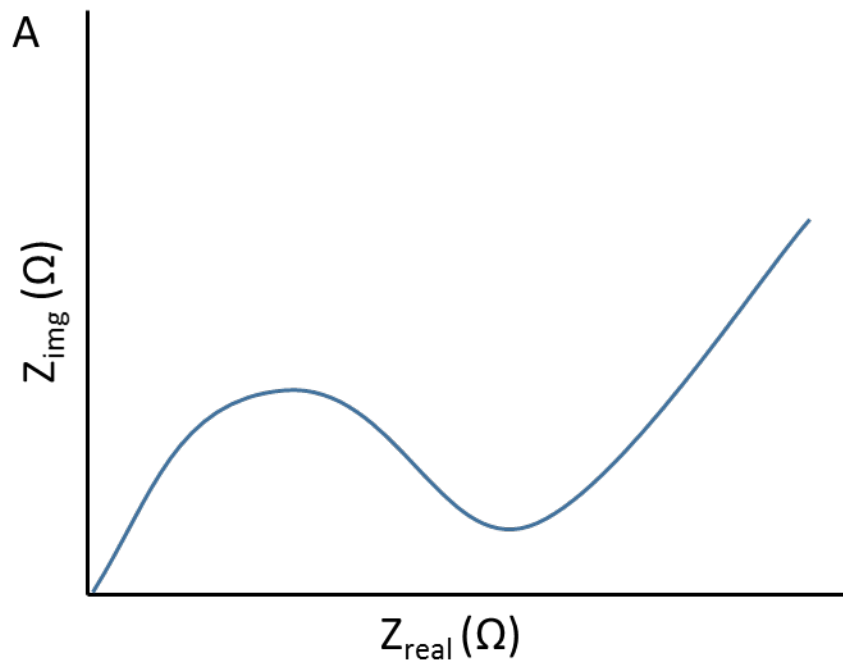
Electrochemical impedance spectroscopy (EIS) is performed by applying a sinusoidal AC potential to the electrochemical cell and measuring the current response. A small excitation signal, between 1-10 mV, is used. The impedance of the system, opposition of a circuit to current when voltage is applied, is measured over a range of frequencies. The current response to the excitation signal is linear but shifted in phase. This phase shift (ϕ) results in impedance (Z) being comprised of a real and also an imaginary component as seen in Equation 2.10.

$$Z(\omega) = \frac{E}{I} = Z_0 \exp(j\phi) = Z_0(\cos\phi + j\sin\phi) \quad (\text{Equation 2.10})$$

A Nyquist plot displays the real component on the x-axis and the imaginary component on the y-axis but does not show the corresponding frequencies. An example Nyquist plot is shown in Figure 2.4A. The semicircle domain at higher frequencies corresponds to the electron transfer process between the redox species and the electrode. The semicircle diameter provides the electron transfer resistance. The greater the semicircle the greater the electron transfer resistance of the sample. The line at lower frequencies represents the diffusion limited process or the diffusion to a large planar electrode. The data in the Nyquist plot can be modeled by a circuit. A common circuit is the Randles circuit shown in Figure 2.4B. The components are the solution resistance (R_s), the double layer capacitance (C_{dl}), the charge

transfer resistance (R_{ct}), and the Warburg diffusion element (Z_W) which models semi-infinite linear diffusion.

Figure 2.4. A) Nyquist Plot and B) Randles Circuit.



Impedance measurements were conducted with a Princeton Applied Research PARSTAT 2273 potentiostat/galvanostat/FRA. Impedance experiments were carried out in 5×10^{-3} M $\text{K}_3[\text{Fe}(\text{CN})_6]$ and 0.1 M KCl. The AC amplitude was 5 mV and the frequency range was 50 mHz to 100 kHz. All impedance measurements were carried out at open circuit potential and the data was modeled with ZSimpWin software. The Nyquist plots were modeled after a simple Randles circuit. The WE was a bare GCE or LDHf/GCE, a SCE was used as the RE, and a platinum wire was the CE.

2.2.3. Structural Characterization of Deposited Films

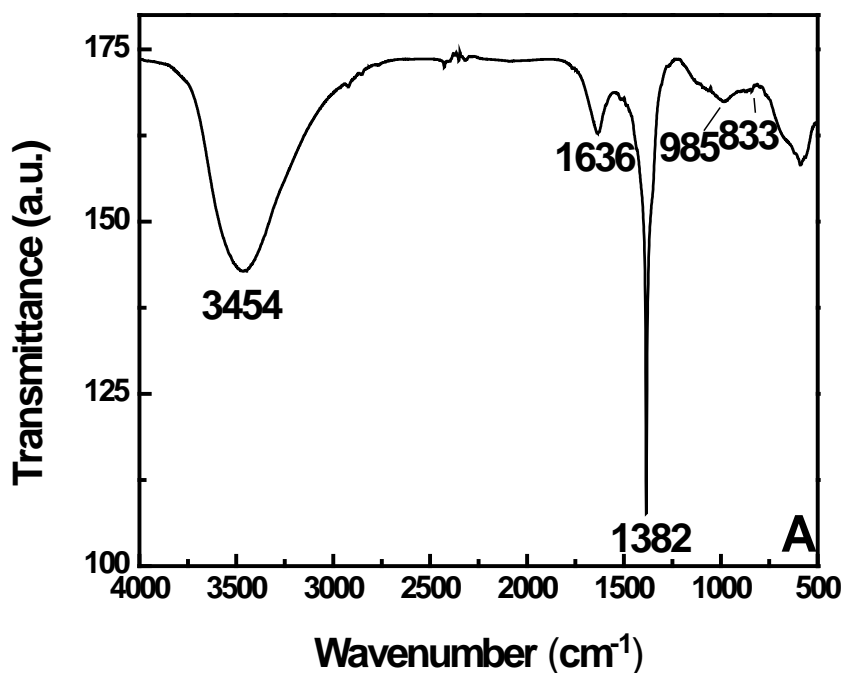
Scanning electron microscopy (SEM) images were collected using an FEI Quanta 200 ESEM. An Everhart-Thornley Detector with a Photomultiplier Tube (EDT-PMT) was employed in high vacuum at a spot size of 3.0 and high voltage of 25 kV. X-ray diffraction (XRD) measurements were conducted after each deposition. For all samples, diffractograms were obtained with a Siemens D500 X-ray Diffractometer (24 mA and 35 kV) in a standard Bragg-Brentano configuration. Each sample was scanned from 2.0° to 50° (2θ), with a step size of 0.05° and a dwell time of 1.0 second, using $\text{CuK}\alpha$ radiation ($\lambda = 1.540562 \text{ \AA}$). A Perkin Elmer Spectrum One FTIR Spectrophotometer (Waltham, MA, USA) was used to analyze the composition of the LDH. KBr pressed pellets were used to collect background spectra. The samples were mixed and ground to ensure homogeneity with KBr to give a 1:100 sample to KBr ratio then pressed into an 8 mm FTIR pellet die. Each sample was scanned at a range of $4000 - 450 \text{ cm}^{-1}$ wavenumbers.

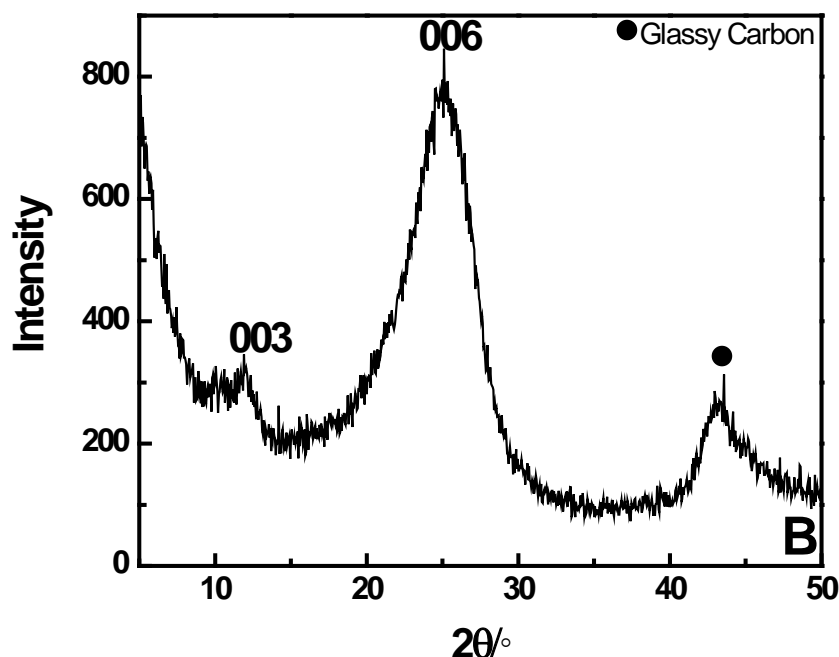
2.3. Results and Discussion

2.3.1. Structural Characterization

The FTIR spectrum for the electrochemical sensor shown in Figure 2.5A confirms the presence of LDH with only nitrate ions and water in the interlayer regions. The broad peak at 3454 cm^{-1} corresponds to the O-H stretching of the LDH layer and interlayer water molecules. The peak at 1636 cm^{-1} represents the bending vibration of interlayer region water molecules. The peaks at 1382 and 833 cm^{-1} are a result of the asymmetric stretching and out-of-plane symmetric deformation of nitrate ions in the interlayer region [39, 45]. The broad peak at 985 cm^{-1} is associated with Al-OH deformation [46].

Figure 2.5. A) FT-IR spectrum of Zn-Al-NO₃ LDHf/GCE and B) XRD pattern of Zn-Al-NO₃ LDHf/GCE.



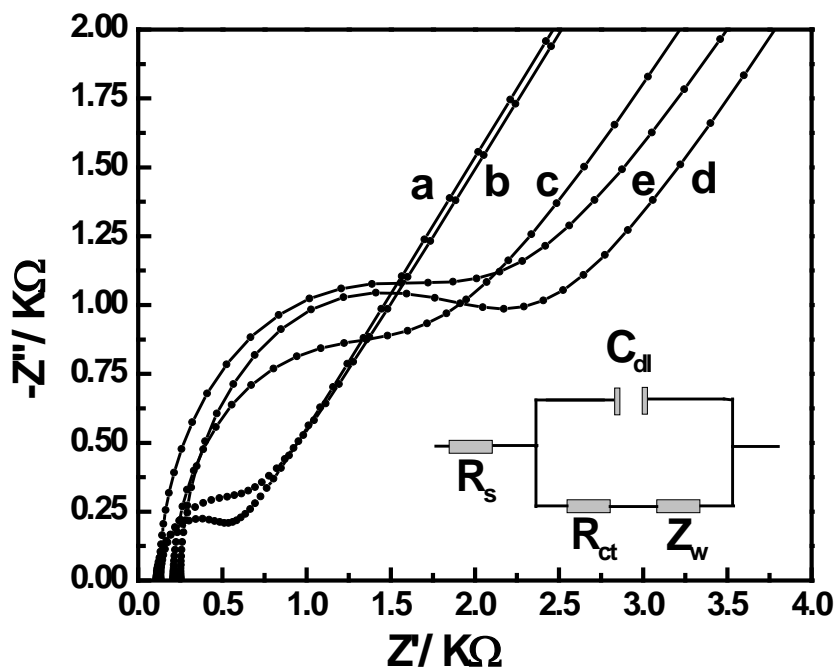


The typical XRD pattern of the deposited Zn-Al-NO₃ LDH is shown in Figure 2.5B. The two peaks at 11° and 26.5° correspond to the 003 and 006 basal planes of the LDH, respectively. The peak at 43.6° corresponds to the (10) reflection of glassy carbon. The Zn-Al-NO₃ LDH d-spacing was 8.04 Å, which is in agreement with previous studies [39].

Electrochemical impedance spectroscopy was performed on films after the LDHf deposition process. There are two components to the EIS spectra: a semicircle domain at higher frequencies and a line at lower frequencies. The semicircle domain corresponds to electron-transfer limited process and the diameter of the semicircle provides the electron-transfer resistance, R_{et} . The linear domain at lower frequencies represents the diffusion limited process. The bare GCE (curve a) in Figure 2.6 exhibits a very small semicircle domain which conveys that there is very little resistance to interfacial electron transfer between the redox probe in solution and the electrode support. The deposition of LDHf on the electrode surface results in larger semicircles (curves b-e). The formation of the nonconducting film creates a

barrier for electron transfer on the surface increasing the electron transfer resistance. Longer deposition times result in higher interfacial electron transfer resistance [43]. The thickness of the 60 s film was determined to be 800-1200 nm by side profile SEM. Longer depositions or thicker films would result in decreased peak currents and poorer detection limits for modified electrodes.

Figure 2.6. Nyquist plots obtained for a) bare GC electrode and b)-e) LDHf/GCEs at deposition times of 30, 60, 90 and 120s, respectively.

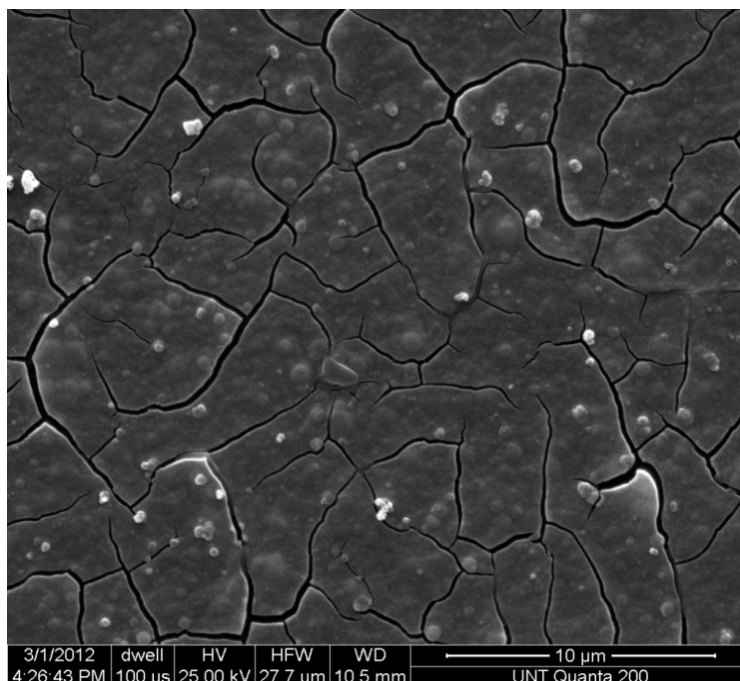


2.3.2. Film Morphology

Figure 2.7 shows an SEM image of a glassy carbon electrode with a thin film of electrodeposited Zn-Al-NO₃ LDH. The image shows a smooth and featureless surface for the

film. Fractures in the film are a result of shrinkage when films are removed from plating solution and dried.

Figure 2.7. SEM image of LDHf/GCE.



2.3.3. Voltammetric Response of LDHf/GCE to GA and CA

Figure 2.8A shows 3 consecutive CVs of GA at a bare GCE. There are two oxidation peaks in each voltammogram, the first is much more prominent than the second. The two oxidation peaks indicate that the electrochemical oxidation of GA is an ECEC reaction [21]. The peak current decreases as the number of cycles increases suggesting that the oxidized GA is fouling the electrode. Figure 2.8B shows 3 consecutive CVs of CA at a bare GCE. There is only one oxidation peak, but the mechanism has been determined to be ECEC also [33]. The peak current does not decrease during the 3 consecutive CVs indicating that CA does not foul the electrode.

Figure 2.8. Consecutive CV cycles of 0.1 mM (A) GA and (B) CA at a bare GCE.

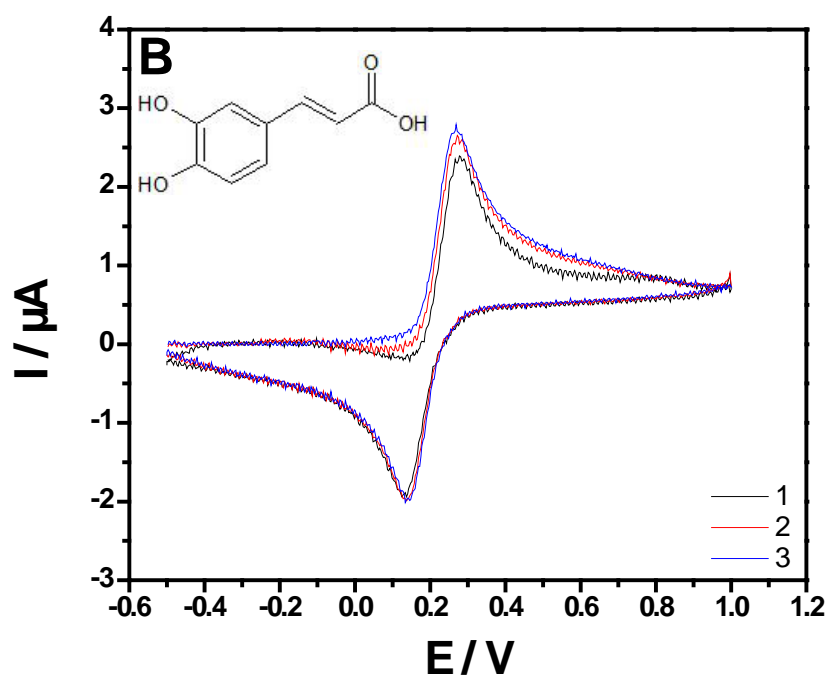
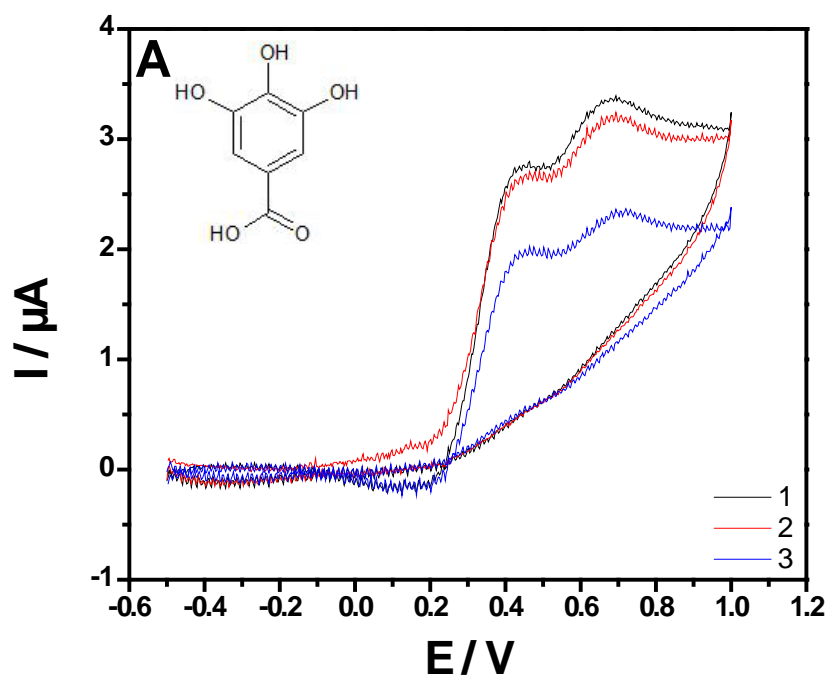


Figure 2.9. CVs of 0.1 mM (A) GA and (B) CA at (a) bare GCE and (b) LDHf/GCE.

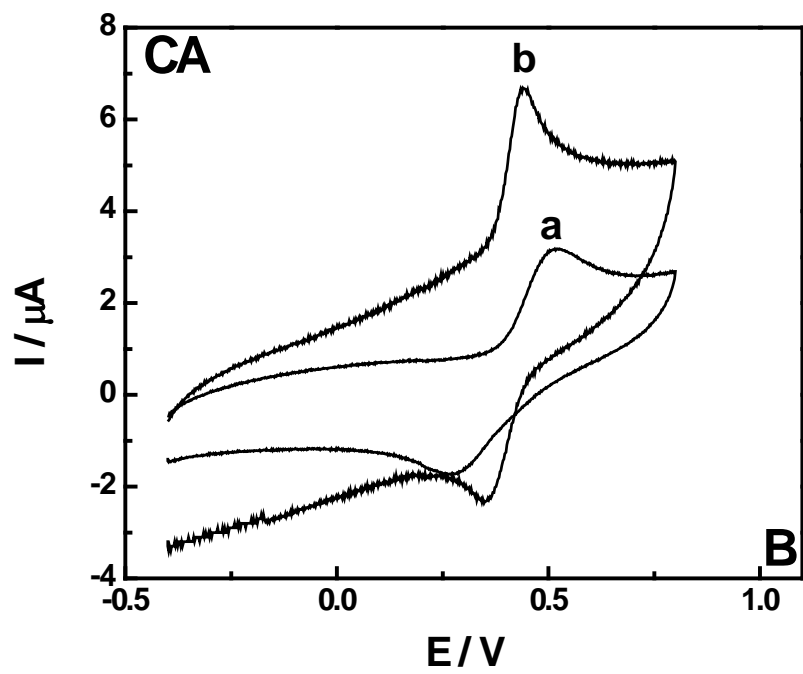
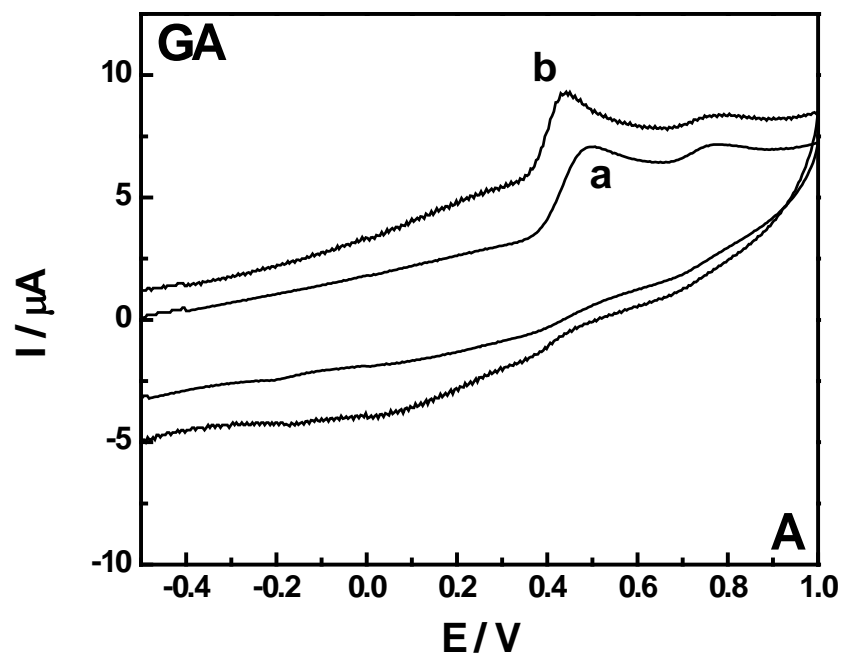


Figure 2.9A is a CV of GA at a bare GCE (curve a) and an LDHf/GCE (curve b). It is obvious that both oxidation peak currents are greater for the LDHf/GCE than the GCE. The increase in peak current may be due to higher surface area and adsorptive ability of the Zn-Al-NO₃ film. More adsorption of GA indicates higher accumulation efficiency and increases surface concentration. This indicates that analyte can be preconcentrated on the surface of the modified electrode in order to improve quantitative analysis. Negatively charged phenolic acids (GA or CA) can participate in anion exchange with surface and intercalated nitrate species in LDH. Intercalation of the analyte into the LDH film is possible but very unlikely. Furthermore, ligand exchange or surface complexation reactions between Al-OH and negatively charged phenolic acids could occur [47]. The modified electrode is more sensitive to GA than the bare GCE. Furthermore, the oxidation peak occurs at a lower potential (0.4419 vs. 0.5059 V) when compared to the unmodified electrode. The decrease in overpotential indicates that LDH acts as a mediator for the electrocatalytic oxidation of GA.

Figure 2.9B shows CVs for CA at a bare GCE (curve a) and an LDHf/GCE (curve b). The redox peak currents are sharper and significantly enhanced for the LDHf/GCE, especially the oxidation peak, which indicates that the Zn-Al LDH film increases the surface area and adsorptive ability. Also, the ΔE_p is smaller for the LDHf/GCE (160 mV) than for the unmodified GCE (259 mV). This decrease in ΔE_p demonstrates the improvement in the reversibility of the electrochemical reaction.

2.3.4. Effect of Scan Rate

The effect of scan rate (v) on the peak current (i_{pa}) was observed in Figure 2.10. The peak current increased linearly with $v^{1/2}$ (50-400 mV/s) for both analytes indicating a diffusion-controlled mechanism dominates. Log i vs log v were also plotted for the oxidation peaks of the analytes in Figure 2.11 producing the equations $\log i_p = 0.56 \cdot \log v - 6.16$ ($R^2 = 0.9992$) and $\log i_p = 0.66 \cdot \log v - 6.63$ ($R^2 = 0.9909$) for GA and CA, respectively. Slopes with values of 0.5 indicate diffusion controlled processes and slopes with values of 1.0 indicate adsorption based processes. Intermediate values indicated mixed processes. The GA slope of 0.56 is close to the theoretical value of 0.5 which confirms the presence of a diffusion controlled reaction. The CA slope of 0.66 indicates mixed control with diffusion providing greater control than adsorption.

2.3.5. Effect of pH

The effect of pH on the response of GA and CA was observed by cyclic voltammetry in 0.1 M PBS at a pH range from 3 to 9 in Figure 2.12. GA has pKa's of 4.0, 8.7, 11.4, and >13 [48,49]. CA has pKa's of 4.41, 8.64, and 12.5 [50]. The dominant species of both analytes are shown in their respective pH ranges in Figure 2.12. Higher peak values were obtained at pH 3 for both analytes. These results agree with previous studies of CA and GA at glassy carbon electrodes [18, 50]. The lower pH limit was deemed to be 3 due to protonation of the hydroxide groups, which results in metal bonds breaking and the dissolution of metal cations at lower pHs [51].

Figure 2.10. Cyclic voltammograms of 0.1 mM (A) GA and (B) CA in 0.1 M pH 3 PBS at a LDHf/GCE at different scan rates (50, 100, 150, 200, 250, 300, 350, 400) and at 50 mv/s in the absence of analyte.

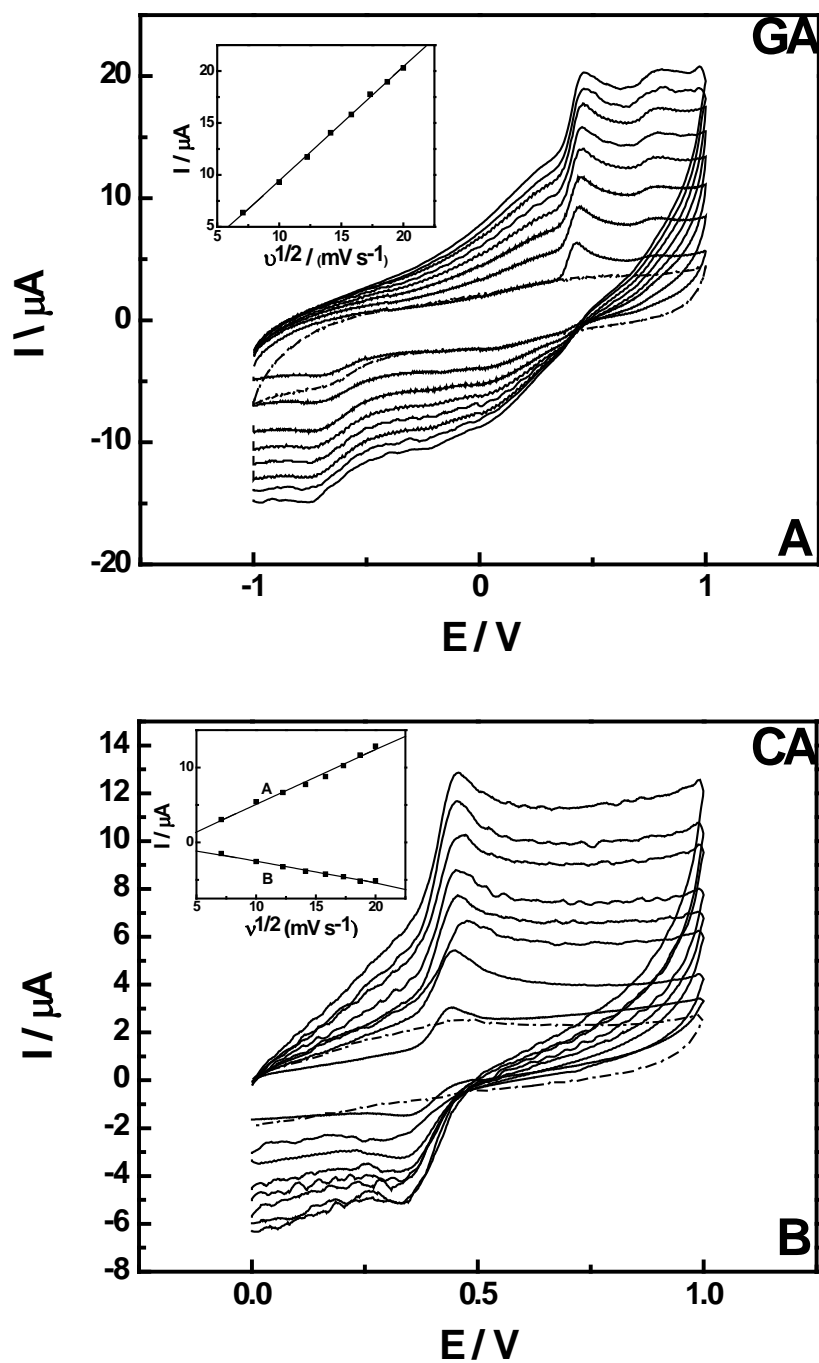


Figure 2.11. Log i vs. log v was plotted for the oxidation peaks of (A) GA and (B) CA.

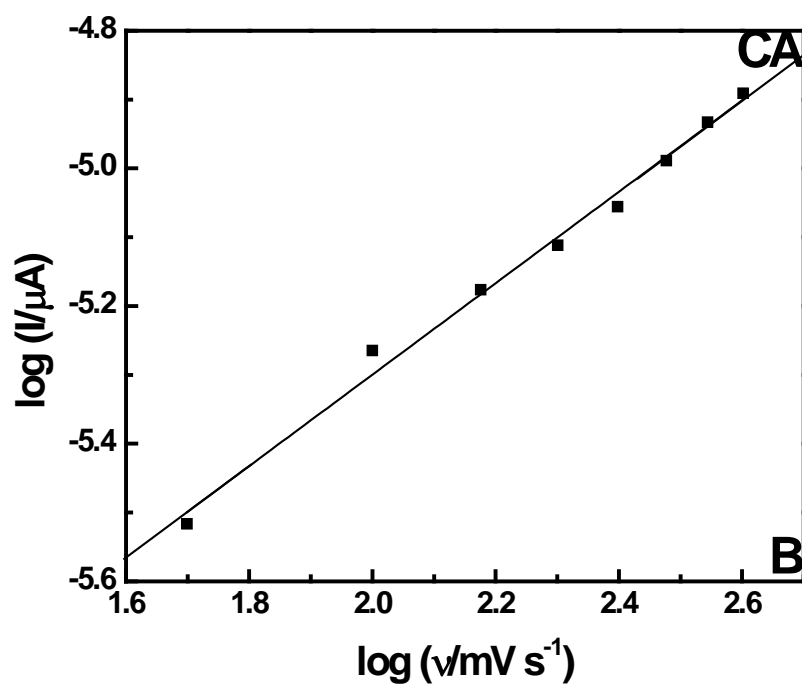
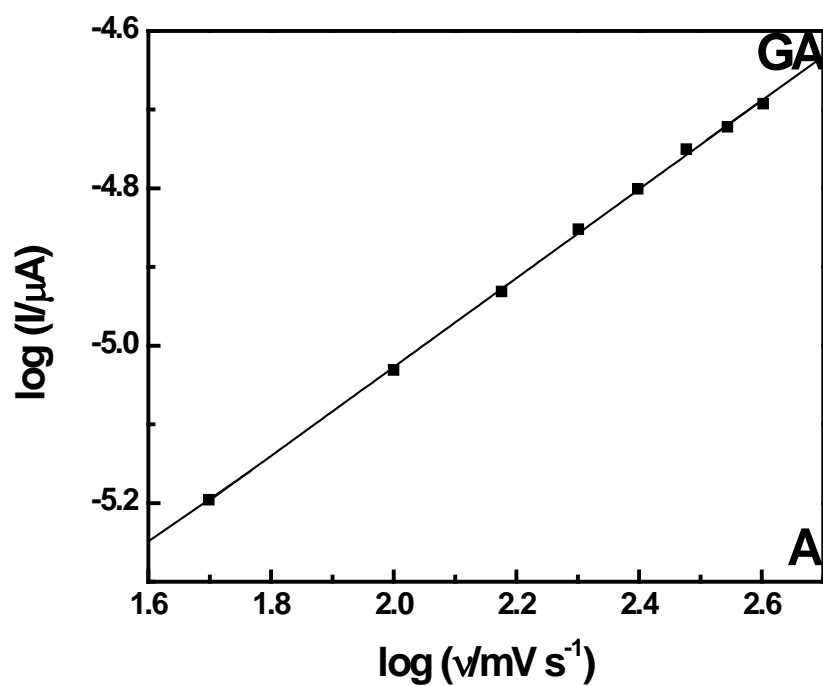
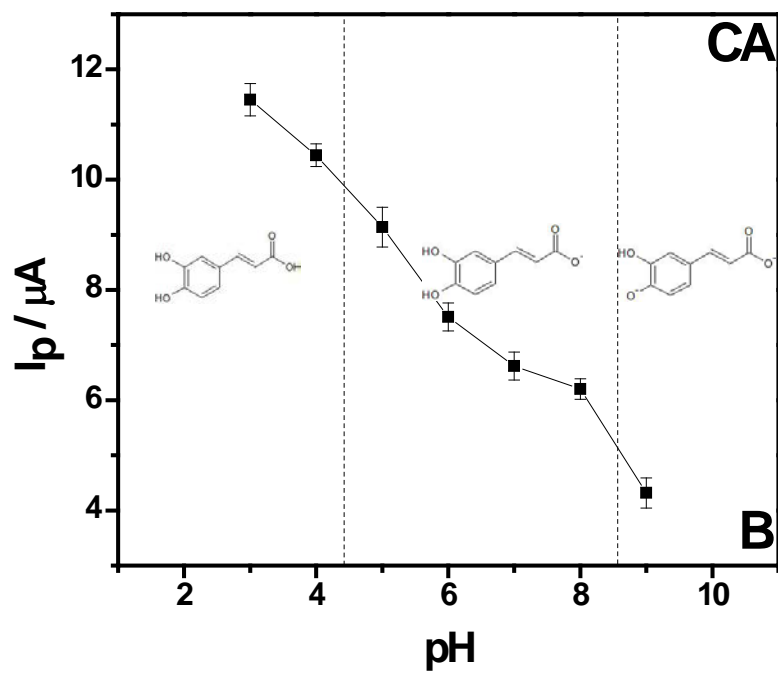
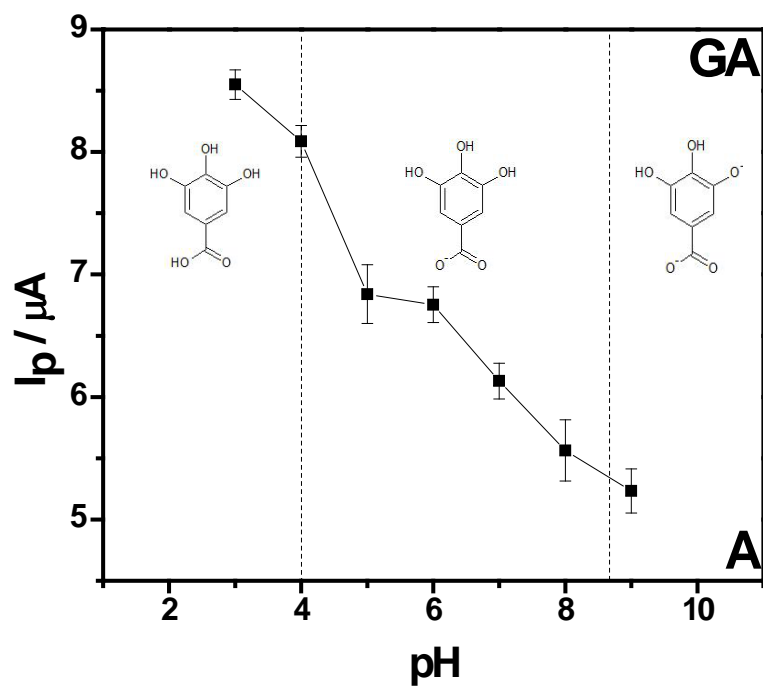


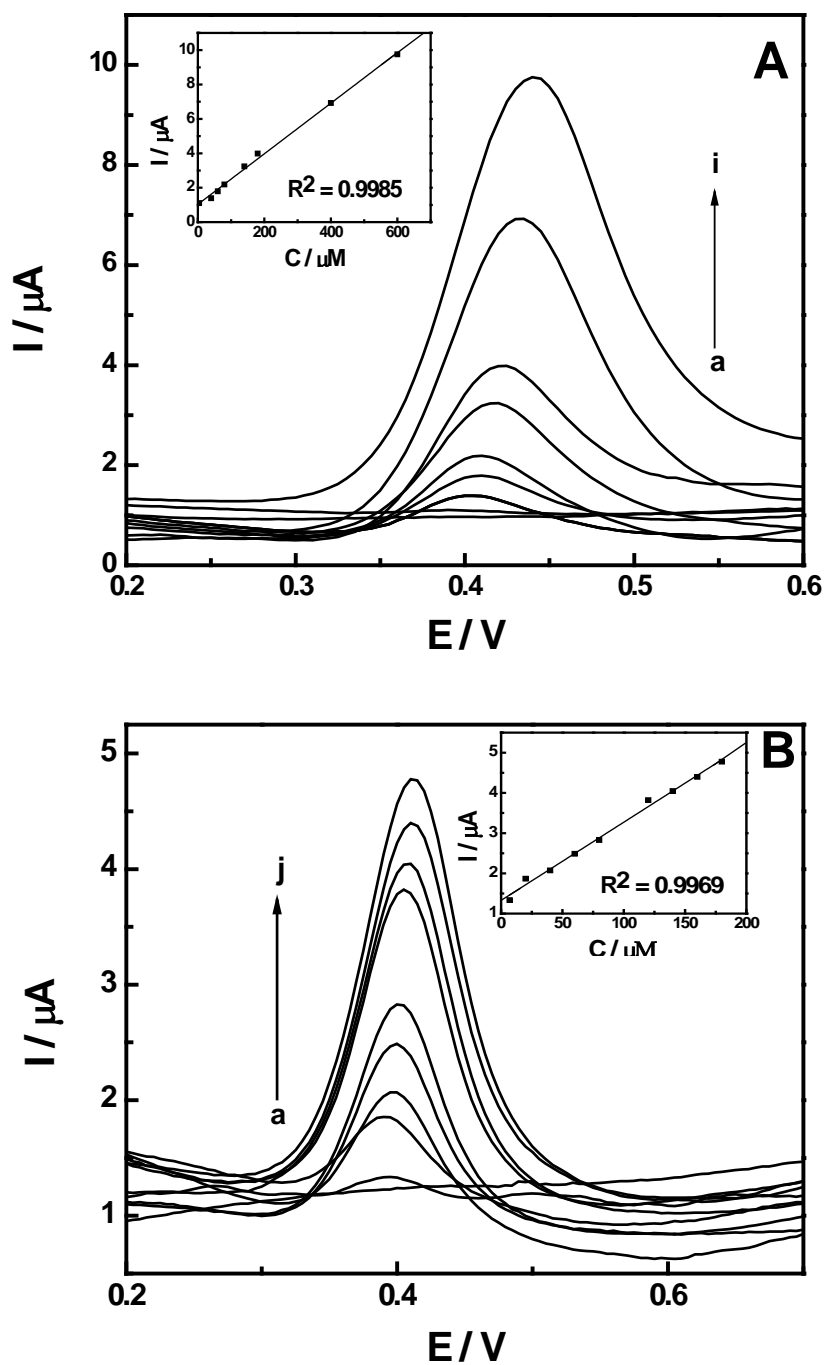
Figure 2.12. Peak current from cyclic voltammograms of (A) GA and (B) CA at various pHs.



2.3.6. Linear Range and Limit of Detection

Determination of the limits for detection of GA concentration was performed with DPV. A deposition time of 60 sec was found to be optimal for the determination of GA. This time is in agreement with previous studies of similar phenolic compounds [43, 44]. The DPV experiments were conducted at an optimal preconcentration time of 100 sec at open circuit potential. Figure 2.13A shows that the anodic peak current (i_p) was also proportional to GA concentration. The equation of the DPV plot for GA is $i_p (\mu A) = 0.0147C_{GA} (\mu M) + 1.03$. The DPV current for GA has a linear concentration range of 4 μM to 600 μM with a correlation coefficient of 0.9985, a detection limit of 1.6 μM and a quantification limit of 4.3 μM . The same optimal conditions were used for the determination of CA. Figure 2.13B shows that the anodic peak current (i_p) was also proportional to the CA concentration. The equation of the DPV plot for CA is $i_p (\mu A) = 0.0194 C_{CA} (\mu M) + 1.33$. The DPV current for CA has a linear concentration range of 7 μM to 180 μM with a correlation coefficient of 0.9969, a detection limit of 2.6 μM and a quantification limit of 18.7 μM . Detection limit was determined by the average of the blank plus 3 times the standard deviation of the blank ($y_{LOD} = y_{blank} + 3*SD_{blank}$) and quantification limit was determined by the average of the blank plus 10 times the standard deviation of the blank ($y_{LOQ} = y_{blank} + 10 *SD_{blank}$). The blank was measured 10 times. The limit of detection for gallic acid was not as great as recent literature but the linear range was greater than or equal to most recent studies [18,22,23,52,53]. The caffeic acid detection limit was inferior to most recent studies while the linearity range was comparable or greater than most [30,34,35].

Fig. 2.13. The differential pulse voltammograms of (A) GA at a) 0, b) 4, c) 40, d) 60, e) 80, f) 140, g) 180, h) 400, i) 600 μM and (B) CA at a) 0, b) 7, c) 20, d) 40, e) 60, f) 80, g) 120, h) 140, i) 160, j) 180 μM . The inset shows the plot of the DPV peak current vs. the concentration. Amplitude: 0.05 V; pulse width: 0.06s; pulse period: 0.2s.



2.3.7. Interference, Stability and Reproducibility

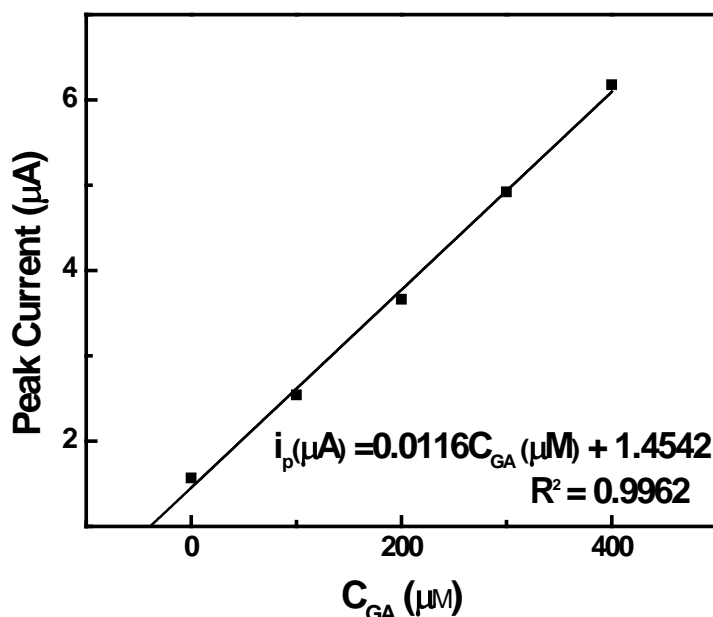
Commonly interfering substances were investigated to assess the sensor's response. A relative error of 10% was considered tolerable. The concentration of GA was kept at 0.1 mM. No significant interference was observed from a 100-fold concentration addition of methanol, glucose, alanine, caffeine, resorcinol, F^- , NH_4^+ , PO_4^{3-} , Na^+ , Cl^- , NO_3^- , or K^+ . The stability of the modified electrode was studied by measuring the electrode response with 0.1 mM GA for 14 days. The modified electrode retained 90% of its initial response after it was kept in the refrigerator at 4° C for 1 week and 80% after 2 weeks. The reproducibility of the sensor was determined by obtaining the relative standard deviation (RSD) from five parallel measurements of 0.1 mM GA at different electrodes. The RSD was 1.58% demonstrating reproducibility for the LDHf/GCE. The stability of the electrode is comparable to other studies while the reproducibility is unmatched [22,23,52,53].

2.3.8. Analytical Application

The modified electrode was used to determine the GA content in green tea samples. The green tea samples were prepared from packets of dried tea leaves (Carrington Tea). The dry leaf content of the packet weighed 1.7499 g. The GA was extracted by submerging the tea packet into 200 ml of distilled water at 90°C. The solution was stirred for 5 min with the submerged tea packet. The packet was removed and the resulting solution was filtered. A standard addition method was conducted to determine the concentration of GA in green tea samples for pH 3 phosphate buffer. The obtained peak currents in DPV measurements are displayed in the standard addition plot in Figure 2.14. The peak current increased with the

standard addition of GA and obeyed the equation: $i_p (\mu A) = 0.0116C_{GA} (\mu M) + 1.4542$, $R^2=0.9962$, $n=5$, which by extrapolation indicates that the GA concentration in green tea is 67.02 ± 5.87 mg/g of dried tea leaves (or 58.97 ± 5.14 mg/100ml). The results obtained were greater than the established value in literature [54] which indicates that other phenolic compounds (epicatechin (EC), epigallocatechin (EGC), epicatechin gallate (ECG), and epigallocatechin gallate (EGCG)) oxidize at the same or very similar potential. The modified electrode is not suited for discriminating between GA and some of the phenolic compounds found in green tea. However, if the value is designated as a measurement of total phenolic content then it is within the range established by a previous study (24.2 -101.3 mg/100 ml) [55]. Therefore the modified electrode may be a suitable alternative to the Folin-Ciocalteu reagent determining total phenolic content in a sample.

Figure 2.14. Calibration curve of the standard addition method for GA determination in green tea by DPV at LDHf/GCE.



2.4. Chapter Conclusions

In this work, Zn-Al-NO₃ layered double hydroxide film was electrochemically synthesized on a glassy carbon substrate. The results indicated that after the electrode modification, the oxidation currents of GA and CA were greatly enhanced. The reversibility of CA was also improved. The modified electrode was used to study the oxidation of GA and determination of GA content in tea samples. The sensor demonstrated stability, reproducibility and anti-interference capabilities. These characteristics combined with its low cost and ease of fabrication make it a suitable sensor for further studies in determining phenolic content in various foods but not for GA alone.

2.5. References

- [1] R. Arakawa, M. Yamaguchi, H. Hotta, T. Osakai, T. Kimoto, *J. Am. Soc. Mass Spectr.*, 2004, 15, 1228-1236.
- [2] A. Finger, S. Kuhr, U.H. Engelhardt, *J. Chrom.*, 1992, 624, 293-315.
- [3] S. Sellappan, C. C. Akoh, G. Krewer, *J. Agric Food Chem.*, 2002, 50, 2432–2438.
- [4] K. W. Lee, Y. J. Kim, H. J. Lee, C. Y. Lee, *J. Agric Food Chem.*, 2003, 51, 7292-5.
- [5] R. M. Muir, A. M. Ibáñez, S. L. Uratsu, E. S. Ingham, C. A. Leslie, G. H. McGranahan, N. Batra, S. Goyal, J. Joseph, E. D. Jemmis, A. M. Dandekar, *Plant Mol Biol.*, 2011, 75, 555-565.
- [6] M. Kassim, M. Achoui, M. R. Mustafa, M. A. Mohd, K. M. Yusoff, *Nutr. Res.*, 2010, 30, 650-659.
- [7] A. Borges, C. Ferreira, M. J. Saavedra, M. Simões, *Microb. Drug Resist.*, 2013, 19, 256-65.

- [8] A. Abdelwahed, I. Bouhlel, I. Skandrani, K. Valenti, M. Kadri, P. Guiraud, R. Steiman, A. Mariotte, K. Ghedira, F. Laporte, M. Dijoux-Franca, L. Chekir-Ghedira, *Chem.-Biol. Interact.*, 2007, 165, 1-13.
- [9] L. Cedó, A. Castell-Auví, V. Pallarès, A. Macià, M. Blay, A. Ardévol, M. J. Motilva, M. Pinent, *Nutr. Cancer*, 2014, 66, 88-96.
- [10] J. H. Kim, B. K. Lee, K. W. Lee, H. J. Lee, *J. Nutr. Biochem.*, 2009, 20, 149-54.
- [11] M. N Clifford, *J. Sci. Food Agr.*, 2000, 80, 1033-1043.
- [12] C. B. Faulds, G. Williamson, *J. Sci. Food Agric.*, 1999, 79, 393-395.
- [13] A. B. Moghaddam, M. R. Ganjali, R. Dinarvand, P. Norouzi, A. A. Saboury, A. A. Moosavi-Movahedi, *Biophys. Chem.*, 2007, 128, 30-37.
- [14] J. C. Ye, M. W. Hsiao, C. H. Hsieh, W. C. Wu, Y. C. Hung, W. C. Chang, *Taiwan J. Obstet. Gynecol.*, 2010, 49, 266-271.
- [15] D. P. Santos, M. F. Bergamini, A. G. Fogg, M. Valnice, B. Zanoni, *Microchim. Acta*, 2005, 151, 127-134.
- [16] T. Nagaoka, A. H. Banskota, Y. Tezuka, I. Saiki, S. Kadota, *Bioorg. Med. Chem.*, 2002, 10, 3351-3359.
- [17] S. G. Dmitrienko, O. M. Medvedeva, A. A. Ivanov, O. A. Shpigun, Y. A. Zolotov, *Anal. Chim. Acta*, 2002, 469, 295-301.
- [18] R. Abdel-Hamid, E. F. Newair, *J. Electroanal. Chem.*, 2013, 704, 32-37.
- [19] I. Novak, M. Šeruga, Š. Komorsky-Lovrić, *Food Chem.*, 2010, 122, 1283-1289.
- [20] H. Wang, G. J. Provan, K. Helliwell, *J. Pharm. Biomed. Anal.*, 2003, 33, 539-544.
- [21] R. Abdel-Hamid, E. F. Newair, *J. Electroanal. Chem.*, 2011, 657, 107–112.

- [22] S. M. Ghoreishi, M. Behpour, M. Khayatkashani, M. H. Motaghedifard, *Anal. Methods*, 2011, 3, 636-645.
- [23] J. H. Luo, B. L. Li, N. B. Li, H. Q. Luo, *Sensors Actuat B-Chem* 2013, 186, 84–89.
- [24] D. Fracassetti, N. Lawrence, A. G. J. Tredoux, A. Tirelli, H. H. Nieuwoudt, W. J. Du Toit, *Food Chem.*, 2011, 128, 1136-1142.
- [25] K. Skalicka-Wozniak, E. Melliou, O. Gortzi, K. Glowinski, I. B. Chinou, *Z. Naturforsch. C*, 2007, 62, 797-800.
- [26] X. Wang, J. Pang, J. A. Maffucci, D. S. Pade, R. A. Newman, S. M. Kerwin, P. D. Bowman, S. Stavchansky, *Biopharm. Drug Dispos.*, 2009, 30, 221-228.
- [27] X. B. Luo, B. Chen, S. Z. Yao, J. G. Zeng, *J. Chromatogr. A*, 2003, 986, 73-81.
- [28] C. Tang, O. S. Sojinu, *Talanta*, 2012, 94, 232-239.
- [29] P. Raptá, V. Misik, A. Stasko, I. Vrabel, *Free Radical Biol. Med.*, 1995, 18, 901-908.
- [30] K. Tyszczyk, A. S. Kaminska, A. Wozniak, *Food Chem.*, 2011, 125, 1498-1503.
- [31] A. S. Arribas, M. Martinez-Fernandez, M. Moreno, E. Bermejo, A. Zapardiel, M. Chicharro, *Food Chem.*, 2013, 136, 1183-1192.
- [32] A. Curulli, G. di Carlo, G. M. Ingo, C. Riccucci, D. Zane, C. Bianchini, *Electroanalysis*, 2012, 24, 897-904.
- [33] H. Hotta, M. Ueda, S. Nagano, Y. Tsujino, J. Koyama, T. Osakai, *Anal. Biochem.*, 2002, 303, 66-72.
- [34] F. R. F. Leite, W. de J. R. Santos, L. T. Kubota, *Sensors Actuat B-Chem.*, 2014, 193, 238– 246.
- [35] H. Filik, G. Çetintaş, A. A. Avan, S. Aydar, S. N. Koç, İsmail Boz, *Talanta*, 2013, 116, 245–250.
- [36] J. Wang, R. P. Deo, M. Musameh, *Electroanalysis*, 2003, 15, 1830–1834.

- [37] F. Cavani, F. Trifiro, A. Vaccari, *Catal. Today*, 1991, 11, 173-301.
- [38] H. Zhao, K.L. Nagy, *J. Colloid Interf. Sci.*, 2004, 274, 613-624.
- [39] M. S. Yarger, E. M. P. Steinmiller, K. Choi. *Inorg. Chem.*, 2008, 47, 5859-5865.
- [40] G. H. A. Therese, P. V. Kamath, *Chem. Mater.*, 2000, 12, 1195-1204.
- [41] M. Montia, P. Benitoa, F. Basilea, G. Fornasaria, M. Gazzanob, E. Scavettaa, D. Tonellia, A. Vaccaria, *Electrochim. Acta*, 2013, 108, 596-604.
- [42] H. Yin, L. Cui, S. Ai, H. Fan, L. Zhu, *Electrochim. Acta*, 2010, 55, 603–610.
- [43] M. Li, F. Ni, Y. Wang, S. Xu, D. Zhang, S. Chen, L. Wang, *Electroanalysis*, 2009, 21, 1521-1526.
- [44] F. Ni, Y. Wang, D. Zhang, F. Gao, M. Li, *Electroanalysis*, 2010, 22, 1130-1135.
- [45] J. T. Klopogge, R. L. Frost, Infrared and Raman spectroscopic studies of layered double hydroxides (LDHs), in V. Rives (Ed.), *Layered Double Hydroxides: Present and Future*, Nova Science Publishers, Inc., New York, 2001, pp. 139-192.
- [46] J. T. Klopogge, R. L. Frost, L. Hickey, *J. Raman Spectrosc.*, 2004, 35, 967-974.
- [47] S. Vreysen, A. Maes. *Appl. Clay Sci.*, 2008, 38, 237–249.
- [48] N. P. Slabbert. *Tetrahedron*, 1977, 33, 821-824.
- [49] H. F. Ji, H. Y. Zhang, L. Shen. *Bioorg. Med. Chem. Lett.*, 2006, 16, 4095-4098.
- [50] C. Giacomelli, K. Ckless, D. Galato, F. Miranda, A. Spinelli, *J. Braz. Chem. Soc.*, 2002, 13, 332-338.
- [51] S. J. Santosa, S. Sudiono, Z Shiddiq, *J. Ion Exchange*, 2007, 18, 322-327.
- [52] M. Di Fuscoa, C. Tortolinia, D. Deriua, F. Mazzei, *Talanta*, 2010, 81, 235–240.

- [53] L. P. Souza, F. Calegari, A. J. G. Zarbin, L. H. Marcolino-Júnior, M. F. Bergamini, *J. Agric. Food Chem.*, 2011, 59, 7620–7625.
- [54] C. Cabrera, R. Giménez, M. C. López, *J. Agric. Food Chem.*, 2003, 51, 4427-35.
- [55] M. Liebert, U. Licht, V. Bohm, R. Bitsch, *Z. Lebensm. Unters. Forsch. A*, 1999, 208, 217-220.

CHAPTER 3

CORROSION RESISTANCE OF ELECTROCHEMICALLY SYNTHESIZED MODIFIED ZACCAGNAITE FILMS ON STAINLESS STEEL

3.1. Introduction

Steels are utilized in many applications including architectural/civil engineering, medical equipment, oil and gas, food and drink processing/storage, water treatment/transport, automotive and pharmaceutical industries [1-7]. Stainless steel has good corrosion resistance in various corrosive environments, with resistance derived from its chromium component. A minimum of 10.5% chromium allows for the formation of a protective chromium oxide layer. The oxide layer is self-repairing in oxygen rich environments [8]. However, stainless steels are susceptible to localized corrosion due to attack by chloride ions [9, 10]. Stainless steels are often coated to prolong lifetime when utilized in a chloride environment [11, 12]. Many types of coatings have been developed and recently there has been a shift towards more environmentally friendly coatings. There have been several studies showing the potential of using layered double hydroxides (LDHs) as coatings for metal or alloy substrates [13-15].

LDHs are a class of layered anionic clays derived from the natural clay hydrotalcite. They are comprised of metal hydroxide layers with anions and water in the interlayer regions between the metal sheets. The positive charge is derived from the substitution of divalent ions with trivalent ions in brucite-like metal hydroxide. This positive charge is balanced by interlayer anions which can be exchanged. LDH is represented by the formula $[M^{2+}_{1-x}M^{3+}_x(OH)_2][A^{n-}]_x/n \cdot zH_2O$, where M^{2+} and M^{3+} are divalent and trivalent metal cations, respectively. A^{n-} is an anion such as CO_3^{2-} or NO_3^- , x is the $M^{3+}/(M^{2+} + M^{3+})$ ratio and z is the number of associated water

molecules [16]. A divalent to trivalent ratio ($M^{2+}:M^{3+}$) between 4:1 and 2:1 is considered the range for a material to be reliably classified as a LDH although there are exceptions [16-19].

Because of their anion exchange properties, LDHs can be used in corrosion resistant coatings. Zhang et al. spin-coated LDH films onto a magnesium alloy substrate improving its corrosion protection [20]. However this protection deteriorated when immersed in NaCl solution due to film defects. A one-step hydrothermal crystallization method for Zn-Al- NO_3 /alumina bilayer film was developed [21]. In-situ growth of the film allows for greater adhesion to the substrate because of formation of chemical bonds. Mg-Al hydrotalcite conversion coatings have been generated in-situ utilizing the substrate AZ31 Mg alloy as the source of Mg ions [22, 23]. The growth mechanism along with the corrosion mechanism for the Mg-Al hydrotalcite films have been studied on magnesium alloys [24, 25]. These conversion films have also been modified with phytic acid to improve corrosion resistance [26]. The resistance of these films degraded during immersion testing. Mg-Al- CO_3 LDH films were synthesized by a combined co-precipitation and hydrothermal process on AZ31 alloy [27]. These films increased the corrosion protection of the substrate but required a 48 h synthesis, 12 h aging process and a 24-48 heat treatment in an autoclave. Films containing both crystalline $Mg(OH)_2$ and Mg-Al- CO_3 LDH were generated by a steam coating method on magnesium alloy AZ31 at temperatures up to 453 K [28]. These films displayed excellent corrosion resistance in 5 wt.% NaCl solution. Films grown by in-situ crystallization have exhibited self-healing properties in 3.5 wt.% NaCl [29].

Electrochemical deposition is another technique for the in-situ generation of films on various substrates [30]. Electrodeposition of thin films is an attractive technique because of the

low cost, simple setup, short duration and ability to deposit on large or unconventional substrate shapes [31]. Furthermore, there is greater control over film properties and deposition rate by changing the deposition parameters [32, 33]. Zaccagnaite is a hexagonal Zn-Al-LDH, a substituted variant of hydrotalcite, and represented by the formula $\text{Zn}_4\text{Al}_2(\text{OH})_{12}[\text{CO}_3] \cdot 3\text{H}_2\text{O}$ [19]. It has a metal ratio of 2:1 in natural mineral formations and various ratios have been synthetically prepared. Yarger et al. electrodeposited Zn-Al- NO_3 films onto gold-coated glass substrates with a nitrate solution containing Zn^{2+} and Al^{3+} ions [18]. An optically transparent Li-Al- CO_3 LDH was electrochemically deposited onto AZ31 substrate from a $\text{Li}^+/\text{Al}^{3+}$ aqueous solution [34]. The coating provided excellent corrosion protection to the substrate but synthesis of the electrolyte solution requires many steps. Wu et al. deposited Zn-Al- NO_3 films onto AZ91D Mg alloy substrate in a $\text{Zn}^{2+}/\text{Al}^{3+}$ aqueous solution [35]. The LDH coating showed great corrosion resistance and improved adhesion to the substrate. While a Co-Ni LDH has been deposited onto stainless steel substrates as a possible supercapacitor in a previous study, the corrosion performance has not been evaluated for any LDHs onto steels [36]. In this study, modified zaccagnaite films were electrochemically deposited on stainless steel substrates at room temperature. These films are modified zaccagnaite materials for two reasons. First, the elemental ratio of Zn:Al is outside the typical range for LDH and secondly the carbonate group has been exchanged with nitrate. A step potential method was used to synthesize the films. A short deposition duration (60s) followed by drying of the film was repeated up to five times to mitigate the fracturing of the film which commonly occurs in hydroxide and oxide films prepared from aqueous solutions. These films were characterized and tested for their corrosion resistance in 3.5 wt.% NaCl aqueous solution.

3.2. Experimental

3.2.1. Film Synthesis

The substrates were stainless steel (430) discs from Ted Pella, Inc. with a diameter of 10 mm, a thickness of 0.76 mm and an area of 1.77 cm². The substrates contained <0.12% C, 16-18% Cr, <0.75% Ni, <1.0% Mn, <1.0% Si, <0.040% P, and <0.030% S by weight. The discs were degreased by rough polishing with grit paper and then sonicated in acetone. The substrates were then attached to coiled copper wire leads with conductive silver epoxy. Once dry they were mounted in epoxy utilizing molds. After curing, the mounted electrodes were polished with SiC and diamond to a mirror finish followed by ultrasonication in ethanol.

The electrolytic solution was prepared by dissolving a 2:1 molar ratio of Zn²⁺ to Al³⁺ ions in distilled water. Aluminum nitrate nonahydrate (Al(NO₃)₃•9H₂O, Alfa Aesar) was the aluminum source, zinc nitrate hexahydrate (Zn(NO₃)₂•6H₂O, Alfa Aesar) was the source of zinc and potassium nitrate (KNO₃, Fisher Scientific) was used as the electrolyte to help facilitate the formation of modified zaccagnaite film at the electrode surface. The electrolytic concentration of each compound was 0.02 M Zn(NO₃)₂•6H₂O, 0.01 M Al(NO₃)₃•9H₂O and 0.2 M KNO₃. An EG&G Princeton Applied Research (PAR) Model 273A potentiostat/galvanostat was used to electrochemically deposit films. The depositions were performed at room temperature utilizing a three-electrode configuration under a nitrogen atmosphere. The working electrode was a stainless steel disc, a platinum mesh was used as the counter electrode and the reference electrode was a saturated calomel electrode (SCE). A step potential method was employed for thin film deposition. The applied potential started at -1.5 V for 5 sec and then stepped to -1.0 V

for 20 sec. Each layer was deposited for 60 sec and allowed to dry undisturbed between depositions.

3.2.2. Characterization

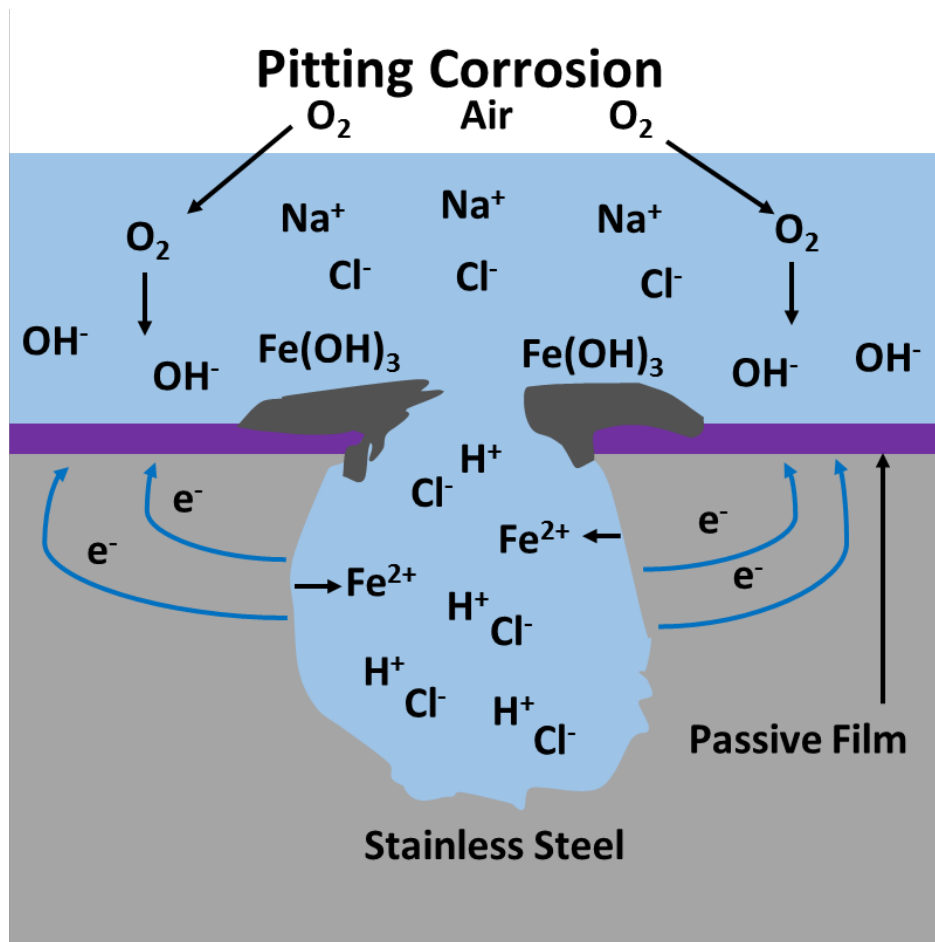
The structure and phase composition of the modified zaccagnaite films were identified by X-ray diffraction (XRD) with a Siemens D500 diffractometer using Cu K α radiation ($\lambda = 1.5405$ Å) in a standard Bragg-Brentano configuration. The X-ray tube was operated at 35 kV and 24 mA. Each sample was scanned from 2.0° to 40° (2 θ), with a step size of 0.05° and a dwell time of 1.0 seconds. The surface morphology of the films was characterized by scanning electron microscopy (SEM) with an X-ray dispersive spectroscopy (EDX) attachment (FEI Quanta 200 ESEM). A spot size of 3.0 and an accelerating voltage of 25 kV were used. Film thickness measurements were performed with a Veeco Dektak 150 stylus profilometer. A Perkin Elmer Spectrum One FT-IR Spectrophotometer was used to analyze the composition of the films. The films were scraped off with a blade and ground up further before being placed onto an ATR attachment. Each sample was scanned 16 times at a wavenumber range of 4000 – 450 cm⁻¹.

3.2.3. Immersion Tests and Corrosion Measurements

Corrosion is a phenomenon where a chemical or electrochemical reaction attacks and degrades metal species. It can usually be described as a set of redox reactions where a metal species becomes oxidized and hydrogen is reduced. Pitting corrosion is a localized form of corrosion that occurs as a result of exposure to specific environments especially those containing chlorides. It results in the production of cavities in the substrate and corrosion

products often cover these pits. Pitting can be initiated by mechanical or chemical damage to the oxide layer protecting the metal. Conditions that can cause pitting corrosion include low oxygen concentrations, high acidity, and high chloride concentrations. A common example is the pitting corrosion of stainless steel displayed in Figure 3.1.

Figure 3.1. Diagram of the pitting corrosion of stainless steel in seawater.



Initially corrosion reactions occur normally inside and outside of the pit. These reactions are:



Then the cathodic reaction inside the pit consumes all of the available O₂ leaving the pit oxygen deficient. As a result of these reactions the electrolyte enclosed in the pit gains positive electrical charge in contrast to the electrolyte surrounding the pit, which becomes negatively charged. Chloride and hydroxide ions diffuse into the pit to maintain a low potential energy. The formation of iron chloride occurs and then the iron chloride is hydrolyzed:



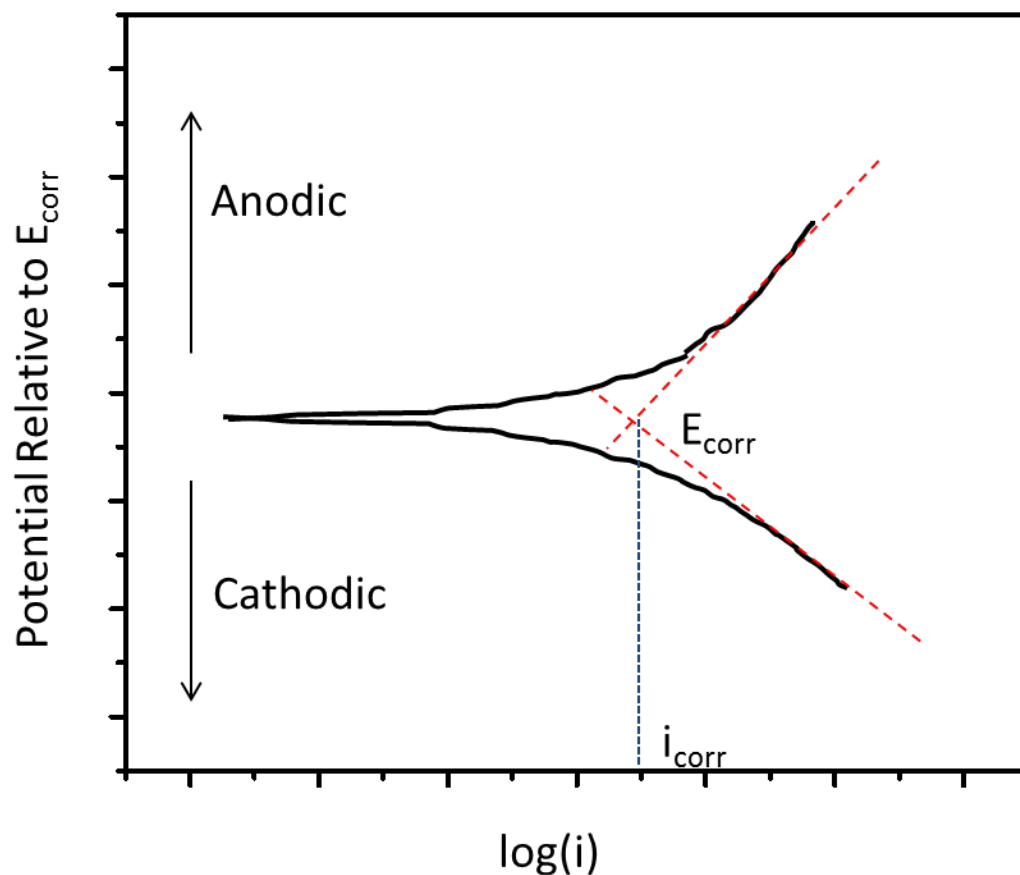
The hydrolysis of iron chloride causes the pH of the electrolyte in the pit to decrease. The decrease in pH increases the dissolution of iron and increases the rate of corrosion reactions.

Because corrosion reactions usually occur electrochemically, the effects of corrosion on metal are best monitored and measured through electrochemical techniques [37,38]. The Tafel method plots the data as potential versus log of the current. The Tafel plot, which is shown in Figure 3.2, consists of both anodic and cathodic polarization curves. Tafel analysis is performed by extrapolating the linear sections of the plot back to their intersection. The voltage and current at the intersection are known as the corrosion voltage (E_{corr}) and current (I_{corr}). The polarization resistance (R_p) can be obtained from the Stern-Geary equation:

$$I_{\text{corr}} = \frac{\beta_a \beta_c}{2.3 R_p (\beta_a + \beta_c)} \quad (\text{Equation 3.4})$$

The Tafel slopes β_a and β_c are obtained from the extrapolated lines and I_{corr} can be found at the intersection. The higher the R_p the lower the corrosion rate of the sample.

Figure 3.2. Example of Tafel plot and extrapolation.

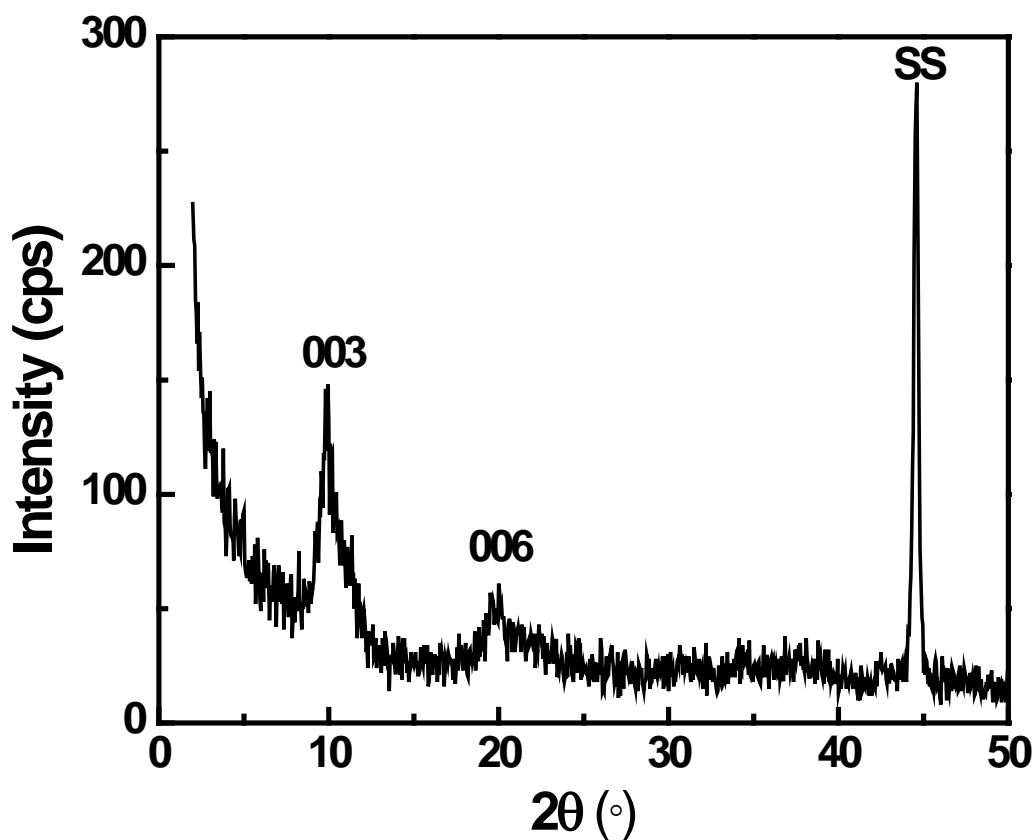


Polarization measurements and immersion tests were performed in 3.5 wt.% NaCl aqueous solutions at room temperature. Electrochemical measurements were conducted with an EG&G Princeton Applied Research (PAR) Model 4000 potentiostat/galvanostat. The coated film and a SCE electrode were used as the working and reference electrodes, respectively. Two graphite rods were used as the counter electrodes for polarization measurements. Each sample was immersed in the NaCl solution for 30 min before polarization curves were measured with respect to open circuit potential (OCP) at a scan rate of 1 mV/s. Immersion tests were performed in 3.5 wt.% NaCl solution at room temperature for up to 168 hours to examine the long term corrosion resistance of the zaccagnaite coated films.

3.3. Results and Discussion

3.3.1. Structural Characterization

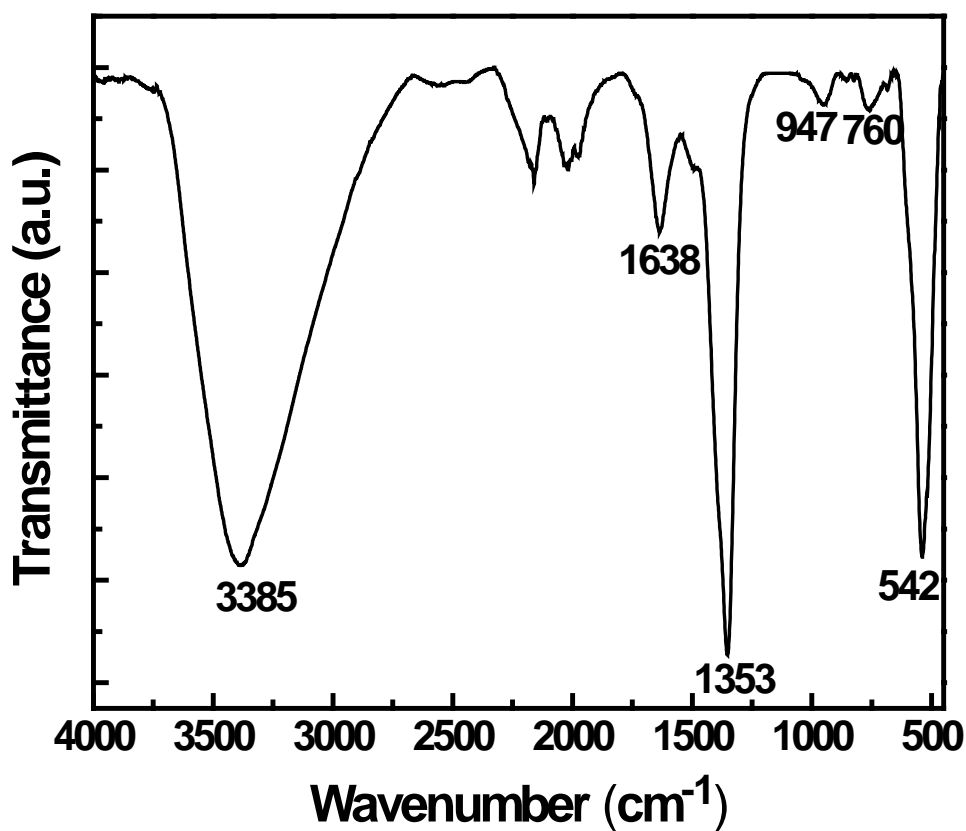
Figure 3.3. X-ray diffraction pattern of a modified zaccagnaite coating on a stainless steel substrate.



The X-ray diffraction pattern of the modified zaccagnaite film deposited on the substrate is displayed in Figure 3.3. The film was grown during one continuous deposition in order to obtain enough material for characterization. The peaks at 9.89° and 20.00° (2θ) represent the characteristic (003) and (006) reflections for LDH. The peak at 44.61° corresponds to the substrate. A basal spacing of 0.89 nm was calculated from the most intense peak at 9.89° using Bragg's equation. This value is in agreement with previous studies [18, 35,

39]. The absence of non-basal reflections is evidence that the film is composed of highly oriented platelets [20, 40]. The peaks may be of low intensity due to the thickness of the films (0.43 to 2.8 μm) and transparency of the lighter weight elements to X-rays, as well as some slight amorphous nature. Furthermore, the diffraction peaks are slightly broad due to poor crystallinity associated with most electrosynthesized LDH films [41]. Although the metal content of the electrodeposited films as measured by EDX is outside the typical accepted range (4:1 to 2:1 for the $2^+/3^+$ cation ratio) of LDH, the XRD and FTIR spectra show the presence of LDH [42].

Figure 3.4. FT-IR spectrum of a modified zaccagnaite film.



The FT-IR spectrum for the deposited film is displayed in Figure 3.4. The spectrum confirms the presence of hydroxides with only water and nitrate ions in the interlayer region.

The broad peak at 3385 cm^{-1} corresponds to O-H stretching of hydroxide and water in the interlayer region. The peak at 1638 cm^{-1} shows the bending vibration of the interlayer water region molecules. The peaks at 1353 cm^{-1} represents the asymmetric stretching of nitrate ions in the interlayer region [18]. The peaks at $947, 760$ and 542 cm^{-1} are associated with Al-O stretching modes [35, 43, 44]. The peaks from $2600\text{--}1800\text{ cm}^{-1}$ are from the diamond ATR surface [45]. The FT-IR is typical of a Zn-Al LDH intercalated with nitrate.

Figure 3.5. SEM images of modified zaccagnaite films for (a) 1L, (b) 2L, (c) 5L and (d) 5L film with a portion of top phase removed.

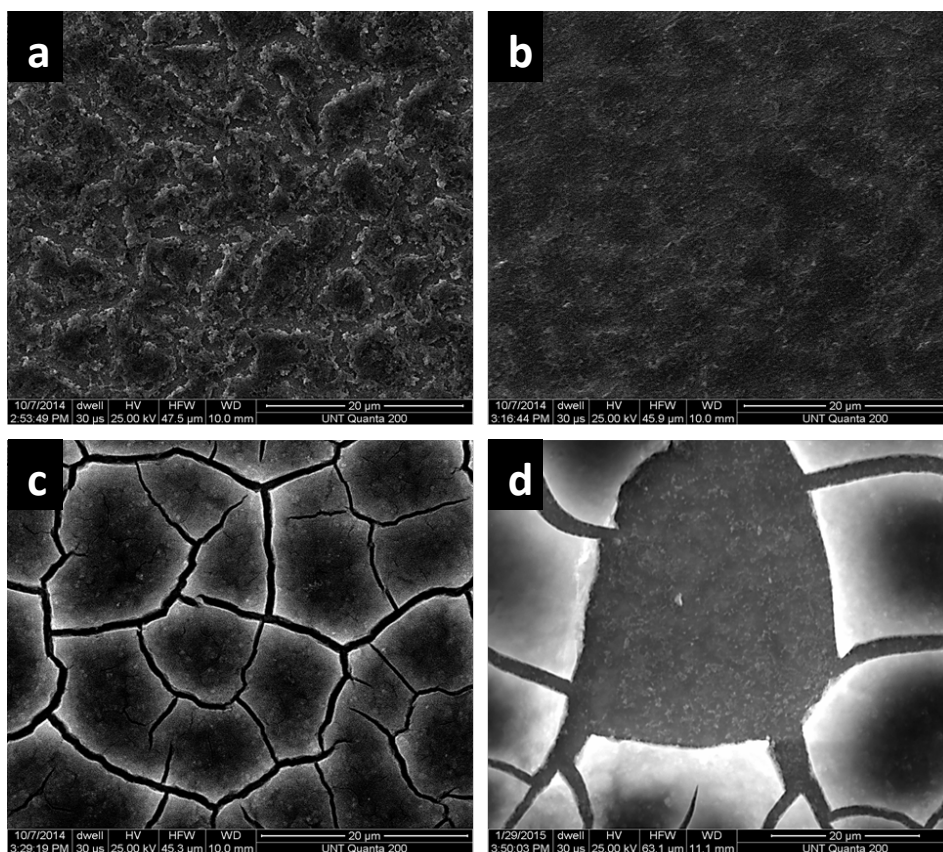


Table 3.1. Elemental composition and thickness of the electrodeposited films (n=3).

Number of Layers	Zinc Atomic %	Aluminum Atomic %	Thickness (nm)
1	41 \pm 4	59 \pm 4	431 \pm 50
2	24 \pm 2	76 \pm 2	612 \pm 46
5	14 \pm 3	86 \pm 3	2814 \pm 45

Figure 3.5 shows the surface morphology of modified zaccagnaite films from a one layer (1L), two layer (2L) and five layer (5L) depositions. The surface of the 1L film (a) shows a flattened disorganized coating with gaps caused by dehydration of the film. The elemental ratio of Zn:Al measured by EDX on the surface of the film is approximately 1:1.2. Table 3.1 list the elemental ratios and film thicknesses for the coatings. The SEM image of the 2L film (b) shows a fairly homogenous surface with none of the flaws observed in the previous image. Multiple depositions reduced the uneven coverage that accompanies dehydration of the film. The elemental ratio of Zn:Al on the surface of the 2L film is approximately 1:2.8. The 5L film (c) exhibits a surface which is different from both the 1L and 2L films. The elemental ratio of the 5L film's surface is approximately 1:5. While it does not have gaps in material as seen in the 1L film there are cracks observed. In Figure 3.5d it is apparent that these cracks do not penetrate all the way to the substrate. Two separate phases can be observed, a fractured phase upon a continuous underlying phase. The surface of the underlying phase in Figure 3.5d has slightly more zinc (1:4 Zn:Al ratio) than the 5L film. Previous research has shown that LDH with an acceptable divalent:trivalent cation ratio is only formed during a certain time frame, dependent on the deposition potential, formation pH of the divalent cation hydroxide and divalent:trivalent cation ratio. At longer synthesis times an aluminum dominated hydroxide

phase is formed [42]. The SEM and EDX results also support this conclusion. Figure 3.6 shows a schematic explaining the changing deposition mechanism where initially hydroxides are generated at the electrode surface. When the pH increases sufficiently at the electrode, metal hydroxides began to precipitate and any hydroxides not consumed move into the bulk of the solution. The diffusion of hydroxides away from the electrode increases the pH of the solution resulting in the precipitation of aluminum hydroxide. Aluminum hydroxide forms at approximately pH 4 and zinc aluminum LDH precipitates at approximately pH 6 [35, 42]. The aluminum hydroxide precipitate coats the mixed hydroxide phase. This deposition process results in the film structure depicted in Figure 3.7, which is comprised of a mostly aluminum hydroxide phase on top of a mixed hydroxide phase. The zinc content of the mixed hydroxide phase increases as the distance to the substrate decreases.

Film thickness measurements for 1L, 2L and 5L films are reported in Table 3.1. The film thickness does not increase proportionally with the number of deposition layers. The lack of linearity may be due to deposition in defects caused by dehydration of previous layers. Furthermore, the rate of film growth may change due to the differences in growth on the substrate versus growth on previously deposited film. The conductivity of the substrate is higher than the conductivity of the deposited film, thus the kinetics will change. The formation of two sequential phases may cause irregular film growth rate. The conductivity variation in each layer and the non-conducting nature of the zinc and aluminum hydroxide film may also contribute to the nonlinear growth rate.

Figure 3.6. Film formation process of the mixed hydroxide phase and top aluminum hydroxide layer for the electrodeposited zaccagnaite coating.

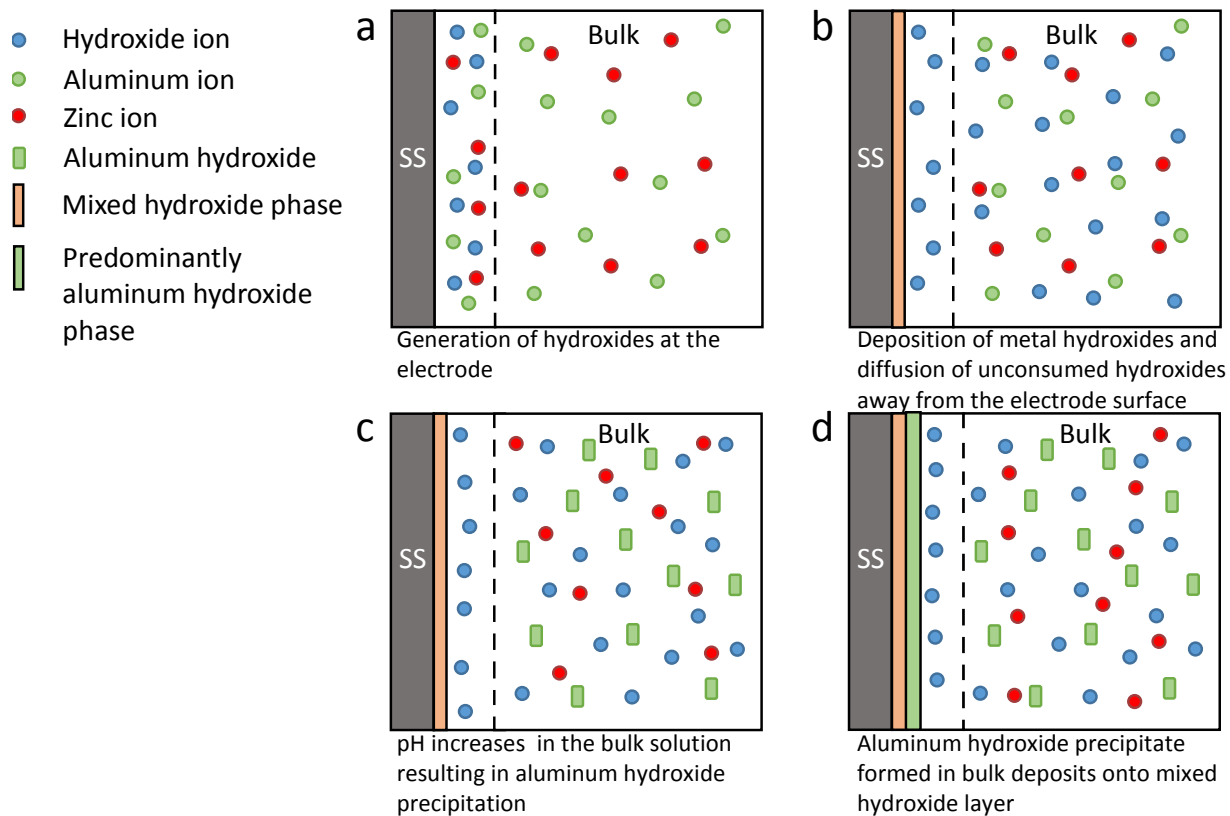
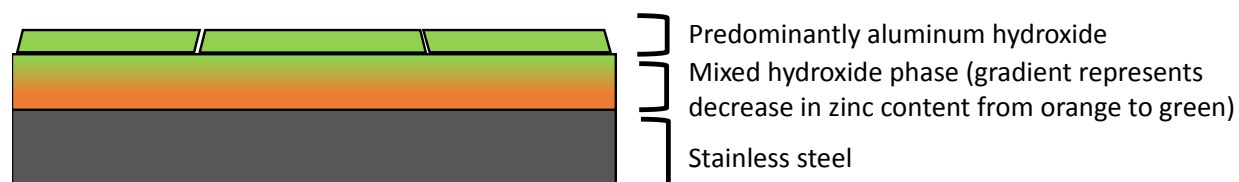


Figure 3.7. Film composition from substrate to outer layer for the electrodeposited zaccagnaite coating.



3.3.2. Corrosion Resistance

Figure 3.8. Polarization curves of the substrate and modified zaccagnaitite films measured in 3.5 wt.% NaCl solution.

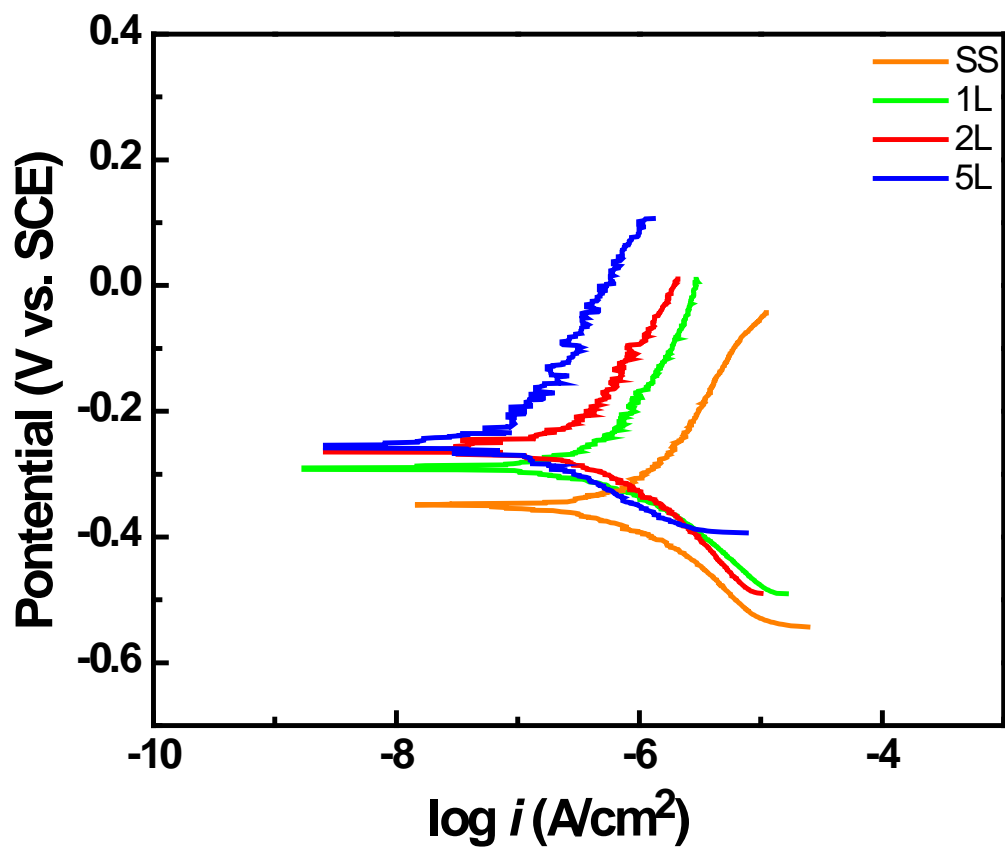


Table 3.2. Corrosion potentials and corrosion current densities derived from polarization experiments performed in 3.5 wt.% NaCl (n=3).

Sample	E_{corr} (V vs. SCE)	i_{corr} (A/cm ²)	R_p (M Ω /cm ²)
SS	-0.363 ± 0.027	$1.11 \times 10^{-6} \pm 0.01 \times 10^{-6}$	0.19 ± 0.06

1L	-0.269 ± 0.020	$4.49 \times 10^{-7} \pm 1.94 \times 10^{-7}$	0.57 ± 0.27
2L	-0.240 ± 0.008	$2.16 \times 10^{-7} \pm 1.15 \times 10^{-7}$	0.79 ± 0.06
5L	-0.237 ± 0.013	$8.41 \times 10^{-8} \pm 1.49 \times 10^{-8}$	2.30 ± 0.05

The polarization curves of the bare substrate, 1L, 2L and 5L films in 3.5 wt.% NaCl solution are shown in Figure 3.8. The corrosion potential (E_{corr}), corrosion current density (i_{corr}) and polarization resistance (R_p) for each sample are listed in Table 3.2. The deposition of modified zaccagnaites resulted in a positive shift in the E_{corr} and a decrease in the i_{corr} . The 1L film had the greatest effect on E_{corr} , shifting almost 100 mV in the positive direction while the 2L and 5L films E_{corr} shifted by smaller increments of approximately 30 and 13 mV, respectively. The i_{corr} decreased from 1.11×10^{-6} A to 4.49×10^{-7} A, 2.16×10^{-7} A, and 8.41×10^{-8} A for the 1L, 2L, and 5L films, respectively. The R_p increased with the number of deposited layers resulting in the 5L film having an R_p an order of magnitude larger than the substrate R_p . These polarization measurements indicate that the film provides a barrier to the transport of aqueous species to the substrate so that the ability of the chloride ions to attack the substrate is reduced. This barrier increases and defects are minimized as more layers are deposited. Some current density oscillation is observed in the anodic branch of the polarization curves which was also observed in a previous study [28]. The current density oscillation becomes greater as the number of deposited layers increases. This may be due to the dissolution of hydroxides from the coating surface or even some interlayer exchange of species in the solution.

The stability of the modified zaccagnaites film in a corrosive marine environment was simulated with immersion testing. A 5L film was immersed at increasing durations up to 168h in 3.5 wt.% NaCl solution. Figure 3.9 shows the polarization curves of the film at four different

immersion times. Table 3.3 lists the E_{corr} , i_{corr} and R_p as the average of 3 measurements for the 5L film. The E_{corr} remained relatively unchanged at approximately -0.240 V from 1 to 72h. At 168h the E_{corr} shifted positively to -0.178 V. The i_{corr} was also stable starting at 9.35×10^{-8} A for 1h and ending at 7.05×10^{-8} A at 168h. The R_p maintained a value between 2-3 M Ω over the entire immersion period from 1h to 168 h. Only the film immersed for 168h exhibits film breakdown at the end of the anodic region suggesting that the film is susceptible to long term damage caused by the chloride environment. Current density oscillation is visible again beginning around the corrosion potential and throughout the anodic region.

SEM images were taken of the 5L film before and after immersion in 3.5 wt.% NaCl solution up to 168h. Figure 3.10 shows that the aluminum dominated layer on the surface of the film forms pits after immersion. These defects range in size from submicron to a couple of microns. These flaws may be evidence of dissociation of the film into hydroxide ions. These defects only affect the top phase and do not appear to penetrate to the substrate because of the stability observed during immersion testing. The top phase acts as a sacrificial barrier for the underlying coating and possibly releases hydroxide ions.

Figure 3.9. Polarization curves of 5L films immersed in 3.5 wt.% NaCl solution up to 168h.

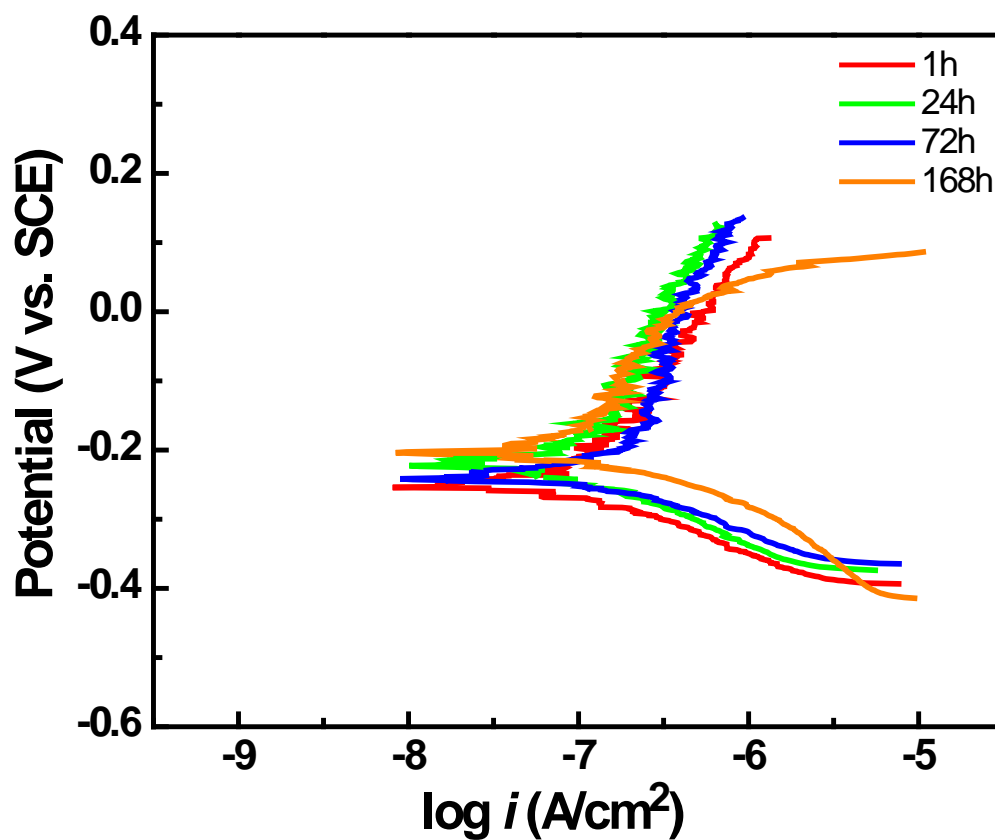
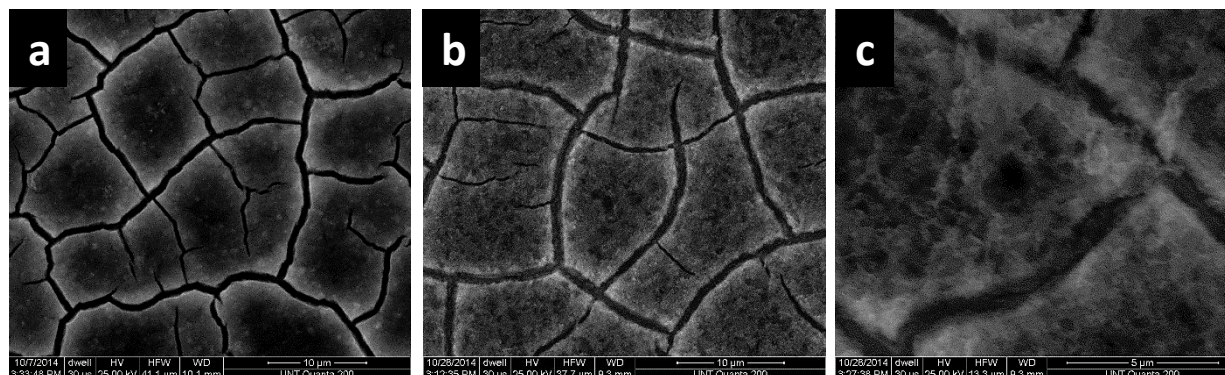


Table 3.3. Corrosion potentials and corrosion current densities derived from immersion of a 5L film in 3.5 wt.% NaCl for various immersion times (n=3).

Immersion Time	E_{corr} (V vs. SCE)	I_{corr} (A/cm ²)	R_p (M Ω /cm ²)
1h	-0.239 ± 0.017	$9.35 \times 10^{-8} \pm 2.00 \times 10^{-8}$	2.19 ± 0.59
24h	-0.245 ± 0.031	$7.88 \times 10^{-8} \pm 1.52 \times 10^{-8}$	2.32 ± 0.37
72h	-0.235 ± 0.020	$6.72 \times 10^{-8} \pm 2.75 \times 10^{-8}$	3.09 ± 1.38
168h	-0.178 ± 0.013	$7.05 \times 10^{-8} \pm 1.69 \times 10^{-8}$	2.33 ± 0.72

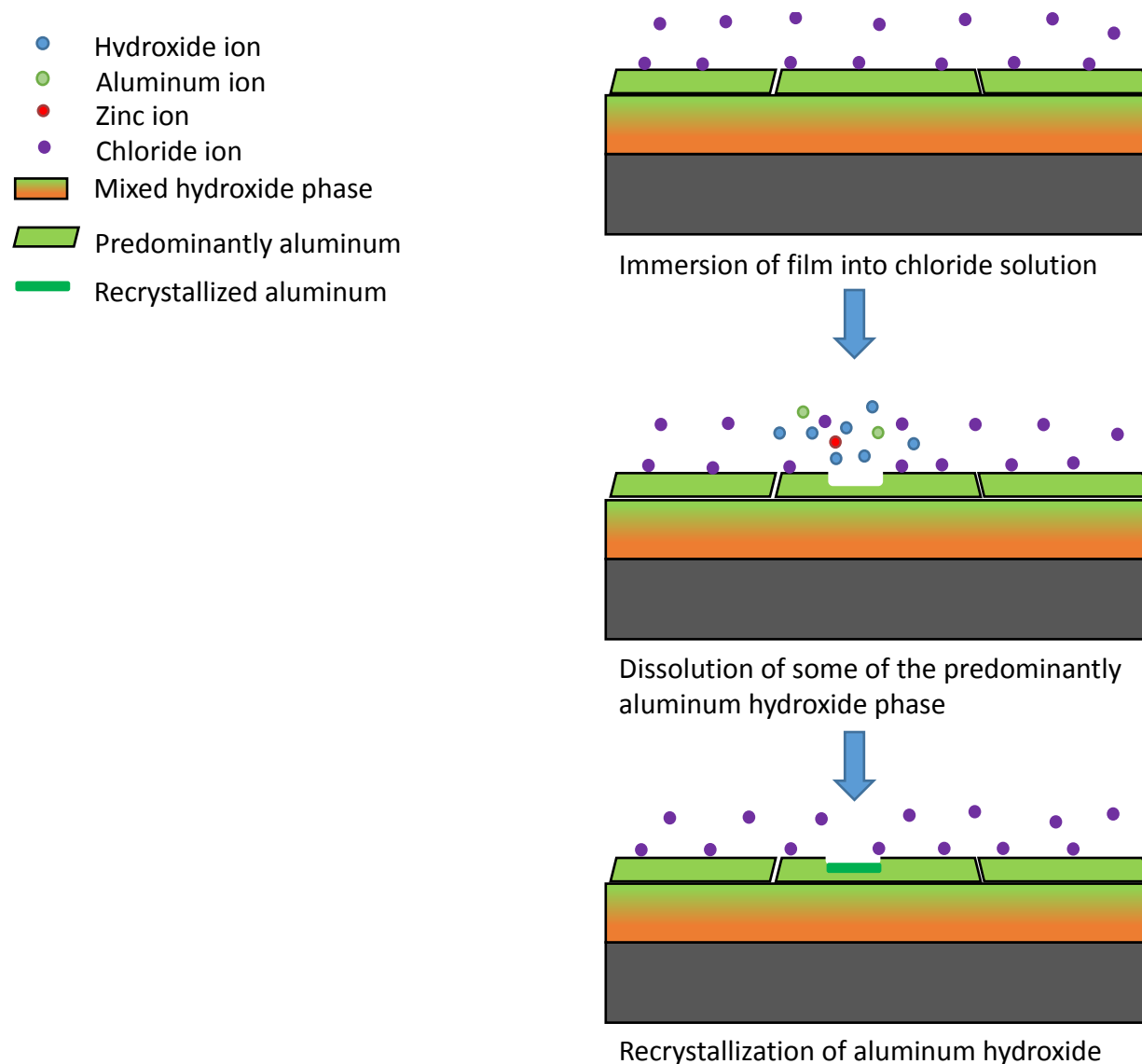
Figure 3.10. SEM images of 5L film (a) before and (b) after immersion in 3.5 wt. % NaCl solution for 168h as well as (c) an enlarged image of a defect in the immersed film.



The anticorrosion performance of the film could be the result of a multitude of factors. The main attribute that confers its corrosion resistance is the ability to form a dense and thick film which prevents the penetration of ions to the substrate surface. The film is insulating, resulting in a decrease in the rate of any electrochemical reactions including those involving corrosion. Furthermore, the nitrate ions in the film have a lower affinity for intercalation than chloride ions. Surface anion exchange with chloride ions traps them and slows their rate of migration to the substrate. This anion exchange phenomenon has been observed in previous studies [34, 35, 46]. Deterioration of the film may release hydroxide ions into the local environment increasing the pH [34]. The release of hydroxide ions can slow down the occurrence of pitting corrosion by reducing the rate of chloride migration to the pit and neutralizing the local solution environment. Previous research has also shown that layered double hydroxides can undergo dissolution/recrystallization or self-healing reactions during the corrosion process [29]. Hydrotalcite has been shown to form a protective amorphous aluminum hydroxide layer to prevent dissolution in mildly acidic solutions [47]. The mostly

aluminum hydroxide top phase behaves as protective coating for the mixed hydroxide phase preventing its dissolution. Figure 3.11 depicts the immersion of the film in corrosive media, the sacrificial protection of the aluminum dominate phase and possible crystallization of aluminum hydroxide in a defect. Further study is required to determine the comprehensive mechanism of corrosion resistance of electrodeposited modified zaccagnaite.

Figure 3.11. Postulated corrosion mechanism for immersed electrodeposited zaccagnaite film.



3.4. Chapter Conclusions

In this study a facile method was developed to electrochemically deposit modified zaccagnaite films onto a stainless steel substrate. The electrodeposition occurred in multiple layers in order to minimize defects generated during deposition and drying of the film. XRD and FT-IR studies showed the presence of a LDH phase; however, the elemental ratios of Zn:Al were outside the typical limits for LDH. The metal substrate coated with modified zaccagnaite exhibited higher corrosion resistance than the bare substrate in 3.5 wt.% NaCl solution. Corrosion protection increased with the number of layers deposited. Aluminum concentration in the coating also increased with the number of layers. The 5L film's corrosion voltage shifted positively 0.126 V and the corrosion current was reduced by 92% when compared to the bare substrate in 3.5 wt.% NaCl. The 5L film also maintained its corrosion resistance while immersed for 168h in 3.5 wt.% NaCl demonstrating that electrochemically generated modified zaccagnaite is an effective material to reduce stainless steel corrosion.

3.5. References

- [1] N. R. Baddoo, *J. of Constructional Steel Res.*, 2008, 64, 1199-1206.
- [2] A. Latifi, M. Imani, M. T. Khorasani, M. D. Joupari, *Surf. Coatings Technol.*, 2013, 221, 1-12.
- [3] T. J. Mesquita, E. Chauveau, M. Mantel, N. Bouvier, D. Koschel, *Corros. Sci.*, 2014, 81, 152-161.
- [4] G. Herting, I. O. Wallinder, C. Leygraf, *J. of Food Engineer.*, 2008, 87, 291-300.
- [5] C. Bitondo, A. Bossio, T. Monetta, M. Curioni, F. Bellucci, *Corros. Sci.*, 2014, 87, 6-10.
- [6] T. K. Ha, H. T. Jeong, H. J. Sung, *J. Mater. Processing Technol.*, 2008, 187-188, 555-558.

- [7] M. A. Akl, M. A. Ahmed, A. Ramadan, *J. of Pharmaceutical and Biomedical Analy.*, 2011, 55, 247-252.
- [8] M. A. Streicher, J. F. Grubb, (2011) Austenitic and Ferritic Stainless Steels, in Uhlig's Corrosion Handbook, Third Edition (ed R. W. Revie), John Wiley & Sons, Inc., Hoboken, NJ, USA. 657-693.
- [9] Q. Hu, G. Zhang, Y. Qiu, X. Guo, *Corros. Sci.*, 2011, 53, 4065–4072.
- [10] Y. Yin, L. Niu, M. Lua, W. Guo, S. Chen, *Appl. Surf. Sci.*, 2009, 255, 9193–9199.
- [11] A.-M. Lazar, W. P. Yespica, S. Marcelin, N. Pébère, D. Samélor, C. Tendero, C. Vahlas, *Corros. Sci.*, 2014, 81, 125-131.
- [12] M. B. González, S. B. Saidman, *Prog. in Org. Coat.*, 2015, 78, 21-27.
- [13] T. Stimpfling, F. Leroux, H. Hintze-Bruening, *Colloids and Surf. A: Physicochemical and Engineer. Asp.*, 2014, 458, 147-154.
- [14] M.L. Zheludkevich, S.K. Poznyak, L.M. Rodrigues, D. Raps, T. Hack, L.F. Dick, T. Nunes, M.G.S. Ferreira, *Corros. Sci.*, 2010, 52, 602–611.
- [15] J. Tedim, M.L. Zheludkevich, A.C. Bastos, A.N. Salak, A.D. Lisenkov, M.G.S. Ferreira, *Electrochim. Acta*, 2014, 117, 164-171.
- [16] D.G. Evans, R.C.T. Slade, *Struct. Bond.*, 2006, 119, 1–87.
- [17] A. N. Salak, A. D. Lisenkov, M. L. Zheludkevich, M. G. S. Ferreira, *ECS Electrochemistry Lett.*, 2014, 3, C9-C11.
- [18] M.S. Yarger, E.M.P. Steinmiller, K.S. Choi, *Inorganic Chem.*, 2008, 47, 5859–5865.
- [19] S. J. Mills, A. G. Christy, J. -M. R. Génin, T. Kameda, F. Colombo, *Mineralogical Mag.*, 2012, 76, 1289-1336.

- [20] F.Z. Zhang, M. Sun, S.L. Xu, L.L. Zhao, B.W. Zhang, *Chemical Engineering J.*, 2008, 141, 362–367.
- [21] X.X. Guo, S.L. Xu, L.L. Zhao, W. Lu, F.Z. Zhang, D.G. Evans, X. Duan, *Langmuir*, 2009, 25, 9894–9897.
- [22] J.K. Lin, J.Y. Uan, *Corros. Sci.*, 2009, 51, 1181–1188.
- [23] J. Chen, Y.W. Song, D.Y. Shan, E.H. Han, *Corros. Sci.*, 2011, 53, 3281–3288.
- [24] J. Chen, Y.W. Song, D.Y. Shan, E.H. Han, *Corros. Sci.*, 2012, 63, 148–158.
- [25] J. Chen, Y.W. Song, D.Y. Shan, E.H. Han, *Corros. Sci.*, 2012, 65, 268–277.
- [26] J. Chen, Y.W. Song, D.Y. Shan, E.H. Han, *Corros. Sci.*, 2013, 74, 130–138.
- [27] F. Zhang, Z. Liua, R. Zeng, S. Li, H. Cui, L. Song, E. Hanc, *Surf. & Coat. Technol.*, 2014, 258, 1152–1158.
- [28] T. Ishizaki, S. Chiba, K. Watanabe, H. Suzuki, *J. of Mater. Chem. A.*, 2013, 1, 8968–8977.
- [29] T. Yan, S. Xu, Q. Peng, L. Zhao, X. Zhao, X. Lei, F. Zhang, *J. Electrochem. Soc.*, 2013, 160, C480–C486.
- [30] M. Kahl, T.D. Golden, *Electroanalysis*, 2014, 26, 1664–1670.
- [31] H.A. Conrad, J.R. Corbett, T.D. Golden, *J. Electrochem. Soc.*, 2012, 159, C29–C32.
- [32] V. DeLeon, T.D. Golden, *ECS Trans.*, 2011, 33, 43–50.
- [33] C.F. Li, M.J. Wang, W.H. Ho, H.N. Li, S.K. Yen, *J. Electrochem. Soc.*, 2011, 158, C11–C16.
- [34] J. Syu, J. Uan, M. Lin, Z. Lin, *Corros. Sci.*, 2013, 68, 238–248.
- [35] F. Wu, J. Liang, Z. Peng, B. Liu, *Appl. Surf. Sci.*, 2014, 313, 834–840.
- [36] V. Gupta, S. Gupta, N. Miura, *J. of Power Sourc.*, 2008, 175, 680–685.
- [37] M. Stern, *J. Electrochem. Soc.*, 1955, 102, 609–616.

- [38] M. Stern, L. Geary, *J. Electrochem. Soc.*, 1957, 104, 56-63.
- [39] A. de Roy, C. Forano, J.P. Besse, Layered double hydroxides: synthesis and post-synthesis modification, in: V. Rives (Ed.), *Layered Double Hydroxides: Present and Future*, Nova Science Publishers, Inc., New York, 2001, pp. 1-39.
- [40] X. Lei, L. Wang, X. Zhao, Z. Chang, M. Jiang, D. Yan, X. Sun, *Industrial & Engineering Chem. Res.*, 2013, 52, 17934–17940.
- [41] I. Gualandi, M. Monti, E. Scavetta, D. Tonelli, V. Prevot, C. Mousty, *Electrochim. Acta*, 2015, 152, 75-83.
- [42] M. Monti, P. Benito, F. Basile, G. Fornasari, M. Gazzano, E. Scavetta, D. Tonelli, A. Vaccari, *Electrochim. Acta*, 2013, 108, 596-604.
- [43] J. T. Klopprogge, R. L. Frost, L. Hickey, *J. Raman Spectr.*, 2004, 35, 967–974.
- [44] Y. Lin, J. Wang, D. G. Evans, D. Li, *J. Phys. Chem. Solid.*, 2006, 67, 998-1001.
- [45] G. Hu, N. Wang, D. O'Hare, J. Davis, *J. Mater. Chem.*, 2007, 17, 2257-2266.
- [46] J. Tedim, A. Kuznetsova, A.N. Salak, F. Montemor, D. Snihirova, M. Pilz, M.L. Zheludkevich, M.G.S. Ferreira, *Corros. Sci.*, 2012, 55, 1–4.
- [47] M. Jobbágy, A. E. Regazzoni, *Appl. Clay Sci.*, 2011, 51, 366-369.

CHAPTER 4

INVESTIGATION OF THE OPTIMAL PARAMETERS FOR THE PREPARATION OF SUPERHYDROPHOBIC MODIFIED ZACCAGNAITE FILMS ON STAINLESS STEEL

4.1. Introduction

Superhydrophobic (SHP) surfaces that have static water contact angles (SWCA) greater than 150° have been investigated recently in literature because of their potential for application in self-cleaning surfaces, corrosion resistant coatings, water transport, oil collection, and tribology [1-5]. SHP surfaces exist in nature on the lotus leaf, legs of a water strider, and the wings of insects [6-10]. SHP surfaces cannot exist on a flat surface. The highest SWCA on a flat surface is 120° which is produced by modifying the surface with trifluoromethyl groups [11]. The combination of high surface roughness (micro and nanoscale) and low surface energy materials result in SHP surfaces. SHP surfaces are usually produced by two approaches. The first method is to produce a high energy surface with high surface roughness and then modify the surface with a low surface energy material. Various techniques have been utilized to create rough surfaces including electrochemical deposition, anodization, sol-gel process, chemical etching, chemical vapor deposition, plasma treatment, casting, sandblasting, electrospinning, and layer-by-layer deposition [13-21]. Common low surface energy materials used to modify rough surfaces are long chain fatty acids, thiols, and fluorosilanes. The second method involves taking a hydrophobic material and creating high surface roughness [22,23]. Most research involves performing the first procedure.

Stainless steel (SS) is an alloy containing iron with a minimum of 10.5% chromium. Its high mechanical strength and corrosion resistance results in its use in the petrochemical,

aviation, food storage and processing, water treatment and transport, automotive, medical, and pharmaceutical industries [24-30]. Industries with metal-fluid contact would benefit most from SHP surfaces. The food industry frequently uses SS containers to store and mix liquids. SHP SS would reduce the need for cleaning and reduce the corrosion of these containers, thus decreasing maintenance costs and equipment failure. SHP surfaces can reduce fluid drag in pipe flow [31]. Rough surfaces on SS have been produced by acid treatment, electroless plating, sputtering, electrochemical etching, laser irradiation, sol-gel, and sandblasting [32-38]. The SS surface is then modified with low surface energy materials.

Layered double hydroxides (LDH) films have been used to create surface roughness on metal substrates. LDHs are layered anionic clays derived from the natural mineral hydrotalcite. Zaccagnaite is a Zn substituted variant of hydrotalcite represented by a formula of $\text{Zn}_4\text{Al}_2(\text{OH})_{12}[\text{CO}_3] \cdot 3\text{H}_2\text{O}$. The structure contains metal hydroxide sheets with anions and water in the interlayer regions between the metal sheets. The positive charge results from the substitution of divalent ions with trivalent ions in metal hydroxide sheets and the positive charge is balanced by interlayer anions which can be exchanged. In situ hydrothermal crystallization of LDH films using porous alumina/aluminum as both the substrate and the source of trivalent cations is commonly used to induce surface roughness [39]. Hydrothermal synthesis allows for greater control over the morphology and structure of the films because of tunable nano/microstructure and crystal orientation. The rough surface of the LDH is then modified by immersion of the film in a solution containing a dissolved low surface energy material such as long chain fatty acids or fluorosilanes. SHP LDH films have also been synthesized on cotton fabric substrates by layer-by-layer deposition followed by modification

with fluoroalkylsilane [40]. Electrodeposition of LDH results in randomly oriented and poorly crystalline films [41]. If the deposition potential is increased, a mixed hydroxide phase containing a higher percentage of aluminum is obtained because of the precipitation of aluminum hydroxide in the solution bulk [42]. This aluminum dominating hydroxide phase has a much higher surface roughness.

In this study, modified zaccagnaite (Zn-Al-NO₃ LDH) films containing a greater trivalent cation content outside the acceptable limits of LDH were electrochemically synthesized on SS 430 substrates. The resulting films were immersed in an ethanol solution containing palmitic acid in order to produce a SHP surface. The influences of deposition potential, deposition time, palmitic acid concentration, hydrophobization reaction duration, and hydrophobization reaction temperature were observed to develop an optimized procedure to produce SHP modified zaccagnaite/palmitate films. SWCA was measured to assess the wettability of the films. Surface morphology and microstructure were investigated by X-ray diffraction (XRD), Fourier transform infrared spectroscopy (FTIR), scanning electron morphology (SEM), energy dispersive X-ray spectroscopy (EDS), and profilometry.

4.2. Experimental

4.2.1. Electrodeposition of Modified Zaccagnaite Film

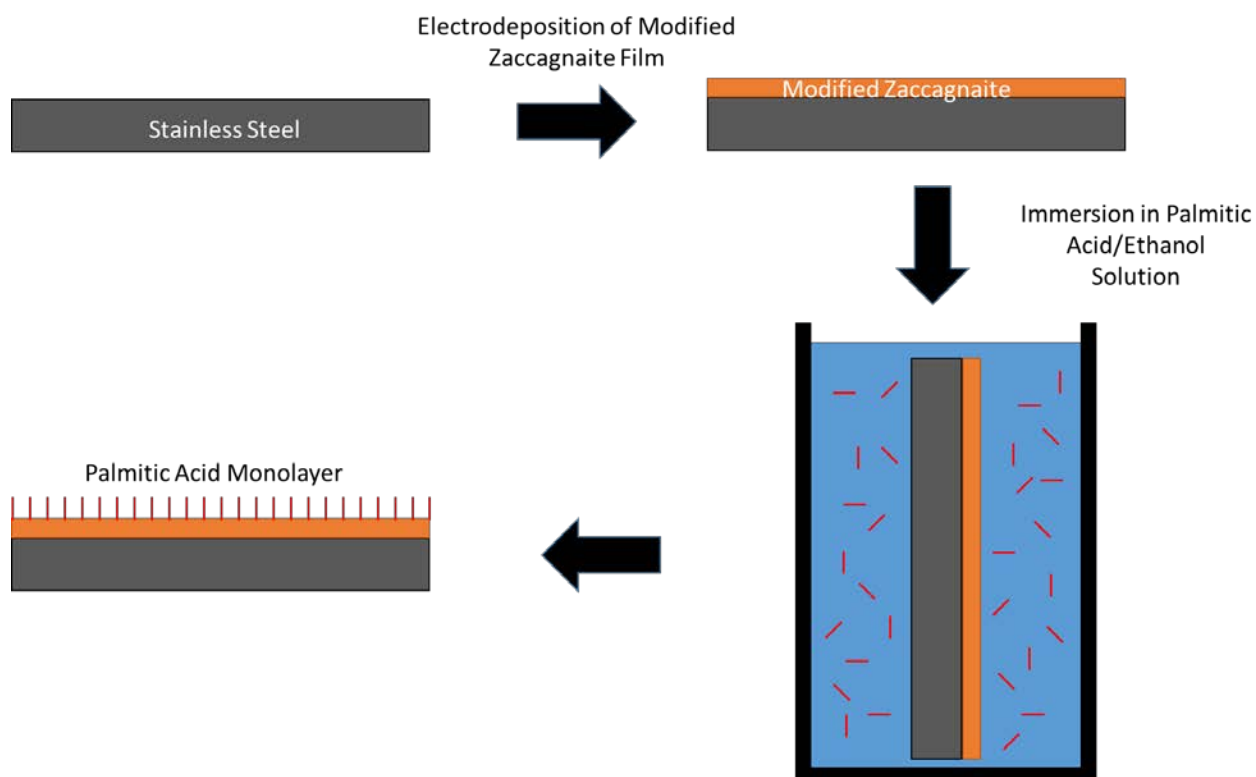
The substrates were SS 430 discs from Ted Pella, Inc. with a diameter of 10 mm, a thickness of 0.76 mm and an area of 0.95 cm². The substrates contained <0.12% C, 16-18% Cr, <0.75% Ni, <1.0% Mn, <1.0% Si, <0.040% P, and <0.030% S by weight. The discs were degreased by rough polishing with grit paper and then sonicated in acetone. The substrates were then

attached to coiled copper wire leads with conductive silver epoxy. Once dry they were mounted in epoxy utilizing molds. After curing, the mounted electrodes were polished with SiC and diamond to a mirror finish followed by ultrasonication in ethanol.

The electrolytic solution was prepared by dissolving a 2:1 molar ratio of Zn^{2+} to Al^{3+} ions in distilled water. Aluminum nitrate nonahydrate ($\text{Al}(\text{NO}_3)_3 \cdot 9\text{H}_2\text{O}$, Alfa Aesar) was the aluminum source, zinc nitrate hexahydrate ($\text{Zn}(\text{NO}_3)_2 \cdot 6\text{H}_2\text{O}$, Alfa Aesar) was the source of zinc and potassium nitrate (KNO_3 , Fisher Scientific) was used as the electrolyte to help facilitate the formation of modified zaccagnaite film at the electrode surface. The electrolytic concentration of each compound was determined to be 0.02 M $\text{Zn}(\text{NO}_3)_2 \cdot 6\text{H}_2\text{O}$, 0.01 M $\text{Al}(\text{NO}_3)_3 \cdot 9\text{H}_2\text{O}$ and 0.2 M KNO_3 . An EG&G Princeton Applied Research (PAR) Model 273A potentiostat/galvanostat was used to electrochemically deposit films. The depositions were performed at room temperature utilizing a three-electrode configuration under a nitrogen atmosphere. The working electrode was a SS disc, a platinum mesh was used as the counter electrode, and the reference electrode was a saturated calomel electrode (SCE). Films were deposited at -1.3 V and stirring was used to mitigate hydrogen evolution. The films were rinsed with distilled water and air dried at room temperature.

4.2.2. Hydrophobization Reaction

Figure 4.1. Illustration of the in situ electrosynthesis of modified zaccagnaite and hydrophobization reaction to produce a superhydrophobic surface.



The hydrophobization reaction, illustrated in Figure 4.1, was performed by immersion of the modified zaccagnaite film in ethanol solution containing dissolved palmitic acid ($\text{CH}_3(\text{CH}_2)_{14}\text{COOH}$). The films were then rinsed with ethanol and allowed to air dry. Reactant concentration, reaction time, and reaction temperature were systematically optimized. Films with the optimized electrodeposition time underwent the hydrophobization reaction at concentrations of 0.05, 0.1, and 0.2 M palmitic acid. The surface with the highest SWCA determines the optimized concentration. Then films underwent the hydrophobization reaction

for durations of 5, 7, and 9 h. Once the best reaction time was determined, the films were reacted at 20°, 40°, and 70° C to determine the optimum reaction temperature.

4.2.3. Characterization

4.2.3.1. Surface Wettability and Contact Angle

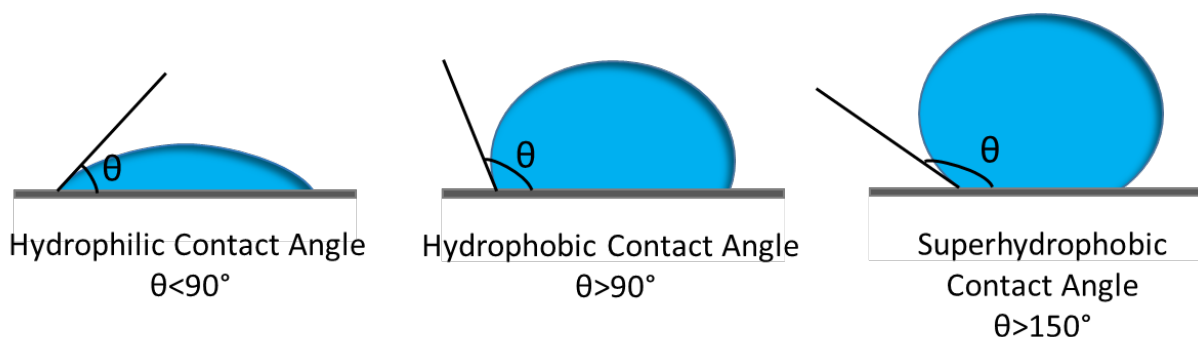
Table 4.1. Properties of hydrophilic and hydrophobic surfaces.

Hydrophilic Surface	Properties	Hydrophobic Surface
Small (<90°)	Contact Angle	Large (>90°)
High	Wettability	Low
High	Solid Surface Free Energy	Low
Usually High	Droplet Adhesion	Usually Poor

Wetting or wettability is an important material characteristic with applications in lubrication, spray quenching, liquid coatings, printing, and oil recovery [43-48]. Wettability is usually investigated by contact angle measurements which characterize the interaction between the liquid and solid phases. Wettability or wetting is the study of how a deposited liquid spreads out on a surface. Small contact angles (<90°) indicate high wettability and large contact angles (>90°) indicate low wettability. High wettability results in the liquid spreading out more because cohesive forces between the liquid molecules are less than the adhesive forces between the liquid and the surface. High wettability usually occurs on high-energy surfaces in which molecules are held together by strong chemical bonds such as metallic, ionic

or covalent. Low wettability results in cohesive forces being stronger than the adhesive forces between the surface and liquid molecules. Low wettability occurs on low-energy surfaces or molecules that are held together by weak interactions such as van der Waals or hydrogen bonding. A surface with high wettability results in droplets with a puddle appearance and a surface with low wettability will bead forming a compact droplet. Properties of both types are shown in Table 4.1. Contact angles can be classified into 3 groups as shown in Figure 4.2. Hydrophilic materials have contact angles less than 90° , hydrophobic materials have contact angles greater than 90° , and SHP materials have contact angles greater than 150° .

Figure 4.2. Contact angle classification.



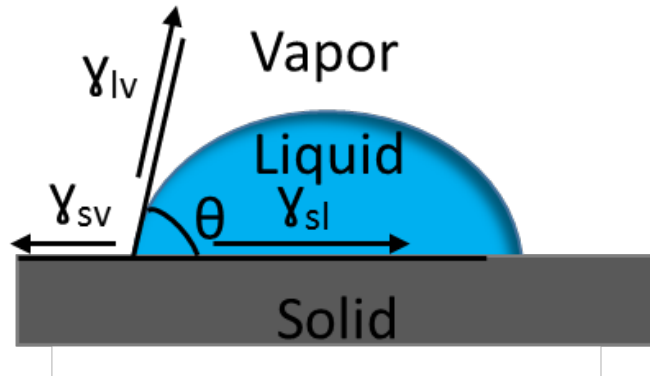
The ideal surface is a perfectly flat and homogenous surface. The contact angle is formed by the intersection of the liquid-solid and liquid-vapor interfaces. A tangent line can be drawn from the intersection to the liquid-vapor boundary of the droplet. The droplet shape is determined by the surface tension of the liquid. In the bulk of a pure liquid each molecule is acted on by cohesive forces of neighboring molecules except for the edge of the droplet where the molecules are pulled inward by neighboring liquid molecules. These forces result in internal pressure or surface tension causing the droplet to contract to minimize surface area.

and maintain the lowest free energy surface. Surface tension and gravity result in the altering of the droplet from its ideal spherical shape. The contact angle of a droplet on an ideal surface can be determined from the thermodynamic equilibrium between three interfacial energies conveyed by Young's equation [49]:

$$\gamma_{lv}\cos\theta_Y = \gamma_{sv} + \gamma_{sl} \quad (\text{Equation 4.1})$$

where γ_{lv} is the liquid-vapor interfacial energy, γ_{sv} is the surface-vapor interfacial energy, γ_{sl} is the surface-liquid interfacial energy, and θ_Y is Young's contact angle. The contact angle on an ideal surface according to Young is represented in Figure 4.3. On an ideal surface Young's contact angle is the same as the measured contact angle because there are no variations and the surface is perfectly flat.

Figure 4.3. Representations of a droplet on an ideal surface.



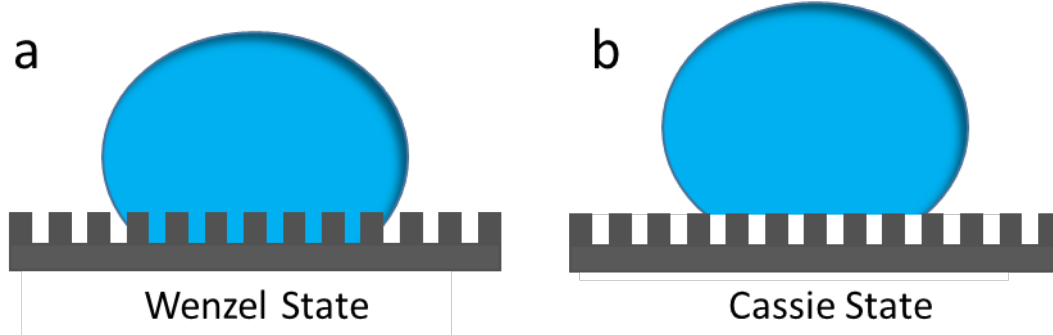
Most surfaces are from ideal and deviations from a perfectly flat surface must be considered. Surface roughness enhances the wettability characteristic of the surface chemistry [50]. The effective surface area increases with roughness, and water will spread more on a surface with hydrophilic functional groups to increase solid-liquid contact. Likewise, water on a

rough hydrophobic surface will spread less to minimize contact. Surface roughness is taken into account for Wenzel's equation:

$$\cos\theta_m = r\cos\theta_Y \quad (\text{Equation 4.2})$$

where θ_m is the measured contact angle, θ_Y is Young's contact angle, and r is the roughness ratio. The roughness ratio can be determined from the ratio of the actual and projected solid surface area where $r = 1$ for a smooth surface and $r > 1$ for a rough surface. A representation of the Wenzel state can be seen in Figure 4.4a. This model assumes that the liquid is in contact with the entire surface including the valleys caused by surface roughness. Both micro and nanoscale roughness influence surface wettability [51].

Figure 4.4. Depiction of the a) Wenzel state and the b) Cassie state.



If the droplet does not penetrate the grooves on the surface, the Cassie state exists. A droplet in the Cassie state is shown in Figure 4.4b. The Cassie equation describes a surface with two different surface chemistries [52]:

$$\cos\theta_m = x_1\cos\theta_{Y1} + x_2\cos\theta_{Y2} \quad (\text{Equation 4.3})$$

where x_1 and x_2 are the area fraction of each type of surface chemistry. When air is considered the second chemistry along with the surface chemistry, the Cassie-Baxter state prevails [52].

This state is represented as:

$$\cos\theta_m = x_1(\cos\theta_Y + 1) - 1 \quad (\text{Equation 4.4})$$

where the contact angle against liquid and air is considered 180 and x_2 equal to $1-x_1$.

In this study, the contact angle is measured by the static sessile drop method in which a camera records an image of the drop on the sample surface. Drops were dispensed by a 2 ml Ramé-Hart micro-syringe graduated in 2 μL increments. The droplet size was 6 μL . Images of the droplets were recorded with an Infinity 2 CCD camera and Infinity Analyze 6.4 software. The angle between the liquid/solid interface and the liquid/vapor interface was measured by the Drop Shape Analysis ImageJ plugin. Contact angle values are reported as the average of measurements of three different positions.

4.2.3.2. Surface Roughness

Surface roughness can be conveyed using multiple parameters. The two most common roughness parameters are the arithmetic mean roughness (R_a) and the root mean square roughness (R_{RMS}). R_a is the most used one-dimensional parameter and can be calculated by:

$$R_a = \frac{1}{n} \sum_{i=1}^n |y_i| \quad (\text{Equation 4.5})$$

where n is the number of data points and y_i is the vertical distance from the mean line. R_{RMS} or R_q is the represented by:

$$R_q = \sqrt{\frac{1}{n} \sum_{i=1}^n y_i^2} \quad (\text{Equation 4.6})$$

and provides the standard deviation of surface height. The film thickness and roughness measurements were performed with a Veeco Dektak 150 stylus profilometer. Roughness and thickness measurements were reported as an average of three measurements. The stylus tip had a tip size of 12.5 μm and a force of 1mg was applied to each sample. The scan length was 600 μm and the measurement (vertical) range was 65.5 μm . The scan speed was 10 $\mu\text{m/s}$.

4.2.3.3. Surface Morphology and Microstructure

The structure and phase composition of the modified zaccagnaites films were identified by X-ray diffraction (XRD) with a Siemens D500 diffractometer using Cu K α radiation ($\lambda = 1.5405 \text{ \AA}$) in a standard Bragg-Brentano configuration. The X-ray tube was operated at 35 kV and 24 mA. Each sample was scanned from 2.0° to 50° (2 θ), with a step size of 0.05° and a dwell time of 1.0 seconds. The surface morphology of the films was characterized by scanning electron microscopy (SEM) with an X-ray dispersive spectroscopy (EDX) attachment (FEI Quanta 200 ESEM). A spot size of 3.0 and an accelerating voltage of 25 kV were used. A Perkin Elmer Spectrum One FT-IR Spectrophotometer was used to analyze the composition of the films. The films were scraped off with a blade and ground up further before being placed onto an ATR attachment. Each sample was scanned 16 times at a wavenumber range of 4000 – 450 cm^{-1} .

4.3. Results and Discussion

4.3.1. Stainless Steel Substrate

Table 4.2. Surface roughness parameters and SWCA of SS (n=3).

R_a (nm)	R_{RMS} (nm)	SWCA (°)
7 ± 1	8 ± 1	51.7 ± 3.4

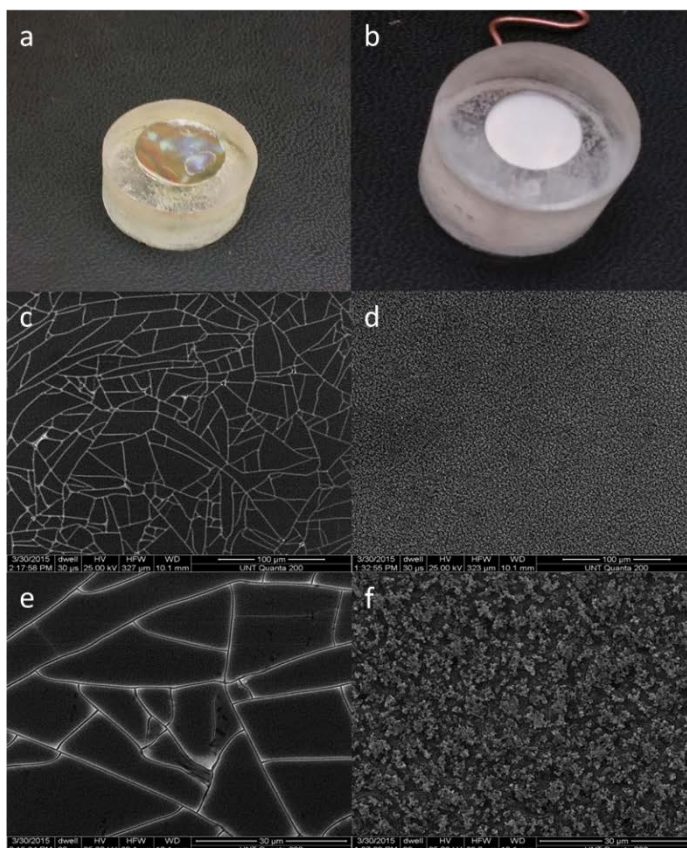
The wettability of the bare SS substrate was examined before synthesizing the SHP films. SS is a high surface energy material and is therefore expected to display high wettability. The substrate was polished extensively before measuring the SWCA so most of the iron and chromium oxide and hydroxides that usually exist in a thin surface layer were removed. The experimentally measured SWCA for SS is displayed in Table 4.2 and was determined to be 51.7°. The roughness parameters of R_a and R_{RMS} were measured as 7 and 8 nm respectively. Such low roughness values are expected for a polished metal.

4.3.2. Influence of Film Electrodeposition Potential

Film deposition potential was varied to observe any effects on the film microstructure. The formation of surface microstructures and increased surface roughness will lead to better SHP surfaces. Depositions at a potential of -1.0 V resulted in a mostly transparent film displaying colorful interference patterns as shown in Figure 4.5a. When the applied potential was increased to -1.3 V, the film became white and opaque observed in Figure 4.5b. Higher deposition potentials resulted in excessive hydrogen evolution at the electrode surface causing

the films to be less adherent to the substrate. The surface morphology of the two films is completely different. The SEM images of the -1.0 V film in Figure 4.5c and e have a spider web appearance. Also, the surface is homogeneous and appears very smooth. When the potential is increased to -1.3 V, the morphology completely changes. SEM images in Figure 4.5d show a homogeneous and highly textured surface. A further magnified SEM image in Figure 4.5f shows amorphous structures on top of a flat underlying phase with much void space between these structures.

Figure 4.5. Digital images of the a) -1 V film and b) -1.3 V film. Low magnification SEM images of film deposited at c) -1.0 V film and d) -1.3 V film and higher magnification SEM images of e) -1.0 V film and f) -1.3 V film.



Profilometer studies of the films are shown in Table 4.3. The thickness of the higher potential film is 3 times that of the lower potential film (2515 vs. 862 nm). As expected a large increase in roughness is observed with the -1.3 V film displaying much higher surface roughness values than the -1.0 V film. The R_a and R_{RMS} are approximately 6 and 5 times higher respectively for -1.3 V film. The -1.3 V film was selected for further study because of its superior surface roughness.

Table 4.3. Film thickness and roughness values (n=3).

Film	Thickness (nm)	R_a (nm)	R_{RMS} (nm)
-1V (3 min)	862 ± 12	29 ± 4	43 ± 10
-1.3V (3 min)	2515 ± 83	180 ± 10	222 ± 15

4.3.3. Influence of Film Deposition Time

Table 4.4. Elemental analysis, roughness parameters, and SWCA of 1, 2, and 3 min modified zaccagnaite/palmitate film depositions at -1.3 V (n=3).

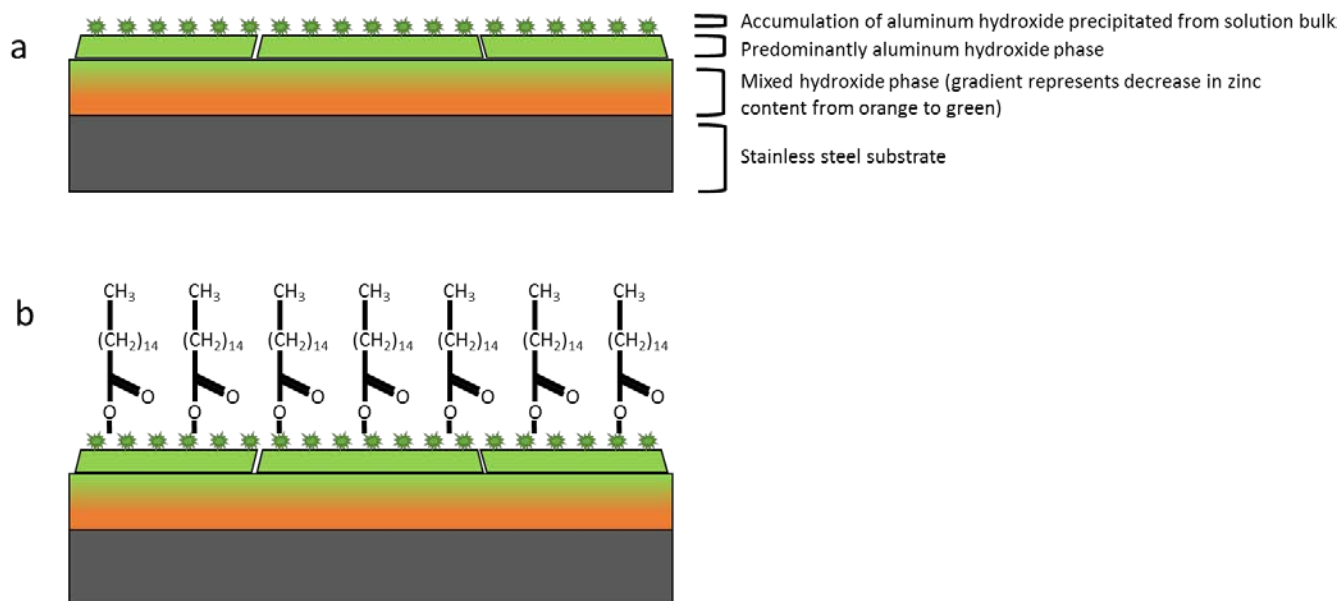
Film	R_a (nm)	R_{RMS} (nm)	Atomic %Zn	Atomic %Al	Zn:Al Ratio	SWCA (°)
-1.3V (1 min)	123 ± 5	158 ± 6	30 ± 1	70 ± 1	1:2.3	165.5 ± 2.1
-1.3V (2 min)	151 ± 8	198 ± 21	14 ± 3	86 ± 3	1:6.1	168.4 ± 1.4
-1.3V (3 min)	180 ± 10	222 ± 15	12 ± 2	88 ± 2	1:7.3	169.9 ± 0.7

The influence of electrochemical deposition time of the modified zaccagnaite film was investigated. The film was deposited for times of 1, 2, and 3 min before undergoing the immersion reaction with palmitic acid. Roughness measurements were performed on the films before the reaction. Table 4.4 shows that both roughness parameters increase as the deposition time increased. A deposition time of 3 min was chosen as the cutoff because longer depositions can result in poor adhesion or films that display fractures because the greater mass results in greater stress on the film especially during drying.

EDX measurements were also performed on the films and the results were displayed in Table 4.4. The aluminum content of the films increased with deposition time. The 1, 2, and 3 min films exhibited Zn:Al ratios of 1:2.3, 1:6.1, and 1:7.3 respectively. These metal ratios are outside the limits for acceptable values (1.6:1 – 4:1) of LDHs and are caused by a high deposition potential [42]. Higher deposition potentials create an excess of OH^- which is not consumed at the electrode. These hydroxides diffuse to the bulk causing the precipitation of aluminum hydroxide which codeposits with the LDH and eventually dominates the surface of the film. A schematic of the film is shown in Figure 4.6a. This aluminum hydroxide is responsible for the increased surface roughness displayed at higher deposition potentials.

The hydrophobization reaction with palmitic acid results in the carboxylic head group reacting with the hydroxide group on the film surface [53]. The reaction mechanism involves the formation of Al-O bonds caused by a dehydration reaction between surface hydroxides and the carboxylic acid head group of the palmitic acid. The carboxylate group of the palmitate ion bonds to aluminum and the hydrocarbon tail is oriented away from the surface observed in Figure 4.6b.

Figure 4.6. Schematic of film composition a) before and b) after hydrophobization reaction.



The parameters of the surface reaction (0.1 M palmitic acid concentration, 7 h hydrophobization duration, 70° C reaction temperature) were kept the same when testing the different deposition times. The SWCA of the films deposited for different durations, shown in Table 4.4, were very close to each other, but correlated with the roughness parameters. The SWCA of the 1, 2, and 3 min modified zaccagnaite/palmitate films were 165.5°, 168.4°, and 169.9° respectively indicating that the roughness of the films were similar, but increased slightly with deposition time. The 3 min film was determined to be the optimum deposition time.

4.3.4. Influence of Palmitic Acid Concentration in Hydrophobization Reaction

The effect of palmitic acid concentration on SWCA was determined by examining the concentrations of 0.05, 0.1, and 0.2 M palmitic acid. The remaining parameters of deposition time (3 min), hydrophobization time (7 h), and hydrophobization temperature (70°C) were kept the same. The results in Table 4.5 show that the SWCA increased from 164.0° to 169.9° when

the concentration increased from 0.05 to 0.1 M, but decreased to 166.5° when the concentration was increased to 0.2 M. The optimum palmitic acid concentration was determined to be 0.1 M.

Table 4.5. SWCA of modified zaccagnait/palmitate films where the palmitic acid concentration varied while the other parameters are kept static (3 min film electrodeposition time, 7 h hydrophobization reaction time at 70° C) (n=3).

Palmitic Acid Concentration (M)	SWCA (°)
0.05	164.0 ± 1.7
0.1	169.9 ± 0.7
0.2	166.5 ± 0.1

4.3.5. Influence of Hydrophobization Time

Table 4.6 shows the SWCA measurements of different reaction times (5, 7, and 9 h). The remaining film parameters were an electrodeposition time of 3 min, 0.1 M palmitic acid concentration, and a hydrophobization reaction temperature of 70° C. SWCA values increased from 165.1° to 169.9 from 5 to 7 h and decreased very slightly to 169.2 when the hydrophobization time increased to 9 h. An optimal reaction time of 7 h was determined.

Table 4.6. SWCA of modified zaccagnaite/palmitate films where the hydrophobization reaction time varied while the other parameters kept static (3 min film electrodeposition time, 0.1M palmitic acid concentration, hydrophobization reaction performed at 70° C) (n=3).

Immersion Time (h)	SWCA (°)
5	165.1 ± 0.5
7	169.9 ± 0.7
9	169.2 ± 0.4

4.3.6. Influence of Hydrophobization Temperature

Table 4.7. SWCA of modified zaccagnaite/palmitate films where the hydrophobization reaction temperature varied while the other parameters were kept static (3 min film deposition, 0.1M palmitic acid concentration, 7 h hydrophobization reaction time) (n=3).

Reaction Temperature (C)	SWCA (°)
20	163.4 ± 1.2
40	167.5 ± 0.3
70	169.9 ± 0.7

Films were subjected to different reaction temperatures while all other parameters were static (3 min film deposition time, 0.1 M palmitic acid concentration, 7 h hydrophobization duration). The films were reacted at 20°, 40°, and 70° C. A maximum temperature of 70° C was selected because of the 78°C boiling point of ethanol. Table 4.7 shows that the SWCA of the

films increased slightly when the temperature was increased. A hydrophobization temperature of 70° C produced a film with a SWCA of almost 170° C.

Figure 4.7. SEM of modified zaccagnaite/palmitate film at a) high and b) low magnification.

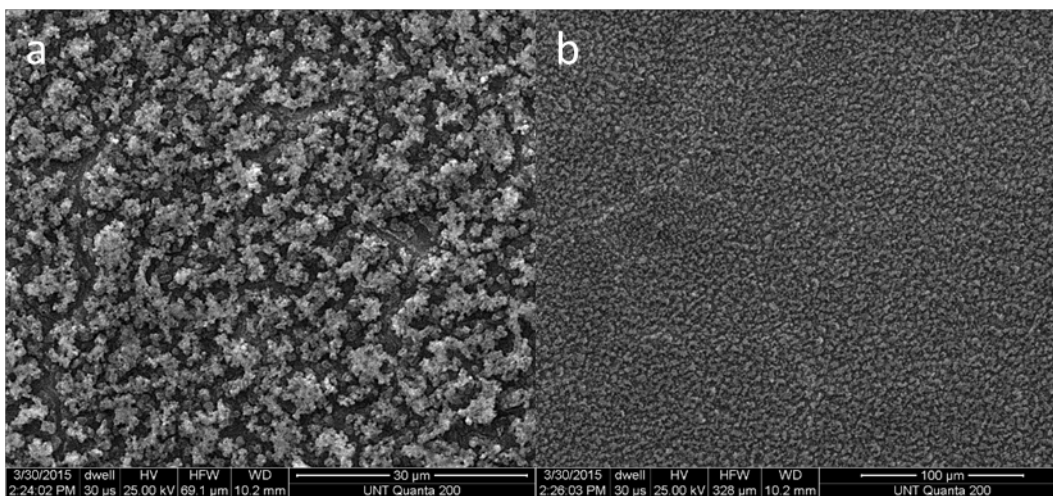


Figure 4.8. Comparison of SWCA on a) SS, b) modified zaccagnaite, and c) optimized zaccagnaite/palmitate film.



SEM images of the modified zaccagnaite/palmitate film at high and low magnification are shown in Figure 4.7a and b. Many voids or cavities can be observed from the morphology allowing air to be trapped in the surface. Trapped air on the surface is key to hydrophobicity

because water droplets will rest on a layer of air [54]. Digital images of the water droplets on SS, modified zaccagnaite film, and the modified zaccagnaite/palmitate film are shown in Figure 4.8. The SWCA decreased when the modified zaccagnaite was deposited on SS, but increased dramatically when the monolayer of low-surface-energy palmitic acid bonded to the surface.

4.3.7. Film Structure

Films were deposited for 3 min and 15 min and examined with XRD. Films were deposited for a 15 min because of the weak intensity of the 3 min film diffraction pattern. The XRD pattern of the modified zaccagnaite films deposited on SS is displayed in Figure 4.9. The structure of LDH is observed even though its Zn:Al content is outside the acceptable limits [55]. Only the (003) reflection at 10.05° is observed in the diffraction pattern of the 3 min film. The weak intensity of the (003) reflection is due to the small amount deposited on the SS substrate. Both the (003) and (006) reflections at 9.90° and 19.85° respectively are observed in the 15 min diffraction pattern. Peaks from the SS substrate can be observed at 42.65° and 44.60° . The 3 min and 15 min films display basal spacings of 0.88 and 0.89 nm which agree with previous research [56-58]. The diffraction peaks are broad because electrosynthesized LDHs exhibit poor crystallinity and nitrate can be intercalated in two different orientations [41,59].

The FTIR spectra of palmitic acid, modified zaccagnaite, and modified zaccagnaite/palmitate are shown in Figure 4.10. The FTIR spectrum of the modified zaccagnaite shows the presence of LDH just like the XRD data. The O-H stretching of hydroxides and water in the interlayer region is seen as a broad peak at 3499 cm^{-1} . The bending vibration of the interlayer water molecules is observed at 1589 cm^{-1} and asymmetric stretching of nitrate ions in

the interlayer region is attributed to the peak at 1340 cm^{-1} [56]. Al-O stretching modes are observed at 820 and 555 cm^{-1} [55,58,59]. Peaks from 2700 - 1800 cm^{-1} are from the diamond ATR surface [62]. The modified zaccagnaite/palmitate film exhibits new peaks. Peaks at 2918 and 2851 cm^{-1} correspond to asymmetric and symmetrical CH_2 stretching and are evidence of bond creation between the surface aluminum and the carboxylate of the palmitate ion [63].

Figure 4.9. XRD patterns of modified zaccagnaite films deposited for 3 min and 15 min.

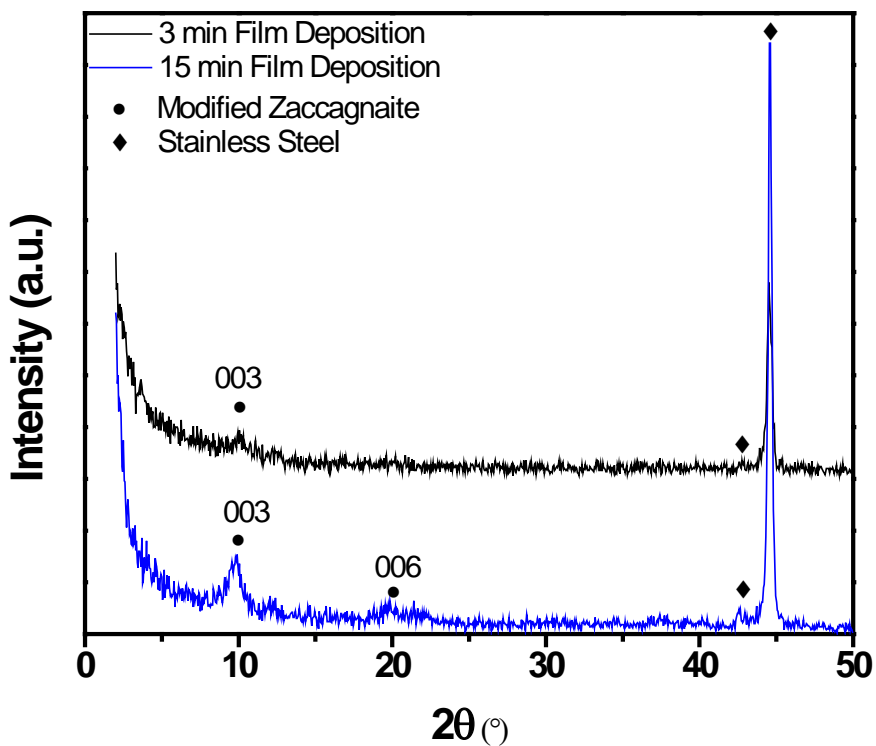
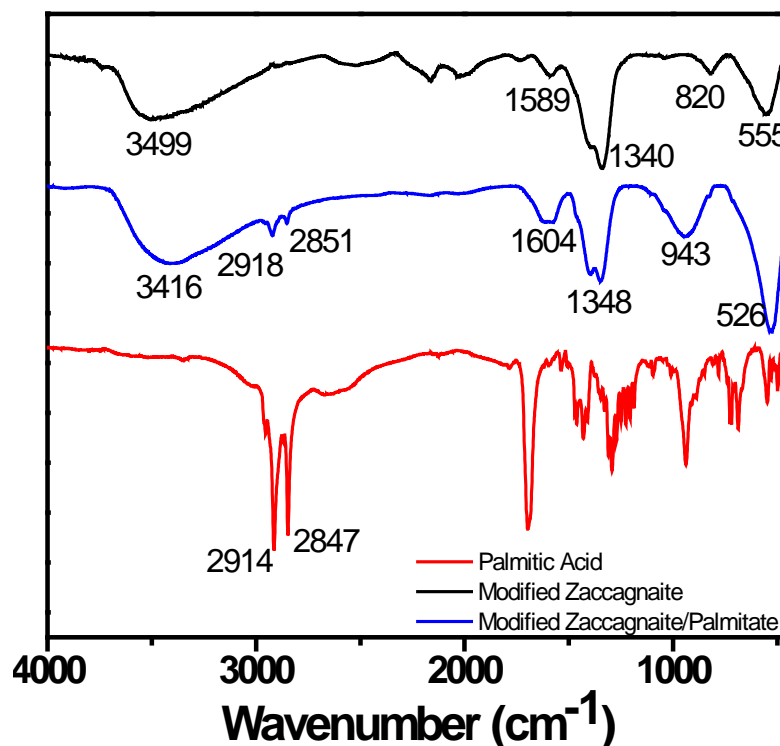


Figure 4.10. FT-IR spectra of a) palmitic acid, b) modified zaccagnaite film, and c) the modified zaccagnaite/palmitate film.



4.4. Chapter Conclusions

The optimal conditions for the fabrication of SHP surfaces on SS using a modified zaccagnaite film to generate surface roughness and palmitic acid as the low energy surface material were explored. A film deposition potential of -1.3 V, deposition time of 3 min, palmitic acid concentration of 0.1 M, hydrophobization time of 7 h, and a hydrophobization temperature of 70°C produced a SWCA of 169.9°. SEM and profilometry showed that a film displaying high surface roughness was generated at -1.3 V. EDX measurements revealed that an aluminum hydroxide phase existed over a mixed phase of zinc and aluminum hydroxide. XRD indicated that this film retained the crystal structure of LDH even though the Zn:Al metal

content was outside the acceptable limits for LDH. FTIR analysis of the modified zaccagnaite/palmitate films showed that the palmitic acid formed bonds with the surface aluminum hydroxide to change the surface from highly hydrophilic to superhydrophobic.

4.5. References

- [1] S. S. Latthe, P. Sudhagar, C. Ravidhas, A. J. Christy, D. D. Kirubakaran, R. Venkatesh, A. Devadoss, C. Terashima, K. Nakata, A. Fujishima, *Cryst. Eng. Comm.*, 2015, 17, 2624-2628.
- [2] X. Zhang, J. Liang, B. Liu, Z. Peng, *Colloids Surf. A Physicochem. Eng. Asp.*, 2014, 454, 113-118.
- [3] J. Seo, S. Lee, J. Lee, T. Lee. *ACS Appl. Mater. Interfaces*, 2011, 3, 4722-4729.
- [4] C. Xue, P. Ji, P. Zhang, Y. Li, S. Jia, *Appl. Surf. Sci.*, 2013, 284, 464-471.
- [5] A. M. Emelyanenko, F. M. Shagieva, A. G. Domantovsky, L. B. Boinovich, *Appl. Surf. Sci.*, 2015, 332, 2015.
- [6] R. Blossey, *Nature Mater.*, 2003, 2, 301-306.
- [7] L. Feng, S. Li, Y. Li, H. Li, L. Zhang, J. Zhai, Y. Song, B. Liu, L. Jiang, D. Zhu, *Adv. Mater.*, 2002, 14, 1857-1860.
- [8] R. Furstner, W. Barthlott, C. Neinhuis, P. Walzel, *Langmuir*, 2005, 21, 956-961.
- [9] X. F. Gao, L. Jiang, *Nature*, 2004, 432, 36-36.
- [10] W. Lee, M.K. Jin, W.C. Yoo, J. K. Lee, *Langmuir*, 2004, 20, 7665-7669.
- [11] S. Shibuichi, T. Yamamoto, T. Onda, and K. Tsujii, *J. Colloid Interface Sci.*, 1998, 208, 287-294.
- [12] Q. Liu, D. Chen, Z. Kang, *ACS Appl. Mater. Interfaces*, 2015, 7, 1859-1867.

- [13] B. Jeong, E. Jung, J Kim, *Appl. Surf. Sci.*, 2014, 307, 28-32.
- [14] W. Huang, C. Lin, *Appl. Surf. Sci.*, 2014, 305, 702-709.
- [15] R. Liao, Z. Zuo, C. Guo, Y. Yuan, A. Zhuang, *Appl. Surf. Sci.*, 2014, 317, 701-709.
- [16] S. Rezaei, I. Manoucheri, R. Moradian, B. Pourabbas, *Chem. Eng. J.*, 2014, 252, 11-16.
- [17] J. P. Fernández-Blázquez, D. Fell, E. Bonaccorso, A. del Campo, *J. Colloid Interface Sci.*, 2011, 357, 234-238.
- [18] X. Wen, C. Ye, Z. Cai, S. Xu, P. Pi, J. Cheng, L. Zhang, Y. Qian, *Appl. Surf. Sci.*, 2015, 339, 109-115.
- [19] H. Cho, D. Kim, C. Lee, W. Hwang, *Curr. Appl. Phys.*, 2013, 13, 762-767.
- [20] N. Zhan, Y. Li, C. Zhang, Y. Song, H. Wang, L. Sun, Q. Yang, X. Hong, *J. Colloid Interface Sci.*, 2010, 345, 491-495.
- [21] L. Zhang, Y. Li, J. Sun, J. Shen, *J. Colloid Interface Sci.*, 2008, 319, 302-308.
- [22] L. Zhang, Z. Zhou, B. Cheng, J. M. DeSimone, E. T. Samulski, *Langmuir*, 2006, 22, 8576-8580.
- [23] H. Yan, K. Kurogi, H. Mayama, K. Tsujii, *Angew. Chem. Int. Ed.*, 2005, 44, 3453-3456.
- [24] N. R. Baddoo, *J. Constr. Steel Res.*, 2008, 64, 1199-1206.
- [25] A. Latifi, M. Imani, M. T. Khorasani, M. D. Joupari, *Surf. Coat. Technol.*, 2013, 221, 1-12.
- [26] T. J. Mesquita, E. Chauveau, M. Mantel, N. Bouvier, D. Koschel, *Corros. Sci.*, 2014, 81, 152-161.
- [27] G. Herting, I. O. Wallinder, C. Leygraf, *J. Food Eng.*, 2008, 87, 291-300.
- [28] C. Bitondo, A. Bossio, T. Monetta, M. Curioni, F. Bellucci, *Corros. Sci.*, 2014, 87, 6-10.
- [29] T. K. Ha, H. T. Jeong, H. J. Sung, *J. Mater. Process. Technol.*, 2008, 187-188, 555-558.
- [30] M. A. Akl, M. A. Ahmed, A. Ramadan, *J. Pharm. Pharmacol.*, 2011, 55, 247-252.

- [31] N. J. Shirtcliffe, G. McHale, M. I. Newton, Y. Zhang, *ACS Appl. Mater. Interfaces*, 2009, 1, 1316-1323.
- [32] L. Li, V. Breedveld, D. W. Hess, *Appl. Mater. Interfaces*, 2012, 4, 4549-4556.
- [33] L. J. Chen, M. Chen, H. D. Zhou, J. M. Chen, *Appl. Surf. Sci.*, 2008, 255, 3459-3462.
- [34] Q. Huang, Y. Yang, R. Hu, C. Lin, L. Sun, E. A. Vogler, *Colloids Surf., B.*, 2015, 125, 134-141.
- [35] C. Lee, A. Kim, J. Kim, *Surf. Coat. Technol.*, 2015, 264, 127-131.
- [36] B. Wu, M. Zhou, J. Li, X. Ye, G. Li, L. Cai, *Appl. Surf. Sci.*, 2009, 256, 61-66.
- [37] H. Yang, P. Pi, Z. Cai, X. Wen, X. Wang, J. Cheng, Z. Yang, *Appl. Surf. Sci.*, 2010, 256, 4095-4102.
- [38] M. A. Frank, A. R. Boccaccini, S. Virtanen, *Appl. Surf. Sci.*, 2014, 311, 753-757.
- [39] X.X. Guo, S.L. Xu, L.L. Zhao, W. Lu, F.Z. Zhang, D.G. Evans, X. Duan, *Langmuir*, 2009, 25, 9894-9897.
- [40] Y. Zhao, Z. Xu, X. Wang, T. Lin, *Appl. Surf. Sci.*, 2013, 286, 364-370.
- [41] I. Gualandi, M. Monti, E. Scavetta, D. Tonelli, V. Prevot, C. Mousty, *Electrochim. Acta*, 2015, 152, 75-83.
- [42] M. Montia, P. Benitoa, F. Basilea, G. Fornasaria, M. Gazzanob, E. Scavettaa, D. Tonellia, A. Vaccaria, *Electrochim. Acta*, 2013, 108, 596-604.
- [43] K.N. Prabhu, P. Fernandes, G. Kumar, *Mater. Des.*, 2009, 2, 297-305.
- [44] X. Zhao, M.J. Blunta, J.J. Yao, *Pet. Sci. Technol. Eng.*, 2010, 71, 169-178.
- [45] Y.Q. Wang, H.F. Yang, Q.G. Hang, L. Fang, S.R. Ge, *Adv. Mater. Res.*, 2010, 1019, 154-155.
- [46] M. Sakai, T. Yanagisawa, A. Nakajima, Y. Kameshima, K. Okada, *Langmuir*, 2009, 25, 13-16.
- [47] Y. Son, C. Kim, D.H. Yang, D.J. Ahn, *Langmuir*, 2008, 24, 2900-2907.

- [48] J. Perelaer, C.E. Hendriks, A.W.M. de Laat, U.S. Schubert, *Nanotechnology*, 2009, 20, 165303-165307.
- [49] T. Young, *Philos. Trans. R. Soc. Lond.*, 1805, 95, 65-87.
- [50] R. N. Wenzel, *Ind. Eng. Chem. Res.*, 1936, 28, 988-994.
- [51] C. T. Hsieh, W. Y. Chen, F. L. Wu, *Carbon*, 2008, 46, 1218-1224.
- [52] A. B. D. Cassie and S. Baxter, *J. Chem. Soc. Faraday Trans.*, 1944, 40, 546-551.
- [53] D. L. Allara, R. G. Nuzzo, *Langmuir*, 1985, 1, 52-66.
- [54] E. Hosono, S. Fujihara, I. Honma, H.J. Zhou, *Am. Chem. Soc.*, 2005, 127, 13458–13459.
- [55] D.G. Evans, R.C.T. Slade, *Struct. Bond.*, 2006, 119, 1–87.
- [56] M.S. Yarger, E.M.P. Steinmiller, K.S. Choi, *Inorg. Chem.*, 2008, 47, 5859–5865.
- [57] F. Wu, J. Liang, Z. Peng, B. Liu, *Appl. Surf. Sci.*, 2014, 313, 834–840.
- [58] A. de Roy, C. Forano, J.P. Besse, Layered double hydroxides: synthesis and post-synthesis modification, in: V. Rives (Ed.), *Layered Double Hydroxides: Present and Future*, Nova Science Publishers, Inc., New York, 2001, pp. 1-39.
- [59] Radha, S. and Kamath, P. V., *Z. anorg. allg. Chem.*, 2012, 638, 2317–2323.
- [60] J. T. Klopprogge, R. L. Frost, L. Hickey, *J. Raman Spectrosc.*, 2004, 35, 967–974.
- [61] Y. Lin, J. Wang, D. G. Evans, D. Li, *J. Phys. Chem. Solids*, 2006, 67, 998-1001.
- [62] G. Hu, N. Wang, D. O'Hare, J. Davis, *J. Mater. Chem.*, 2007, 17, 2257-2266.
- [63] M. Ruan, W. Li, B. Wang, Q. Luo, F. Ma, Z. Yu, *Appl. Surf. Sci.*, 2012, 258, 7031– 7035.

CHAPTER 5

CORROSION RESISTANCE OF SUPERHYDROPHOBIC AND HYDROPHOBIC MODIFIED

ZACCAGNAITE FILMS ON STAINLESS STEEL

5.1. Introduction

Corrosion damage is one of the leading causes of metal components failure. Component failure can result in loss of revenue due to equipment downtime and damage to components. The cost of metal corrosion has been estimated to amount to several percent of a nation's GDP [1]. Corrosion cannot be stopped but it can be slowed through the use of different alloys, inhibitors, and protective coatings especially in certain aggressive environments. Stainless steels are relatively cheap and versatile materials because of the number of elements that can be incorporated. They are used in a number of industries [2-8]. Its strength comes from the minimum 10.5% chromium content which results in the formation of a protective oxide layer in oxygen rich environments. Stainless steels are corrosion resistant in many environments but are susceptible to local corrosion in chloride environments [9,10]. The oxide layer is degraded quicker than it can be formed. As a result, stainless steel components are often protected by films or coatings when employed in corrosive environments [11,12]. The industry standard, chromate coatings, is effective but is detrimental to the environment and slowly being phased out for more eco-friendly materials.

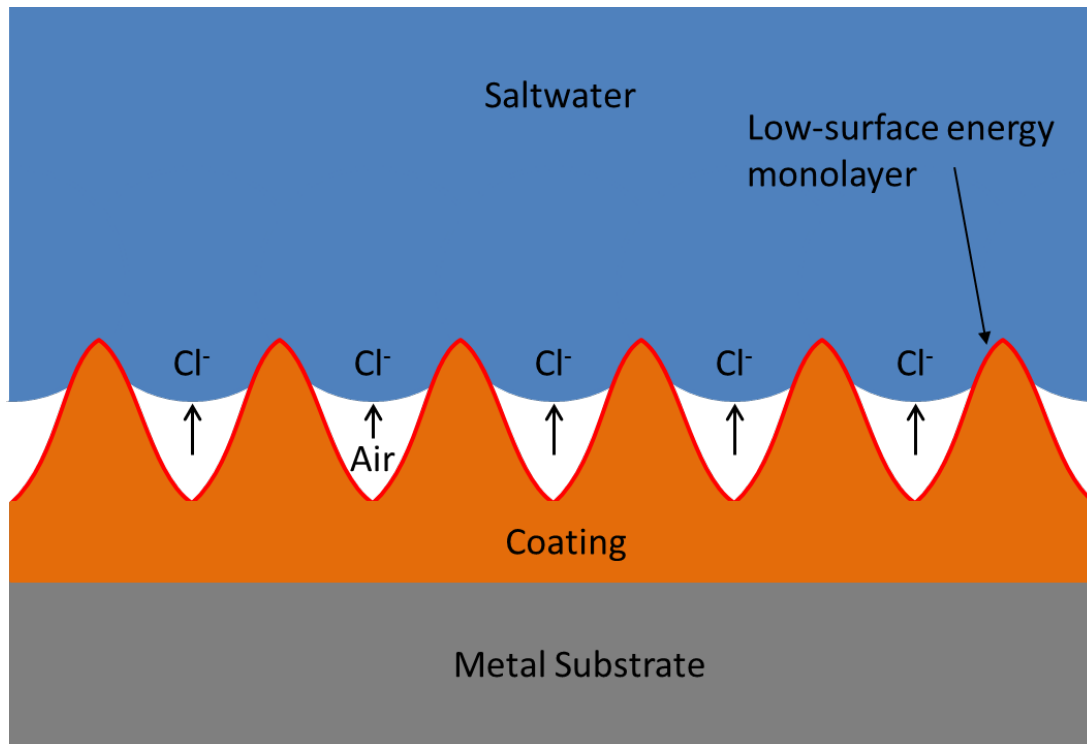
Layered double hydroxides have been investigated recently as corrosion resistant coatings [13-15]. They can be fabricated numerous ways but in situ synthesis is desired because of the stronger adhesion due to chemical bonding between the coating and substrate [16]. LDHs make great corrosion coatings because of their barrier properties, minimal environmental

impact, insulating nature (when synthesized without transition metal cations), anion exchange/trapping ability, and in some cases self-healing capabilities [17-20].

Superhydrophobic (SHP) surfaces have a static water contact angle greater than 150° and can impart more corrosion resistance to coatings via their water repellency [21,22]. SHP surfaces are constructed by combining high surface roughness and low-surface energy materials. Surface roughness can be generated through a number of methods [23-29]. Surface roughness allows for the trapping of air in the nano/microstructure of the surface. If the surface is modified with a hydrophobic monolayer such as a long chain fatty acid, the trapped air can push water away from the substrate minimizing contact with water as seen in Figure 5.1 [30]. Exposure to corrosive agents in water (chlorides, sulfates, etc.) is minimized by the SHP surface. When the barrier properties of a coating are combined with the water repellency of a SHP monolayer, corrosion resistance is greatly enhanced [31,32].

The deposition of layered double hydroxide films can provide the surface roughness that is the basis for SHP surfaces. Hydrothermal synthesis of LDH films allows for tunable surface roughness [33]. Modification of these films with low surface energy materials such as long chain fatty acids, or 1H,1H,2H,2H-Perfluorodecyltrimethoxysilane (PFDTMS) can produce SHP surfaces [34,35]. Some of these SHP LDH films have been subjected to corrosion testing in simulated seawater [31,32,34]. Another study has shown how these films resist microbial induced corrosion [36]. All previous literature involves the use of magnesium or aluminum as the substrate and none of the films were fabricated by electrochemical synthesis.

Figure 5.1. Illustration of SHP surface water repellency.



In this study, two different modified zaccagnaite (MZ) films are fabricated on SS 430 substrates using electrochemical synthesis. One film is deposited at -1.0 V (vs. SCE) and the other at -1.3 V. Both films underwent surface treatment with palmitic acid to form a hydrophobic surface on the -1.0 V modified zaccagnaite/palmitate (MZ/P) film and a SHP surface on the -1.3 V film MZ/P. The structure and morphology of the films were characterized by X-ray diffraction (XRD), Fourier transform infrared (FTIR) spectroscopy, and scanning electron microscopy (SEM). The corrosion resistance of the films was evaluated by potentiodynamic polarization and electrochemical impedance spectroscopy (EIS).

5.2. Experimental

5.2.1. Substrate Preparation and Film Synthesis

The substrates were SS 430 discs from Ted Pella, Inc. with a diameter of 10 mm, a thickness of 0.76 mm and an area of 0.95 cm². The substrates contained <0.12% C, 16-18% Cr, <0.75% Ni, <1.0% Mn, <1.0% Si, <0.040% P, and <0.030% S by weight. The discs were degreased by rough polishing with grit paper and then sonicated in acetone. The substrates were then attached to coiled copper wire leads with conductive silver epoxy. Once dry they were mounted in epoxy utilizing molds. After curing, the mounted electrodes were polished with SiC and diamond to a mirror finish followed by ultrasonication in ethanol.

The electrolytic solution was prepared by dissolving a 2:1 molar ratio of Zn²⁺ to Al³⁺ ions in distilled water. Aluminum nitrate nonahydrate (Al(NO₃)₃•9H₂O, Alfa Aesar) was the aluminum source, zinc nitrate hexahydrate (Zn(NO₃)₂•6H₂O, Alfa Aesar) was the source of zinc and potassium nitrate (KNO₃, Fisher Scientific) was used as the electrolyte to help facilitate the formation of MZ film at the electrode surface. The electrolytic concentration of each compound was determined to be 0.02 M Zn(NO₃)₂•6H₂O, 0.01 M Al(NO₃)₃•9H₂O and 0.2 M KNO₃. An EG&G Princeton Applied Research (PAR) Model 273A potentiostat/galvanostat was used to electrochemically deposit films. The depositions were performed at room temperature utilizing a three-electrode configuration under a nitrogen atmosphere. The working electrode was a SS disc, a platinum mesh was used as the counter electrode, and the reference electrode was a saturated calomel electrode (SCE). Films were deposited at -1.0 V and -1.3 V for 3 min. Stirring was used to mitigate hydrogen evolution. The films were rinsed with distilled water and air dried at room temperature.

5.2.2. Film Hydrophobization

The hydrophobization reaction was performed by immersion of the sample in ethanol solution containing dissolved palmitic acid. The immersion reaction was performed in 0.1 M palmitic acid solution for 7 h at 70° C. The films were then rinsed with ethanol and allowed to air dry.

5.2.3. Characterization

The structure and phase composition of the modified zaccagnaite films were identified by X-ray diffraction (XRD) with a Siemens D500 diffractometer using Cu K α radiation ($\lambda = 1.5405$ Å) in a standard Bragg-Brentano configuration. The X-ray tube was operated at 35 kV and 24 mA. Each sample was scanned from 2.0° to 50° (2 θ), with a step size of 0.05° and a dwell time of 1.0 seconds. The surface morphology of the films was characterized by scanning electron microscopy (SEM) with an X-ray dispersive spectroscopy (EDX) attachment (FEI Quanta 200 ESEM). A spot size of 3.0 and an accelerating voltage of 25 kV were used. A Perkin Elmer Spectrum One FT-IR Spectrophotometer was used to analyze the composition of the films. The films were scraped off with a blade and ground up further before being placed onto an ATR attachment. Each sample was scanned 16 times at a wavenumber range of 4000 – 450 cm⁻¹.

5.2.4. Contact Angle Measurement

In this study, the static water contact angle (SWCA) is measured by the static sessile drop method in which a camera records an image of the drop on the sample surface. Drops were dispensed by a 2 ml Ramé-Hart micro-syringe graduated in 2 μ L increments. The droplet

size was 6 μL . Images of the droplets were recorded with an Infinity 2 CCD camera and Infinity Analyze 6.4 software. The angle between the liquid/solid interface and the liquid/vapor interface was measured by the Drop Shape Analysis ImageJ plugin. Contact angle values are reported as the average of measurements of three different positions.

5.2.5. Immersion Tests and Corrosion Measurements

Polarization measurements and immersion tests were performed in 3.5 wt.% NaCl aqueous solutions at room temperature. Potentiodynamic polarization tests were conducted with an EG&G Princeton Applied Research (PAR) Model 4000 potentiostat/galvanostat. Each sample was immersed in the NaCl solution for 30 min before polarization curves were measured with respect to open circuit potential (OCP) at a scan rate of 1 mV/s. EIS measurements were performed to study the corrosion behavior of the synthesized films in 3.5% NaCl before and after an 192 h immersion period. Each sample was immersed for 30 min prior to measurement in order to achieve a steady state. EIS measurements were conducted with an EG&G Princeton Applied Research (PAR) Model 4000 potentiostat/galvanostat. EIS experiments were performed from 10 kHz to 25 mHz at open circuit potential (OCP) and the perturbation voltage was 5 mV. EIS spectra were modeled with ZView 3.3 (Scribners Associates Inc.) software.

5.3. Results and Discussion

5.3.1. Structural Characterization and Morphology

The XRD patterns of -1.0 V MZ film is shown in Figure 5.2a. The film was analyzed after 15 min in addition to 3 min of electrosynthesis time because of the weak intensity of the 3 min film. The 3 min film shows a very small (003) reflection at 9.91° characteristic of LDH. When the sample is deposited for 15 min, both the (003) and (006) LDH reflections are seen at 10.02° and 20.14° . SS substrate reflections can be observed at 42.56° and 44.56° . The 3 min and 15 min films display basal spacings of 0.89 and 0.88 nm which agree with previous research [37-39].

The XRD patterns of -1.3 V MZ film are shown in Figure 5.2b. Again the film was analyzed after 15 min in addition to 3 min of electrosynthesis time because of the weak intensity of the shorter deposition. The 3 min film shows a very small (003) reflection at 10.05° characteristic of LDH. When the sample is deposited for 15 min, the (003) and (006) LDH reflections are seen at 9.90° and 19.85° . SS substrate reflections can be observed at 42.65° and 44.60° . The 3 min and 15 min films display basal spacings of 0.88 and 0.89 nm.

The FTIR spectra of palmitic acid, -1.0 V MZ, -1.3 V MZ, -1.0 V MZ/P, and -1.3 V MZ/P are shown in Figure 5.3. Table 5.1 shows that the -1.0 V MZ and -1.3 V MZ films spectra contain all the characteristic peaks of LDH including O-H stretching, H_2O bending vibration, asymmetric nitrate stretching, and Al-O stretching [37,38,40,41]. The -1.0 V MZ/P and -1.3 V MZ/P films also show all of the characteristic peaks of LDH and two additional peaks. The two additional peaks are associated with the asymmetrical and symmetrical CH_2 stretching of the palmitic acid indicating that the film has formed chemical bonds with the fatty acid [42]. Peaks from $2700\text{-}1800\text{ cm}^{-1}$ are from the diamond ATR surface [43].

Figure 5.2. XRD patterns of the a) -1.0 V MZ and b) -1.3 V MZ films.

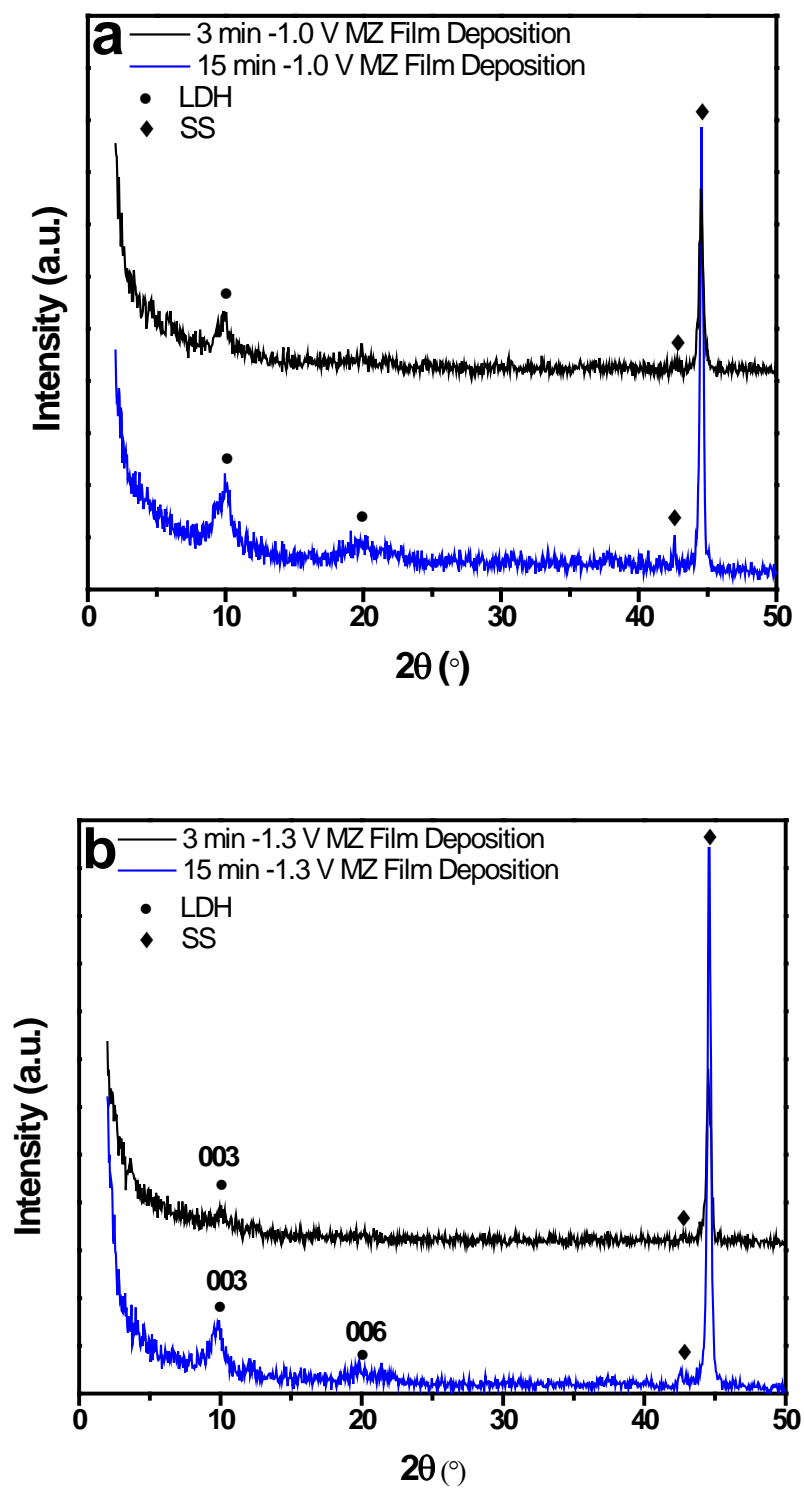


Figure 5.3. FTIR spectra of the -1.0 V MZ and -1.3 V MZ films before and after the hydrophobization reaction.

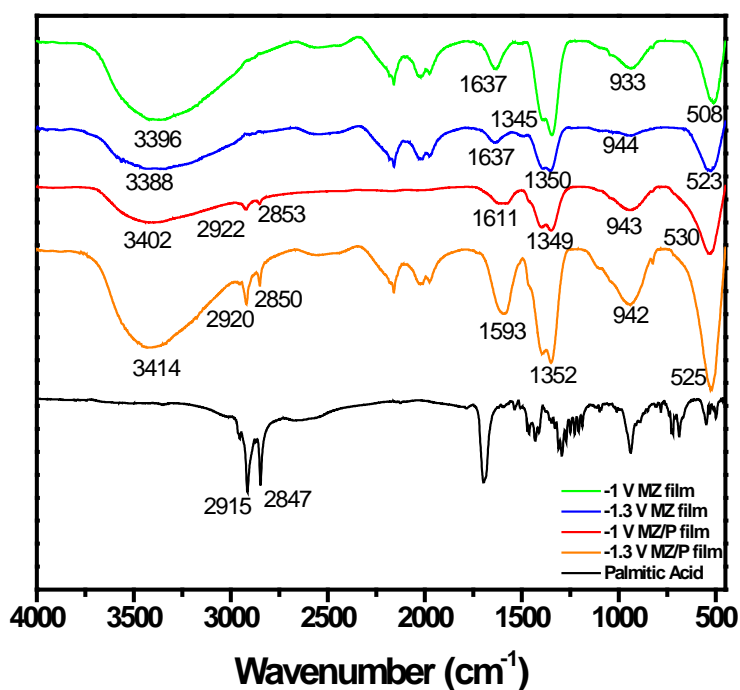
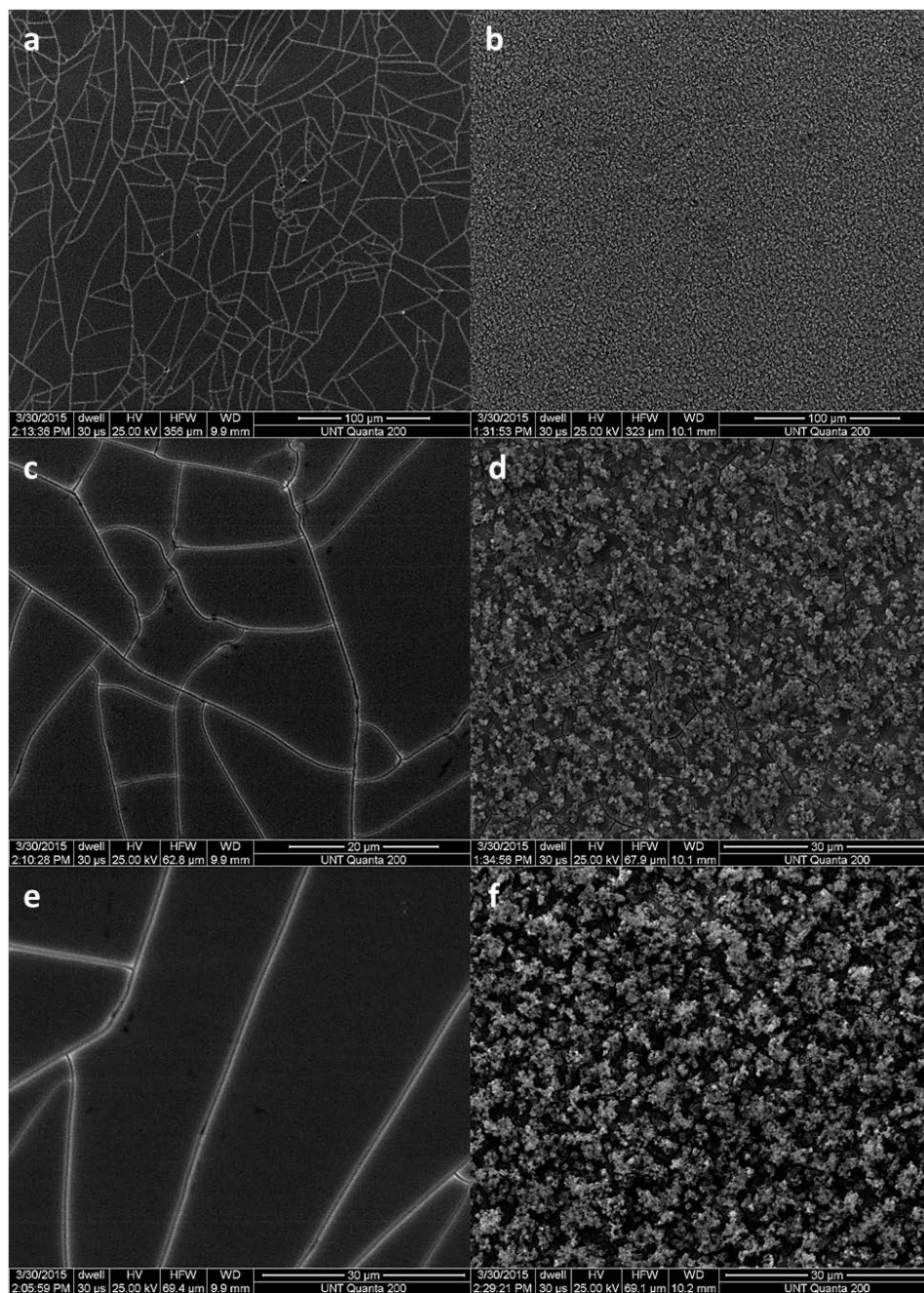


Table 5.1. FTIR Assignments of the palmitic acid, MZ, and MZ/P.

Peak Assignment	-1 V MZ	-1.3 V MZ	-1 V MZ/P	-1.3 V MZ/P	Palmitic Acid
O-H stretch	3396	3388	3402	3414	N/A
Asymmetrical CH ₂ stretch	N/A	N/A	2922	2920	2915
Symmetrical CH ₂ stretch	N/A	N/A	2853	2850	2847
Bending vibration of H ₂ O	1637	1637	1611	1593	N/A
Asymmetric NO ₃ ⁻ stretch	1345	1350	1349	1352	N/A
Al-O stretching modes	933, 508	944, 523	943, 530	942, 525	N/A

Figure 5.4. SEM images of a,c) -1 V MZ film at different magnifications and b,d) -1.3 V MZ film at different magnifications. SEM images of e) -1 V MZ/P film and f) -1.3 V MZ/P film.

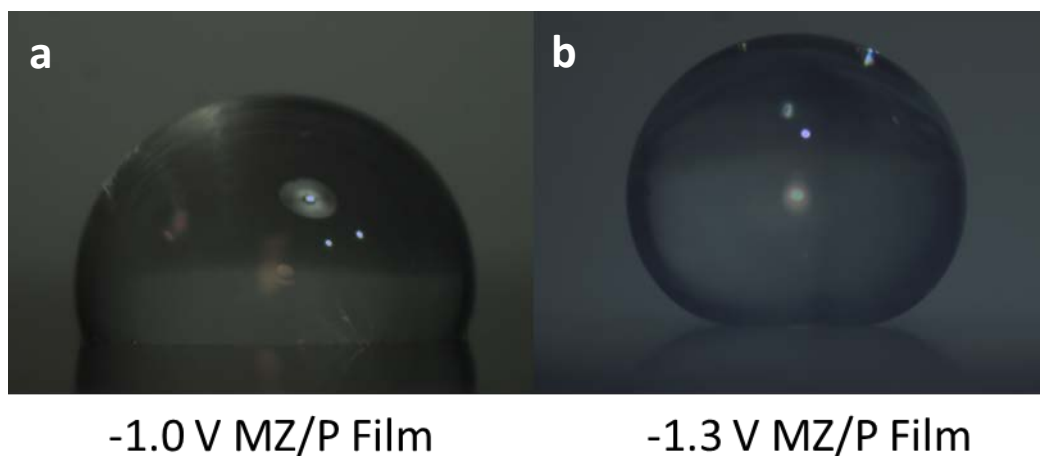


SEM images of the -1.0 V MZ film are shown in Figure 5.4a and 5.4c. The film can be characterized by a smooth homogeneous surface with spider web-like drying fractures that

have been observed in previous studies [44,45]. The surface of the film after reaction with palmitic acid is shown in Figure 5.4e. There is no visible difference in the morphology between the -1.0 V MZ and -1.0 V MZ/P films. SEM images of the -1.3 V MZ film are shown in Figure 5.4b and 5.4d. The surface is highly textured and homogeneous. There is a lot of void space between the amorphous structures that make up the textured surface. Figure 5.4f shows that the -1.3 V MZ and the -1.3 V MZ/P surfaces have the same morphology.

5.3.2. Contact Angle

Figure 5.5. Optical images of the SWCA for a) -1.0 V MZ/P and b) -1.3 V MZ/P films.



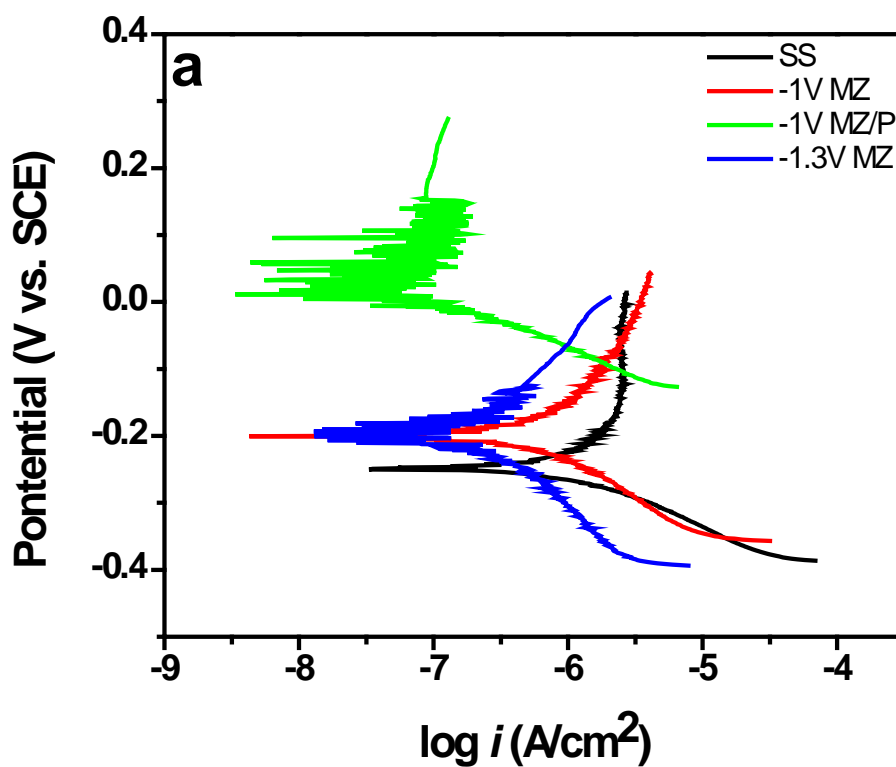
The optical SWCA images are displayed in Figure 5.5. The SWCA values in Table 5.2 support the morphology differences displayed in Figure 5.4. The -1 V MZ/P film displays a hydrophobic SWCA of 106.9° and the -1.3 V MZ/P film displays a superhydrophobic SWCA of 169.9°. The SWCA value of 169.9° is as large or greater than previous research involving SHP hydroxide or LDH films [31,32,34-36,46,47].

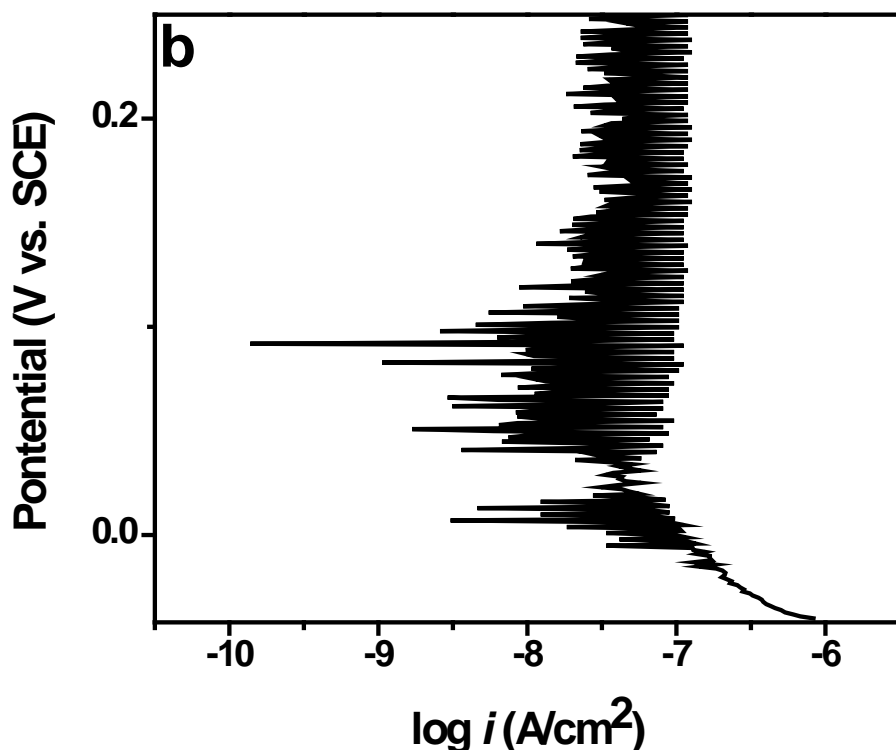
Table 5.2. SWCA of the -1.0 V MZ/P and -1.3 V MZ/P films.

	-1.0 V MZ/P	-1.3 V MZ/P
Contact Angle	$106.9 \pm 1.2^\circ$	$169.9 \pm 0.7^\circ$

5.3.3. Corrosion Resistance

Figure 5.6. a) Polarization curves of SS, -1.0 V MZ, -1.0 V MZ/P and -1.3 V MZ measured in 3.5 wt.% NaCl. b) Polarization curve of the -1.3 V MZ/P film in 3.5 wt.% NaCl.





The polarization curves of the bare SS substrate, -1 V MZ, -1.3 V MZ and -1 V MZ/P samples in 3.5 wt.% NaCl solution are shown in Figure 5.6a. The corrosion potential (E_{corr}) and the corrosion current density (i_{corr}) for each sample is listed in Table 5.3. The deposition of MZ onto SS resulted in a positive shift in the E_{corr} and a decrease in the i_{corr} . Also, a higher deposition potential of MZ caused a positive E_{corr} shift and a decrease in i_{corr} . Hydrophobization of the films also shifted the E_{corr} in a positive direction and decreased the i_{corr} . The i_{corr} decreased from 1.32×10^{-6} A to 6.78×10^{-7} A, 2.20×10^{-7} A and 5.39×10^{-8} A for the SS, -1 V MZ, -1.3 V MZ, and -1 V MZ/P films, respectively. The polarization curve of the -1.3 V MZ/P film is shown in Figure 5.6b. The extreme oscillation of the current may be due to the layer of air that forms on SHP surfaces. Although the plot is too noisy to obtain accurate E_{corr} and i_{corr} values, the plot appears to be shifted more anodic than the other samples and most of the observed current is less than 10^{-7} A indicating improved corrosion protection. These polarization measurements

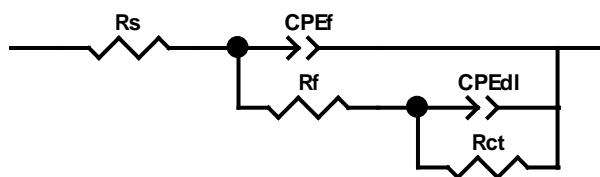
indicate that the film provides a barrier to the transport of aqueous species to the substrate so that the ability of the chloride to attack the substrate is reduced. Hydrophobization of the films improves this barrier. Some current density oscillation is observed around E_{corr} and in the anodic branch of the polarization curves which was also observed in a previous study [48]. The current density oscillation becomes greater as the observed current decreases. This may be due to the dissolution of hydroxides from the coating surface or surface anion exchange with chlorides in the solution.

Table 5.3. Corrosion potential (E_{corr}) and corrosion current density (i_{corr}) of the samples.

	E_{corr} (V vs. SCE)	i_{corr} ($\mu\text{A}\cdot\text{cm}^{-2}$)
SS	-0.254	1.32×10^{-6}
-1V MZ	-0.203	6.78×10^{-7}
-1.3V MZ	-0.186	2.20×10^{-7}
-1V MZ/P	0.046	5.39×10^{-8}

The stability of the bare SS substrate, -1 V MZ, -1.3 V MZ, -1 V MZ/P, and -1.3 V MZ/P samples in a corrosive marine environment was simulated with immersion testing in 3.5 wt.% NaCl solution. EIS data was acquired after 1 h and 192 h of immersion. The equivalent circuit used to fit the EIS spectra is shown in Figure 5.7. R_s represents the solution resistance while R_{ct} and R_f represent the charge transfer resistance and the film resistance. CPE_{dl} and CPE_f are the double layer and film capacitances. R_{ct} and CPE_{dl} represent the film/substrate interface. The electrochemical model takes into account that microstructural pinholes exist in the film which allows some of the electrolyte solution to pass through and corrosive species are able to attack the substrate [49]. R_f represents the resistance of the microstructural pinholes that provide a channel for ions.

Figure 5.7. Equivalent circuit model used to fit EIS data of bare SS substrate, MZ films, and MZ/P films.

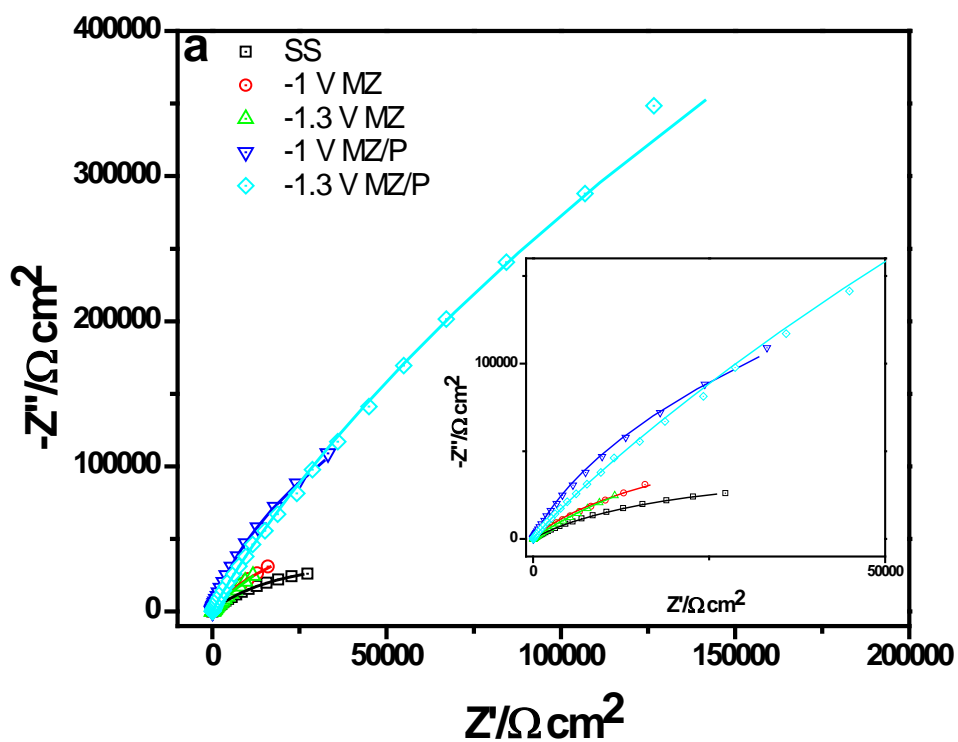


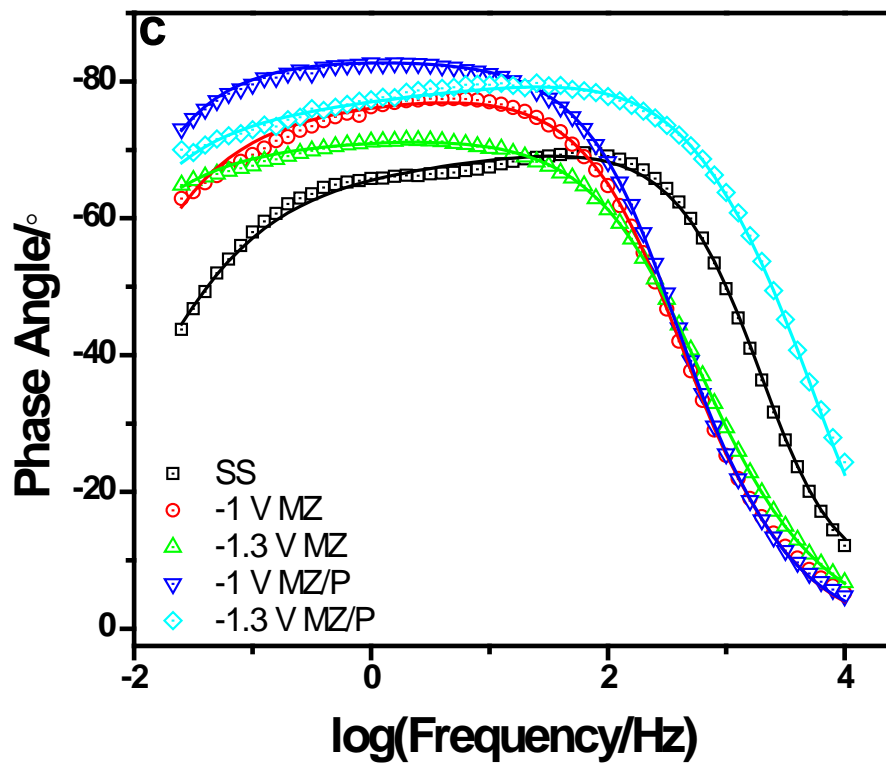
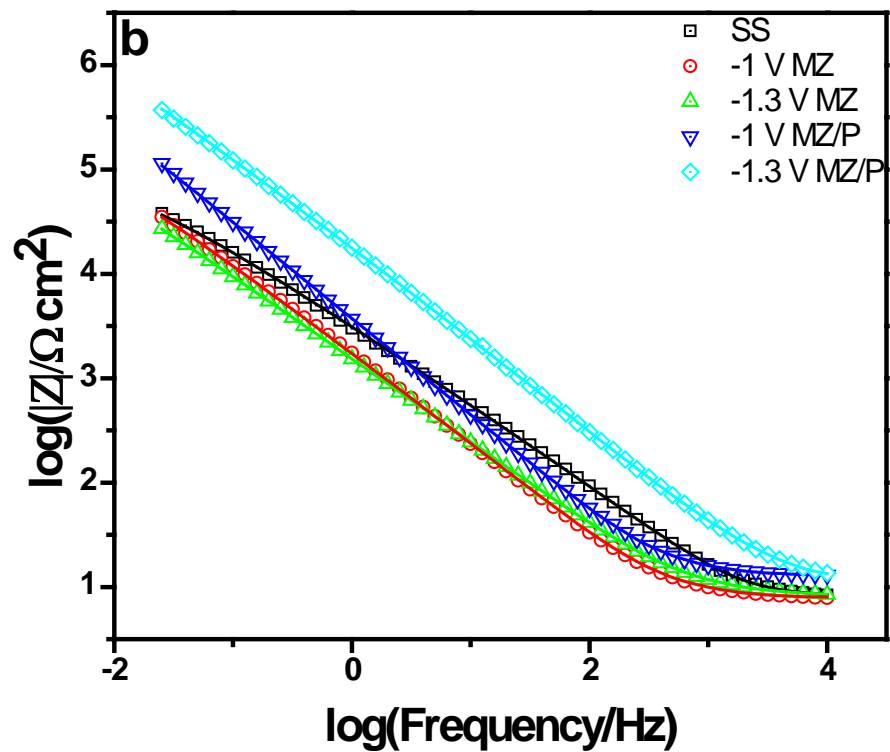
The Nyquist, Bode magnitude, and Bode phase plots of the samples immersed for 1 h in 3.5% NaCl are displayed in Figure 5.8. Partial semicircles can be observed for each sample in Figure 5.8a and the larger the semicircle the greater the corrosion resistance. According to the Nyquist plot, -1.3 V MZ/P film shows the greatest corrosion resistance followed by -1 V MZ/P. The -1 V and -1.3 V MZ films seem to have similar resistances while SS has the lowest. The Bode magnitude plot is shown in Figure 5.8b and all samples display a similar behavior. A higher Z modulus at lower frequencies indicates better corrosion resistance of the metal substrate. Again the -1.3 V MZ/P film displays the greatest corrosion resistance followed by -1 V MZ/P. The SS substrate has a higher Z modulus than both -1.3 V and -1 V MZ films. The Bode phase angle plot is shown in Figure 5.8c and all samples show similar behavior. The phase angle reaches a plateau around 10^2 Hz and it doesn't decrease until 10^{-1} Hz. The phase angles of the SS and -1.3 V MZ/P film plateau at slightly higher frequency than the other samples.

The calculated parameters for the equivalent circuit model in Table 5.4 support most of the behavior observed in the Nyquist and Bode plots. The -1.3 V MZ/P film has the greatest R_{ct} of $3.14 \times 10^6 \Omega \text{ cm}^2$ and the -1 V MZ/P film has the next highest at $5.97 \times 10^5 \Omega \text{ cm}^2$. The R_{ct} of -1.3 V MZ, -1 V MZ, and SS were 2.60×10^5 , 1.50×10^5 , and $9.20 \times 10^5 \Omega \text{ cm}^2$ respectively. The

layer of air on top of the film generated by SHP surface of the -1.3 V MZ/P film is responsible for its high R_{ct} . Because the water repellency of the -1 V MZ/P film is less, it had a lower R_{ct} .

Figure 5.8. a) Nyquist plot, b) Bode plot of $\log|Z|$ vs. $\log(\text{frequency})$, and c) Bode plot of phase angle vs. $\log(\text{frequency})$ of samples at 1 h immersion in 3.5% NaCl. The straight lines represent the simulated curves from ZView.



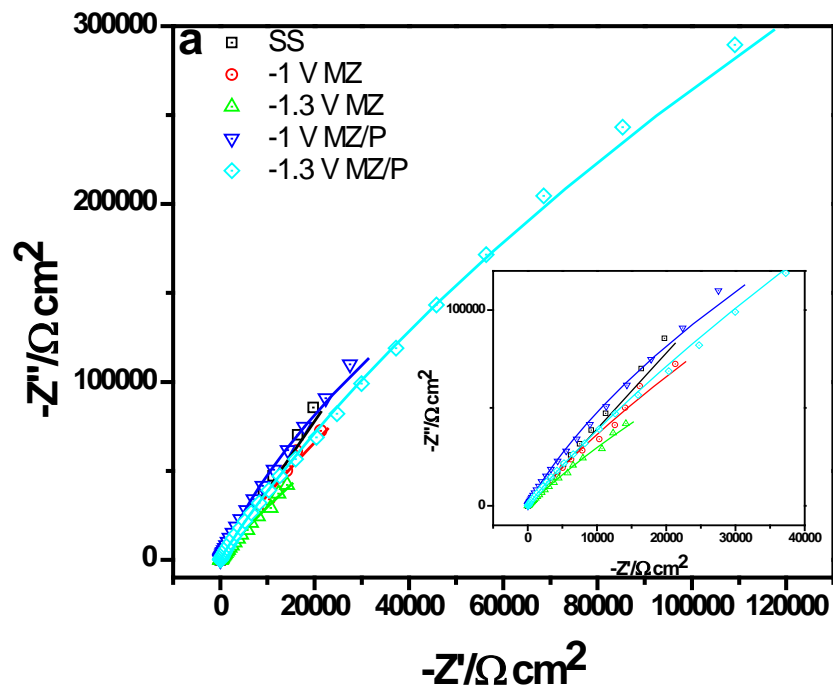


The Nyquist plot in Figure 5.9a indicates that all of the samples have similar looking spectra after 192 h immersion. After 192 h, the -1.3 V MZ/P, -1 V MZ/P, and the SS samples show the highest resistance. It is difficult to estimate resistance from these samples because they are grouped close together and their semicircles are incomplete. The -1.3 V MZ film seems to have the lowest resistance and the -1 V MZ film has a slightly higher resistance. The Bode magnitude plot in Figure 5.9b shows that the -1.3 V MZ/P film has the greatest Z modulus at lower frequencies followed by -1 V MZ/P, SS, -1 V MZ, and then -1.3 V MZ. The Bode phase angle plot in Figure 5.9c is similar to the plot observed at 1 h immersion. The phase angles reach a plateau between 10^1 - 10^2 Hz and then slightly decrease at lower frequencies (10^{-1} Hz). The -1.3 V MZ/P phase angle reaches its maximum at a higher frequency than the others and the -1.0 V MZ/P phase angle reaches its maximum at a lower frequency than the others.

The circuit element values from Table 5.4 indicate that the corrosion resistance of almost all the samples increased after 192 h immersion in 3.5% NaCl. Only the R_{ct} of the -1.3 V MZ/P film decreased after 192 h to $2.81 \times 10^6 \Omega \text{ cm}^2$. The monolayer of palmitic acid on the surface of the -1.3 V MZ/P film may have been damaged by the chloride environment resulting in the loss of the protective air pocket and a lower R_{ct} . Even with its decreased R_{ct} the -1.3 V MZ/P has the highest resistance of the coated substrates. The -1 V MZ/P film had a R_{ct} of $1.19 \times 10^6 \Omega \text{ cm}^2$ which is twice as large as its 1 h value. Surprisingly, the -1 V MZ film had a slightly higher R_{ct} of $1.52 \times 10^6 \Omega \text{ cm}^2$. The R_{ct} value of the -1.3 V MZ film is $8.12 \times 10^5 \Omega \text{ cm}^2$. The -1 V MZ has a higher R_{ct} than the -1.3 V MZ because the high deposition potential may have produced gas bubbles leading to increased defects in the coating. The bare SS sample showed

an increase in R_{ct} to $2.24 \times 10^7 \Omega \text{ cm}^2$ probably due to the passivating oxide layer that formed during the immersion period.

Figure 5.9. a) Nyquist plot, b) Bode plot of $\log|Z|$ vs. $\log(\text{frequency})$, and c) Bode plot of phase angle vs. $\log(\text{frequency})$ of samples at 192 h immersion in 3.5% NaCl. The straight lines represent the simulated curves from ZView.



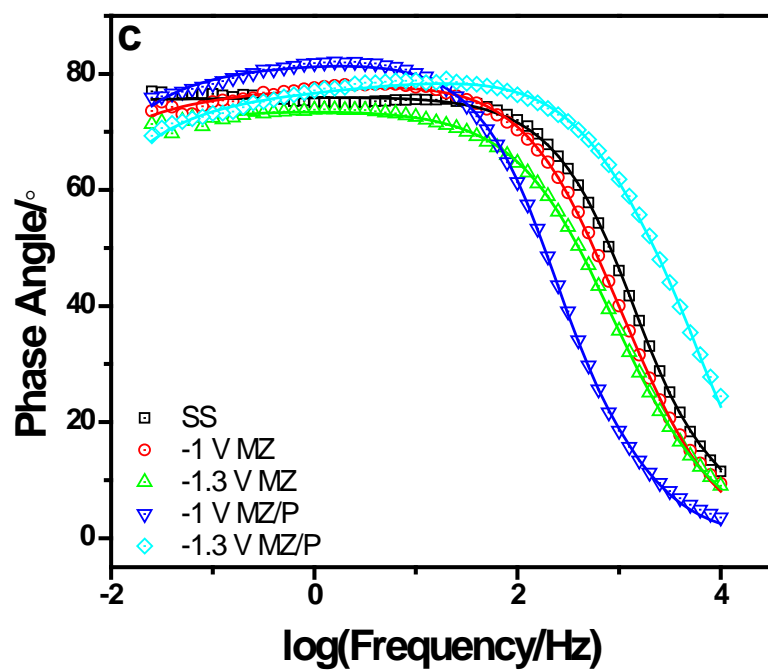
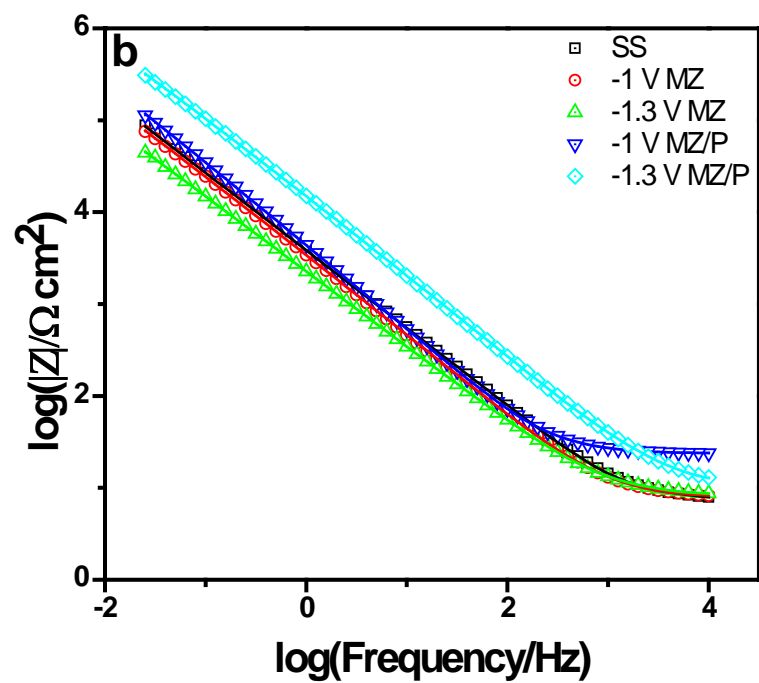
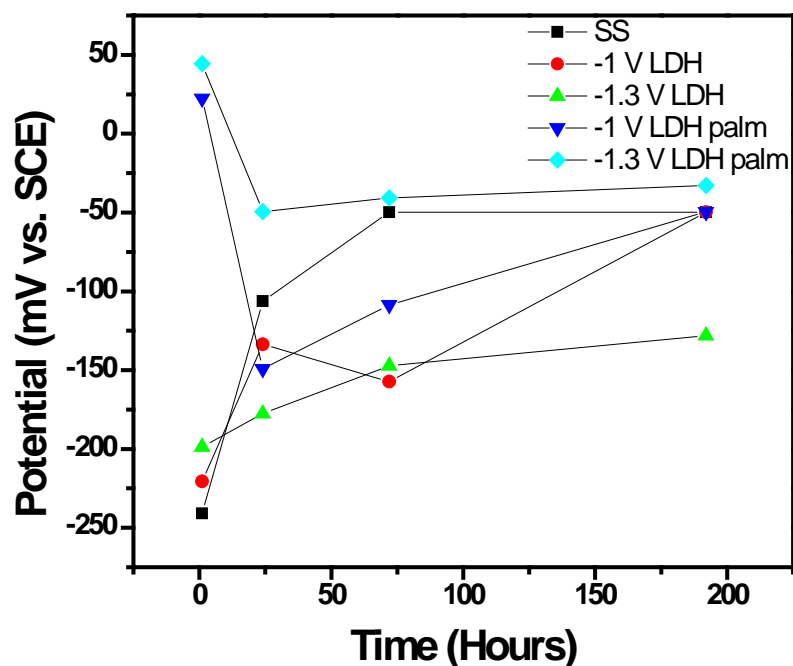


Table 5.4. Fitting parameters of impedance spectra after 1 h and 192 h immersion in 3.5% NaCl calculated using ZView.

	SS		-1 V MZ		-1 V MZ/P		-1.3 V MZ		-1.3 V MZ/P	
	1 h	192 h	1 h	192 h	1 h	192 h	1 h	192 h	1 h	192 h
$R_{sol}/\Omega \text{ cm}^2$	6.61	7.21	7.96	8.05	8.17	8.16	12.89	23.96	11.97	11.22
CPE_f	7.64 E -5	5.28 E -5	2.82 E -5	2.28 E -5	3.66 E -5	1.51 E -5	6.54 E -5	6.83 E -5	2.67 E -6	3.42 E -6
CPE_f-n	0.72	0.83	1.00	0.95	0.93	1.00	0.86	0.84	1.00	0.99
$R_f/\Omega \text{ cm}^2$	4.21	15.52	7.93	20.20	34.97	26.68	8.71	26.12	43.10	41.62
CPE_{dl}	5.64 E -6	2.38 E -6	9.51 E -5	3.86 E -5	1.22 E -5	2.87 E -5	8.76 E -5	2.98 E -5	9.33 E -6	1.08 E -5
CPE_{dl-n}	1.00	1.00	0.79	0.79	0.91	0.85	0.73	0.80	0.80	0.80
$R_{ct}/\Omega \text{ cm}^2$	9.20 E 4	2.24 E 7	1.50 E 5	1.52 E 6	5.97 E 5	1.19 E 6	2.60 E 5	8.12 E 5	3.14 E 6	2.81 E 6

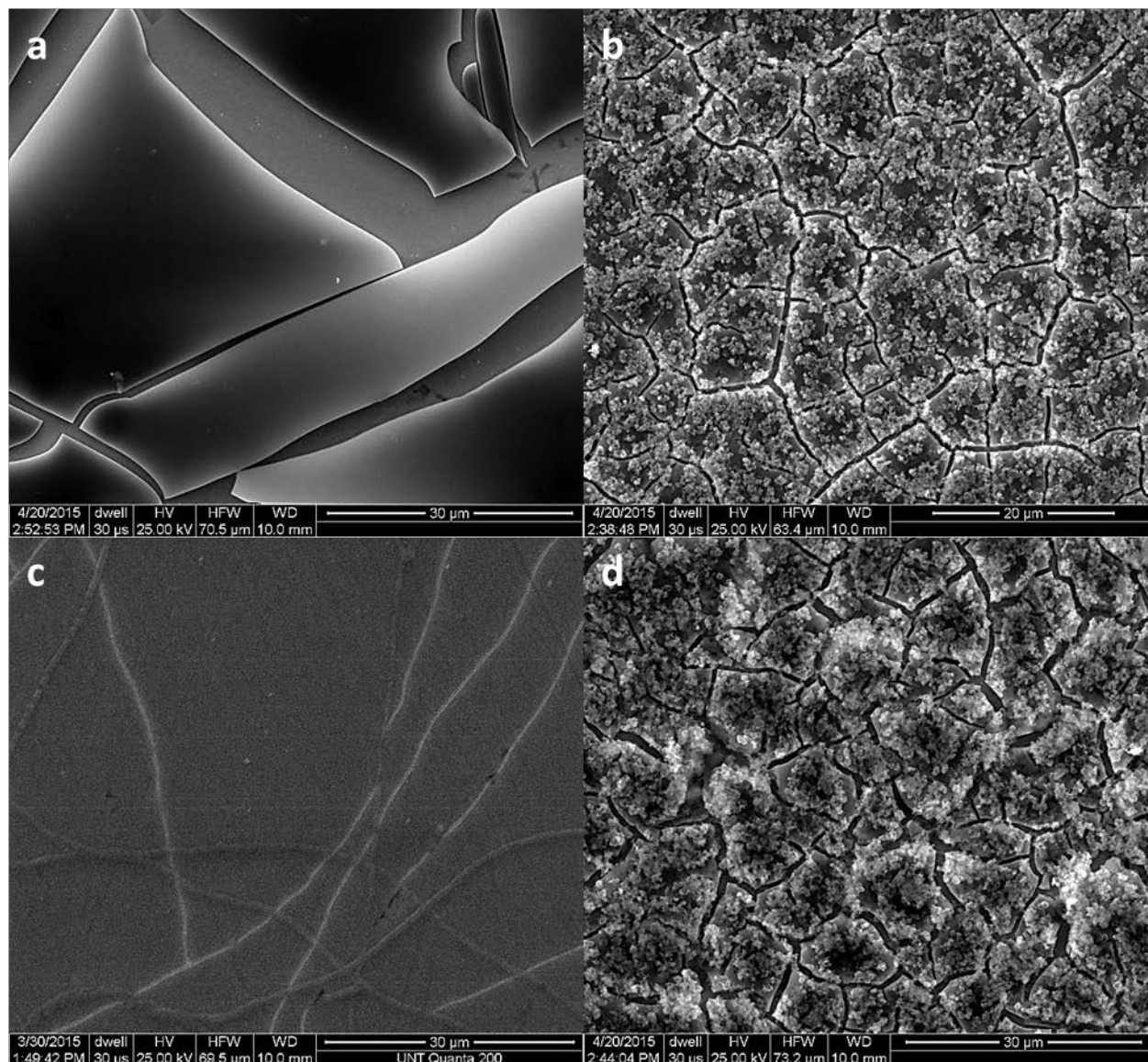
The open circuit potential value of each sample was monitored during the immersion period of 192 h and is displayed in Figure 5.10. The -1.3 V MZ/P and -1.0 V MZ/P films initially (after 1 h) had the most positive OCPs of 44 and 22 mV respectively. The initial OCPs of the SS, -1 V MZ, and -1.3 V MZ films were -241, -221, and -199 mV respectively. The OCPs of the -1.3 V MZ/P and -1.0 V MZ/P films shifted cathodically and the SS, -1 V MZ, and -1.3 V MZ films shifted anodically. At the end of the 192 h immersion period, the SS, -1 V MZ, and -1 V MZ/P films all had an OCP of -50 mV. These similar OCPs could be the result of the samples degrading similarly or producing similar corrosion products. The -1.3 V MZ film ended at an OCP of -128 mV while the -1.3 V MZ/P film had a final OCP of -33 mV. The more anodic final OCP of the -1.3 V MZ/P film may be the result of the damaged palmitic acid monolayer still repulsing water molecules.

Figure 5.10. OCP monitoring in 3.5% NaCl.



SEM images were taken of each coated sample after immersion for 192 h. In Figure 5.11a it seems that the -1 V MZ film has fractured revealing the SS substrate below. This film was not able to withstand the corrosive chloride electrolyte. Figure 5.11b shows the -1.3 V MZ film after immersion. The surface appears slightly fractured, but the underlying SS substrate is not observed. The SEM image of the immersed -1 V MZ/P sample is shown in Figure 5.11c. The sample appears to be unaffected by the corrosive electrolyte. The SEM image of the -1.3 V MZ/P film is displayed in Figure 5.11d. It looks very similar to the -1.3 V MZ film with a slightly fractured appearance. This damage suggests the possible dissolution of the palmitic acid monolayer allowing the corrosive electrolyte to attack the surface.

Figure 5.11. SEM images of a) -1 V MZ, b) -1.3 V MZ, c) -1 V MZ/P, and d) -1.3 V MZ/P films after 192 h immersion in 3.5% NaCl.



5.4. Chapter Conclusions

Hydrophobic and SHP MZ/P films on SS 430 substrates were prepared by electrodeposition and immersion reaction in a palmitic acid/ethanol solution. All synthesis conditions were the same between the hydrophobic and SHP films except the film deposition

potential. A higher (-1.3 V vs. -1.0 V) deposition potential resulted in higher surface roughness and therefore a SHP surface. XRD showed that the films deposited at different potentials had a similar structure. FTIR showed that bonds were formed between the palmitic acid and the film creating a low-surface-energy monolayer on top of the film. Potentiodynamic polarization and EIS in 3.5% NaCl revealed that the -1.3 V MZ/P film showed the better initial corrosion resistance than the -1 V MZ/P film. After a 192 h immersion period, the -1.3 V MZ/P film displayed a slightly decreased yet still higher corrosion resistance than the -1.0 V MZ/P film.

5.5. References

- [1] Corrosion Cost and Preventive Strategies In the United States. McLean, Va. (6300 Georgetown Pike, McLean 22101-2296): U.S. Dept. of Transportation, Federal Highway Administration, Research Development and Technology, Turner-Fairbank Highway Research Center, 2002.
- [2] N. R. Baddoo, *J. of Constructional Steel Res.*, 2008, 64, 1199-1206.
- [3] A. Latifi, M. Imani, M. T. Khorasani, M. D. Joupari, *Surf. Coatings Technol.* 2013, 221, 1-12.
- [4] T. J. Mesquita, E. Chauveau, M. Mantel, N. Bouvier, D. Koschel, *Corros. Sci.*, 2014, 81, 152-161.
- [5] G. Herting, I. O. Wallinder, C. Leygraf, *J. of Food Engineer.*, 2008, 87, 291-300.
- [6] C. Bitondo, A. Bossio, T. Monetta, M Curioni, F. Bellucci, *Corros. Sci.*, 2014, 87, 6-10.
- [7] T. K. Ha, H. T. Jeong, H. J. Sung, *J. Mater. Processing Technol.*, 2008, 187-188, 555-558.
- [8] M. A. Akl, M. A. Ahmed, A. Ramadan, *J. of Pharmaceutical and Biomedical Analy.*, 2011, 55, 247-252.

- [9] Q. Hu, G. Zhang, Y. Qiu, X. Guo, *Corros. Sci.*, 2011, 53, 4065–4072.
- [10] Y. Yin, L. Niu, M. Lua, W. Guo, S. Chen, *Appl. Surf. Sci.*, 2009, 255, 9193–9199.
- [11] A.-M. Lazar, W. P. Yespica, S. Marcelin, N. Pébère, D. Samélor, C. Tendero, C. Vahlas, *Corros. Sci.*, 2014, 81, 125-131.
- [12] M. B. González, S. B. Saidman, *Prog. in Org. Coat.*, 2015, 78, 21-27.
- [13] T. Stimpfling, F. Leroux, H. Hintze-Bruening, *Colloids and Surf. A: Physicochemical and Engineer. Asp.*, 2014, 458, 147-154.
- [14] M.L. Zheludkevich, S.K. Poznyak, L.M. Rodrigues, D. Raps, T. Hack, L.F. Dick, T. Nunes, M.G.S. Ferreira, *Corros. Sci.*, 2010, 52, 602–611.
- [15] J. Tedim, M.L. Zheludkevich, A.C. Bastos, A.N. Salak, A.D. Lisenkov, M.G.S. Ferreira, *Electrochimica Acta.*, 2014, 117, 164-171.
- [16] X. Guo, F. Zhang, D. G. Evans, X. Duan, *Chem. Comm.*, 2010, 46, 5197-5210.
- [17] J. Tedim, A. Kuznetsova, A.N. Salak, F. Montemor, D. Snihirova, M. Pilz, M.L. Zheludkevich, M.G.S. Ferreira, *Corros. Sci.*, 2012, 55, 1–4.
- [18] T. Yan, S. Xu, Q. Peng, L. Zhao, X. Zhao, X. Lei, F. Zhang, *J. Electrochem. Soc.*, 2013, 160, C480-C486.
- [19] G. Villemure, A. J. Bard. *J. Electroanal. Chem.*, 1990, 282, 107-121.
- [20] J. Syu, J. Uan, M. Lin, Z. Lin, *Corros. Sci.*, 2013, 68, 238–248.
- [21] J. Wang, D. Li, Q. Liu, X. Yin, Y. Zhang, X. Jing, M. Zhang, *Electrochim. Acta*, 2010, 55, 6897-6906.
- [22] T. Liu, S. Chen, S. Cheng, J. Tian, X. Chang, Y. Yin, *Electrochim. Acta*, 2007, 52, 8003-8007.
- [23] L. Li, V. Breedveld, D. W. Hess, *Appl. Mater. Interfaces*, 2012, 4, 4549-4556.

- [24] L. J. Chen, M. Chen, H. D. Zhou, J. M. Chen, *Appl. Surf. Sci.*, 2008, 255, 3459-3462.
- [25] Q. Huang, Y. Yang, R. Hu, C. Lin, L. Sun, E. A. Vogler, *Colloids Surf., B.*, 2015, 125, 134-141.
- [26] C. Lee, A. Kim, J. Kim, *Surf. Coat. Technol.*, 2015, 264, 127-131.
- [27] B. Wu, M. Zhou, J. Li, X. Ye, G. Li, L. Cai, *Appl. Surf. Sci.*, 2009, 256, 61-66.
- [28] H. Yang, P. Pi, Z. Cai, X. Wen, X. Wang, J. Cheng, Z. Yang, *Appl. Surf. Sci.*, 2010, 256, 4095-4102.
- [29] M. A. Frank, A. R. Boccaccini, S. Virtanen, *Appl. Surf. Sci.*, 2014, 311, 753-757.
- [30] A.B.D. Cassie, S. Baxter, *Trans. Faraday Soc.*, 1944, 40, 546.
- [31] F. Zhang, L. Zhao, H. Chen, S. Xu, D. G. Evans, X. Duan, *Angew. Chem. Int. Ed.*, 2008, 47, 2466–2469.
- [32] X. Lei, L. Wang, X. Zhao, Z. Chang, M. Jiang, D. Yan, X. Sun, *Industrial & Engineering Chem. Res.*, 2013, 52, 17934–17940.
- [33] X.X. Guo, S.L. Xu, L.L. Zhao, W. Lu, F.Z. Zhang, D.G. Evans, X. Duan, *Langmuir*, 2009, 25, 9894–9897.
- [34] M. Zhou, X. Pang, L. Wei, K. Gao, *Appl. Surf. Sci.*, 2015, 337, 172–177.
- [35] Y. Li, S. Li, Y. Zhang, M. Yu, J. Liu, *Mater. Lett.*, 2015, 142, 137–140.
- [36] Y. Wang, D. Zhang, Z. Lu, *Colloids and Surfaces A: Physicochem. Eng. Aspects*, 2015, 474, 44–51.
- [37] M.S. Yarger, E.M.P. Steinmiller, K.S. Choi, *Inorg. Chem.*, 2008, 47, 5859–5865.
- [38] F. Wu, J. Liang, Z. Peng, B. Liu, *Appl. Surf. Sci.*, 2014, 313, 834–840.

- [39] A. de Roy, C. Forano, J.P. Besse, Layered double hydroxides: synthesis and post-synthesis modification, in: V. Rives (Ed.), *Layered Double Hydroxides: Present and Future*, Nova Science Publishers, Inc., New York, 2001, pp. 1-39.
- [40] J. T. Klopprogge, R. L. Frost, L. Hickey, *J. Raman Spectr.*, 2004, 35, 967–974.
- [41] Y. Lin, J. Wang, D. G. Evans, D. Li, *J. Phys. Chem. Solid.*, 2006, 67, 998-1001.
- [42]] M. Ruan, W. Li, B. Wang, Q. Luo, F. Ma, Z. Yu, *Appl. Surf. Sci.*, 2012, 258, 7031– 7035.
- [43] G. Hu, N. Wang, D. O'Hare, J. Davis, *J. Mater. Chem.*, 2007, 17, 2257-2266.
- [44] J. Chen, Y. Song, D. Shan, E. Han, *Corros. Sci.*, 2012, 65, 268–277.
- [45] J. Chen, Y. Song, D. Shan, E. Han, *Corros. Sci.*, 2012, 63, 148-158.
- [46] D.La, T. A. Nguyen, S. Lee, J. W. Kim, Y. S. Kim, *Appl. Surf. Sci.*, 2011, 257, 5705–5710.
- [47] R.V. Lakshmi, B. J. Basu, *J. Colloid Interface Sci*, 2009, 339, 454–460.
- [48] T. Ishizaki, S. Chiba, K. Watanabe, H. Suzuki, *J. of Mater. Chem. A.*, 2013, 1, 8968-8977.
- [49] D. Yu, J. Tian, J. Dai, X. Wang, *Electrochim. Acta*, 2013, 97, 409-419.

CHAPTER 6

CONCLUSIONS AND SUGGESTIONS FOR FUTURE WORK

6.1. Summary of Dissertation Research

In the first project, a stable sensor for the determination of gallic acid (GA) and caffeic acid (CA) was fabricated by electrodeposition of Zn-Al-NO₃ layered double hydroxide film on a glassy carbon electrode (LDHf/GCE). The differential pulse voltammetry response of the LDHf/GCE to GA has a linear concentration range from 4 mM to 600 mM with a correlation coefficient of 0.9985 and the calculated detection limit of 1.6 mM at a signal-to-noise ratio of 3. The differential pulse voltammetry response of the LDHf/GCE to CA has a linear concentration range from 7 mM to 180 mM with a correlation coefficient of 0.9969 and the calculated detection limit of 2.6 mM at a signal-to-noise ratio of 3. The constructed sensor was applied to the determination of GA in commercial green tea samples. While the sensor could determine the phenolic content of the tea, the sensor was not selective enough to differentiate between GA and other similar phenolic compounds.

Modified zaccagnaite (Zn-Al-NO₃) films were synthesized on stainless steel substrates by multilayer electrochemical deposition in aqueous solutions. Structural characterization indicated a pure layered double hydroxide phase; however, elemental analysis revealed that the surface of the films contained Zn:Al ratios outside the reliable ranges of layered double hydroxides. The films are labeled modified zaccagnaite because of the irregular metal content and the substitution of nitrate for carbonate. The corrosion resistance of the film was determined with polarization measurements in 3.5 wt.% NaCl. The corrosion current was reduced by 92% and open circuit potential was shifted 126 mV more positive. The films

maintained their corrosion resistance after immersion of the films in 3.5 wt.% NaCl for 168 h. This corrosion protection is a result of the multilayer deposition method. Each successive layer fills in the voids and defects in the previous layer.

Superhydrophobic surfaces on stainless steel substrates were prepared by the electrodeposition of a modified zaccagnaite film followed by a hydrophobization reaction with palmitic acid. The effects of modified zaccagnaite electrodeposition potential, electrodeposition time, palmitic acid concentration, hydrophobization reaction time, and hydrophobization reaction temperature were systematically investigated. Contact angle measurements were performed to evaluate the wettability of the films. Optimization of film synthesis resulted in a surface with a static water contact angle of 169.9°.

Superhydrophobic and hydrophobic surfaces on stainless steel substrates were prepared by the electrodeposition of a modified zaccagnaite film followed by a hydrophobization reaction with palmitic acid. The superhydrophobic surface (169.9°) was produced with the optimized parameters determined in previous work. The hydrophobic surface (106.9°) was synthesized utilizing the same parameters except for a different electrodeposition potential. The corrosion properties of both films were investigated with potentiodynamic polarization. The stability of the films was investigated with electrochemical impedance spectroscopy during before and after a 192 h immersion period in 3.5 wt.% NaCl. Both films provide superior initial corrosion resistance when compared to the bare SS substrate and maintained this protection after the 192 h immersion period. The corrosion resistance of the superhydrophobic film decreased slightly during the immersion period. This suggests that the palmitic acid monolayer is not stable for long durations in saltwater.

6.2. Suggestions for Future Work

The sensor research could be continued by examining the surface morphology with a confocal microscope. The film was observed by SEM, but the conditions of the SEM analysis (high vacuum and electron beam) may have damaged the film. Observing with a confocal microscope will also allow the film to be observed in a hydrated state which is more similar to its actual state when it is used for sensing in aqueous solutions. The effective electrode area should also be calculated for both the bare and modified electrode. The area can be determined by performing cyclic voltammetry with a well-known redox probe such as potassium ferricyanide at various scan rates in conjunction with the Randles-Sevcik equation. The effective area can be calculated as long as the scan rate, diffusion coefficient of the redox probe, bulk concentration of the redox probe, and the number of electrons transferred are known. Changing the metal constituents of the LDH film in order to transform it to a conductive material. The Zn cation could be replaced with transitional metals such as Ni or Fe. Increasing the conductivity of the film should improve the sensitivity and possibly make it able to differentiate between similar structured analytes. Another direction would be to combine the LDH in film or nanosheet form with graphene or carbon nanotubes. This combination may produce a sensor with good selectivity, high sensitivity, and other unforeseen benefits. The co-deposition of LDH with a polymer could also be explored to minimize defects due to drying of the film.

Further research can be performed on the multilayer modified zaccagnaites films from the second chapter. Thermal techniques could be performed to characterize the film. Thermal gravimetric analysis could be done to determine the water and anion content. The corrosion

resistance could be studied further by performing electrochemical impedance spectroscopy. Other corrosion analysis techniques that could be performed are the humidity cabinet test and the salt spray test. Also, the corrosion of the film could be studied in simulated seawater which contains a more complete salt content than the 3.5 wt.% NaCl solution. The films could be tested in other corrosive environments besides the sea such as atmospheric, rainwater, microbial, and desert conditions. The corrosion products of the film could be explored with Raman and X-ray photoelectron spectroscopy. Wear, hardness, and adhesion tests could be performed to assess the mechanical strength of the film. The self-healing properties of the film could be tested by making an incision through the film all the way to the substrate. Then the film would be inserted into the corrosive medium and corrosion resistance techniques could be used to see if the corrosion protection increases or decreases during immersion. The investigation of composite coatings containing exfoliated LDH nanosheets and metal alloys could yield improved mechanical and corrosion resistant properties.

The superhydrophobic films from the third and fourth chapters could be characterized further. Atomic force microscopy could be used to investigate the morphology and surface roughness in more detail and resolution than stylus profilometry. The stability of the static water contact angle could be measured over extended amounts of time in atmosphere and different aqueous environments. Contact angle hysteresis and sliding angle could be measured to investigate the adhesion of water on the surface of the film. Mechanical tests such as hardness, abrasion, and adhesion tests could be performed. Corrosion testing of the films could be performed in a variety of corrosive environments. The low surface energy modifier could be changed to trans unsaturated fatty acid in order to obtain a cross linked hydrophobic

monolayer. Crosslinking would provide greater resistance to the dissociation of the fatty acid and because the fatty acid is in the trans configuration the molecules can be tightly packed resulting in better surface coverage.

Layered double hydroxides and their derivatives are an exciting area of research. They have a very unique layered charge structure that lends them to many potential applications. They are found in nature and can replace current materials that are harmful to the environment. These materials are easy to synthesize and most methods do not create much waste. The constituents and properties of the films can be easily changed and modified. These benefits ensure that layered double hydroxides will continue to be explored in the future.